Light fields in complex media: Mesoscopic scattering meets wave control

Stefan Rotter[*]

Institute for Theoretical Physics, Vienna University of Technology (TU Wien), Wiedner Hauptstraße 8–10/136, 1040 Vienna, Austria, EU

Sylvain Gigan[†]

Laboratoire Kastler Brossel, UMR8552 Université Pierre et Marie Curie, Ecole Normale Supérieure, Collège de France, CNRS, 24 rue Lhomond, 75005 Paris, France, EU

(published 2 March 2017)

The newly emerging field of wave front shaping in complex media has recently seen enormous progress. The driving force behind these advances has been the experimental accessibility of the information stored in the scattering matrix of a disordered medium, which can nowadays routinely be exploited to focus light as well as to image or to transmit information even across highly turbid scattering samples. An overview of these new techniques, their experimental implementations, and the underlying theoretical concepts following from mesoscopic scattering theory is provided. In particular, the intimate connections between quantum transport phenomena and the scattering of light fields in disordered media, which can both be described by the same theoretical concepts, are highlighted. Particular emphasis is put on how these topics relate to application-oriented research fields such as optical imaging, sensing, and communication.

DOI: 10.1103/RevModPhys.89.015005

CONTENTS

[*]stefan.rotter@tuwien.ac.at
[†]sylvain.gigan@lkb.ens.fr

I. INTRODUCTION

Recent years have witnessed enormous conceptual and experimental progress in the ability to manipulate light fields both spatially and temporally. On the experimental side these advances have largely been enabled by the availability of highly tunable digital arrays, also known as spatial light modulators (Savage, 2009), which are meanwhile being used to create arbitrarily complex light fields. In this sense the current state of the art in the field of optical wave front shaping is reminiscent of the situation in related areas such as acoustics and seismology, which were similarly promoted by antenna or transducer arrays that can retrieve information from a complex environment. The availability of such versatile tools now also in optics opens up the way to address a topic where conventional optical techniques are hard to apply, like the control of light propagation in turbid media such as in amorphous or disordered materials, biological tissues, complex photonic structures, plasmonic systems, multimode fibers, etc. Starting points for these activities were a number of proof-of-principle experiments that recently demonstrated that a disordered material can be used to focus light (Vellekoop and Mosk, 2007; van Putten *et al.*, 2011) and that its transmission matrix can be measured in detail (S. M. Popoff *et al.*, 2010; Popoff, Aubry *et al.*, 2011) to reconstruct the transmission of images across highly scattering samples (S. Popoff *et al.*, 2010). Beyond spatial control, explicitly time-dependent measurements were able to show that a wave scattered in a disorder region can not only be focused in space but also in time (Aulbach *et al.*, 2011; Katz *et al.*, 2011; McCabe *et al.*, 2011; Mounaix *et al.*, 2016). Following the pioneering concepts introduced by Freund (1990a), further work successfully demonstrated that the information stored in the scattering matrix of a disordered system can be used for turning a disordered sample into a perfect mirror (Katz, Small, and Silberberg, 2012) or into a high resolution spectral filter or spectrometer (Small *et al.*, 2012; Redding *et al.*, 2013). This insight can be expected to have impact on a very broad range of fields such as biology and medicine (Cox, 2012), where imaging through disorder is a major challenge; nanophotonics (Kawata, Ohtsu, and Irie, 2002), where the challenge is to address and control quantum systems in a disordered environment (Sapienza *et al.*, 2011); quantum information (Ott, Mortensen, and Lodahl, 2010; Defienne *et al.*, 2016; Wolterink *et al.*, 2016), where entangled states could be guided and transformed, as well as communication technology (Tse and Viswanath, 2005), where the principal goal is to secure that information sent through a complex environment ends up at a desired receiver.

A sound theoretical basis required to describe these phenomena is given in terms of scattering theory. In the specific context of disorder scattering it is mostly the work in mesoscopic physics (Sebbah, 2001; Imry, 2002; Stöckmann, 2006; Akkermans and Montambaux, 2007), quantum transport (Datta, 1997; Ferry and Goodnick, 1997; Mello and Kumar, 2004), and random matrix theory (Beenakker, 1997; Alhassid, 2000; Mitchell, Richter, and Weidenmüller, 2010) that has been the principal driving force behind theoretical progress. This is because electron scattering through disordered or chaotic systems has been and continues to be one of the paradigms in the mesoscopic physics community. In spite of the progress made, many of the results obtained for the situation on the mesoscopic scale do, however, remain unknown to the newly emerging scientific communities working on wave front shaping in complex media. The reason why many insights penetrated only weakly outside the community of mesoscopic physics is probably due to the vastness of the field, which makes it difficult to overlook, and due to a specific scientific jargon which scientists working outside this community are typically not familiar with.

The intended goal of our review article is to bridge this knowledge gap. Our strategy is to demonstrate how theoretical insight from mesoscopic scattering theory has direct relevance for the recent wave control experiments and vice versa. We start in Sec. II with a brief review of mesoscopic transport theory in which basic concepts like the scattering matrix and its statistical properties following from random matrix theory or related approaches are introduced. We discuss here the concept of transmission eigenchannels as well as their connection to electronic shot noise, which provides indirect access to the distribution of transmission eigenvalues in measurements of electronic current. Particular emphasis is put on the concept of time delay in scattering and its relation to the density of states as well as to coherent wave absorption and to the quantum-to-classical crossover. With such a solid theoretical basis being established, we move on in Sec. III to review a number of mesoscopic transport effects that have meanwhile been observed in optical experiments without the help of any wave front shaping tools. As shown, quite a number of theoretical concepts first studied in a mesoscopic context could be successfully transferred and, indeed, observed with light fields in complex media. Examples highlighted here are those related to the quantization of the conductance and its universal fluctuations, weak localization, the memory effect etc. While these observations are very encouraging for the applicability of the theoretical tools introduced in Sec. II, much more can be done in these experiments with the tools of wave front shaping. These tools are reviewed in Sec. IV and we discuss how they can be used for measuring and modulating the light transmitted through the paradigmatic case of a thin disordered slab. Such an "opaque lens" can be used for focusing, imaging, and for controlling the polarization and the temporal shape of the transmitted light. In Sec. V we review how the predictions from mesoscopic transport theory can be fully brought to bear using the wave front shaping tools introduced earlier. First, we focus on effects that were already realized in corresponding experiments such as those related to open and closed transmission channels, the memory effect, etc. In the next step we provide a collection of many interesting predictions that still await an implementation in the laboratory. This outlook also serves the purpose of indicating future directions of research and demonstrating how much "uncharted territory" is yet to be developed in this increasingly active field of research. Our review is completed with a summary in Sec. VI.

We intentionally restricted the scope of this review to the interface between mesoscopic scattering theory and the recent advances in wave front shaping. With this focus we hope to provide some added value to both of the corresponding

communities that we are trying to better connect with our article. At this point we emphasize that excellent reviews and books are already available for each of these two separate fields: Regarding mesoscopic scattering, interested readers may find a wealth of information on specific topics such as the random matrix theory (RMT) (Beenakker, 1997; Guhr, Müller-Groeling, and Weidenmüller, 1998; Akemann, Baik, and Francesco, 2011), or the maximum entropy approach (Mello and Kumar, 2004), as well as the many interesting connections between electronic transport and light scattering (Lagendijk and van Tiggelen, 1996; Dragoman and Dragoman, 2004; Akkermans and Montambaux, 2007). Also for wave front shaping the first short reviews have recently become available (Mosk *et al.*, 2012; Shi, Davy, and Genack, 2015; Vellekoop, 2015; Vos, Lagendijk, and Mosk, 2015). The niche we intend to fill with this contribution is to highlight the underappreciated connection between the two topical areas and its potential for future research.

II. SCATTERING THEORY FOR COMPLEX MEDIA

The scattering of waves through disordered or otherwise complex media is a problem that can be approached from many different angles. In particular, a whole hierarchy of different methods have been developed that provide insight into different levels of accuracy, typically anticorrelated with the complexity of a specific method. For the purpose of this review, we are mostly interested in those approaches, which retain the wave nature of the scattering process, such as to incorporate effects due to interference. A full solution of the corresponding wave equation is, however, very costly numerically and often does not provide much insight into the general features underlying a whole class of related problems. To overcome such limitations, much work has been invested into "mesoscopic scattering theory," which we provide a short review of. This term refers to a set of theoretical tools that were largely developed in the context of mesoscopic electron transport, in which the phase coherence of electrons, the finite number of modes through which they can scatter, as well as the correlations between these modes play a significant role.

Whatever the formalism chosen to describe wave propagation in disordered media, there are a few common parameters to quantify the scattering properties of the medium. The most important one is probably the transport mean free path, usually referred to as ℓ_{tr} or $\ell^\star$ in the literature (we use the notation $\ell^\star$ in this review). This length scale measures after which distance the propagation direction of an incoming photon is randomized and thus governs the macroscopic transport properties of the medium. At a more microscopic level, the scattering mean free path ℓ (or ℓ_{s} in the literature) measures the average distance traveled between two scattering events and thus quantifies the scattering strength of the medium. The link between $\ell^\star$ and ℓ is through the anisotropy of scattering $\ell^\star = \ell/(1-g)$ quantified by the anisotropy factor $g = \langle \cos\theta \rangle$, i.e., the average of the cosine of the scattering angle θ. An important case is the one of isotropic scattering, for which $\langle \cos\theta \rangle = 0$, $g = 0$, and $\ell^\star = \ell$.

A. Basic formalism

1. Wave equations

A good starting point for setting up the formalism for mesoscopic scattering is the observation that electromagnetic waves in a dielectric medium behave similarly to electrons in a potential (see also the corresponding references listed in the last paragraph of the Introduction). Since this analogy will also be the bridge across which many of the results from mesoscopic transport theory can be carried over to the domain of optics, we start here by elucidating this connection.

Consider first the Schrödinger equation for the evolution of a particle of mass m in a potential $V(\mathbf{r})$,

$$\left[\frac{\mathbf{p}^2}{2m} + V(\mathbf{r})\right]\psi(\mathbf{r},t) = i\hbar\partial_t\psi(\mathbf{r},t). \tag{1}$$

For stationary states with a well-defined real energy $E = \hbar\omega$ and a corresponding time evolution $\exp(-i\omega t)$ the Schrödinger equation reduces to the following form without a time derivative:

$$\left\{\Delta - \frac{2m}{\hbar^2}[V(\mathbf{r}) - E]\right\}\psi_E(\mathbf{r}) = 0, \tag{2}$$

where we used the standard definition for the momentum operator $\mathbf{p} = -i\hbar\boldsymbol{\nabla}$. For appropriate boundary conditions the differential operator in Eq. (2) will be Hermitian such that the eigenstates $\psi_m(\mathbf{r})$ (labeled by their mode index m) satisfy the conventional orthogonality relations

$$\int d\mathbf{r}\,\psi_m(\mathbf{r})^*\psi_n(\mathbf{r}) = \delta_{mn} \tag{3}$$

and form a complete basis of states.

To find equivalent relations also for light scattering, consider first the wave equation for the electric field $\mathbf{E}(\mathbf{r},t)$ in a source-free, linear, and frequency-independent dielectric medium with dielectric function $\varepsilon(\mathbf{r})$, which is directly derived from Maxwell's equations (Jackson, 1998),

$$-\nabla\times\nabla\times\mathbf{E}(\mathbf{r},t) = \frac{\varepsilon(\mathbf{r})}{c^2}\partial_t^2\mathbf{E}(\mathbf{r},t). \tag{4}$$

To make the analogy to the Schrödinger equation, we first restrict ourselves to monochromatic states, which, in perfect analogy to the stationary states of the Schrödinger equation, feature a harmonic time dependence $\mathbf{E}(\mathbf{r},t) = \mathbf{E}_\omega(\mathbf{r})\exp(-i\omega t)$. Unless explicitly stated otherwise, we work with this complex notation in the following with the understanding that the real (physical) electric field is extracted as the real part of this complex quantity $\mathrm{Re}[\mathbf{E}(\mathbf{r},t)]$. As it turns out, even for appropriate boundary conditions, the curl operator above is not a Hermitian operator when the dielectric function $\varepsilon(\mathbf{r})$ is spatially varying and when the conventional inner product is used (Viviescas and Hackenbroich, 2003). We thus rewrite the electric field through the vector-valued function $\boldsymbol{\phi}_\omega(\mathbf{r}) = \sqrt{\varepsilon(\mathbf{r})}\mathbf{E}_\omega(\mathbf{r})$, such that Eq. (4) can be rewritten with the Hermitian differential operator $\boldsymbol{\mathcal{L}}$,

$$\mathcal{L}\boldsymbol{\phi}_\omega(\mathbf{r}) \equiv \frac{1}{\sqrt{\varepsilon(\mathbf{r})}}\nabla\times\left[\nabla\times\frac{\boldsymbol{\phi}_\omega(\mathbf{r})}{\sqrt{\varepsilon(\mathbf{r})}}\right] = \frac{\omega^2}{c^2}\boldsymbol{\phi}_\omega(\mathbf{r}). \quad (5)$$

With appropriate boundary conditions, the eigenstates $\boldsymbol{\phi}_m(\mathbf{r})$ are then orthogonal to each other and provide a complete basis of states. As a consequence, the electric field satisfies the following orthogonality relation:

$$\int d\mathbf{r}\,\boldsymbol{\phi}_m(\mathbf{r})\boldsymbol{\phi}_n(\mathbf{r}) = \int d\mathbf{r}\,\varepsilon(\mathbf{r})\mathbf{E}_m(\mathbf{r})\mathbf{E}_n(\mathbf{r}) = \delta_{mn}. \quad (6)$$

To make the analogy to the stationary Schrödinger equation even more apparent, we simplify the curl operator with the vector identity $\nabla\times(\nabla\times\mathbf{A}) = \nabla(\nabla\cdot\mathbf{A}) - \Delta\mathbf{A}$, such that we arrive at what is termed the vectorial Helmholtz equation,

$$\left\{\Delta - \frac{\omega^2}{c^2}[1-\varepsilon(\mathbf{r})] + \frac{\omega^2}{c^2}\right\}\mathbf{E}_\omega(\mathbf{r}) = \mathbf{0}. \quad (7)$$

We emphasize at this point, however, that Eq. (7) holds only under the assumption that $\nabla\cdot\mathbf{E} = 0$ as for source-free media which are linear, homogeneous, and isotropic [in the linear regime gain and loss in the medium may be included through a complex dielectric $\varepsilon(\mathbf{r})$]. For inhomogeneous media, where the dielectric permittivity is position dependent, the wave equation (4) as well as the Helmholtz equation (7) does not hold. One may just consider the approximation of a locally homogeneous medium for which the variation of $\varepsilon(\mathbf{r})$ is slow as compared to the wavelength λ (Lifante, 2003). Alternatively, when the medium consists of piecewise homogeneous constituents, one may use the Helmholtz equation for each subpart, but different field components get mixed at the boundaries between them. We also mention here that it may computationally be more efficient to consider the magnetic field rather than the electric field in a nonmagnetic medium (Joannopoulos *et al.*, 2008).

Even the vector Helmholtz equation itself is difficult to solve for most cases and closed solutions exist only in very special limits. In practice, one therefore often reduces the Helmholtz equation to a scalar form, in which the scalar quantity $\psi_\omega(\mathbf{r})$ stands for one of the three components of the electric or magnetic field. Implicit in this strategy is the assumption that the coupling of different vectorial components does not contain important physics—a point which in many publications remains open [see, e.g., a corresponding analysis in Bittner *et al.* (2009)]. Certainly, the description of light as a scalar field may lead to quite different results than those based on a full solution of the Maxwell equations (Lagendijk and van Tiggelen, 1996; Skipetrov and Sokolov, 2014), such that a careful analysis for each individual case at hand must be recommended.

In all cases where the scalar Helmholtz equation provides a good approximation of the real physics (Kragl, 1992),

$$\left\{\Delta - \frac{\omega^2}{c^2}[1-\varepsilon(\mathbf{r})] + \frac{\omega^2}{c^2}\right\}\psi_\omega(\mathbf{r}) = 0, \quad (8)$$

all the quantities in this scalar equation for light fields can be directly compared to those of the Schrödinger equation for electrons, Eq. (2). For the case of the dielectric constant of vacuum $\varepsilon(\mathbf{r}) = 1$, or, equivalently, for the case of vanishing potential $V(\mathbf{r})$ in the Schrödinger case, we can see immediately that the resulting two equations, Eqs. (2) and (8), are the same if we identify the "light energy" as $E_{\text{light}} = (\hbar\omega)^2/(2mc^2)$ (Lagendijk and van Tiggelen, 1996). For the case of free space propagation, both equations also have the same fundamental plane wave solutions $\psi_E(\mathbf{r}) = \psi_\omega(\mathbf{r}) = \psi_{\mathbf{k},\omega}\exp(i\mathbf{k}\cdot\mathbf{r} - i\omega t)$, characterized by a single frequency ω and a single wave vector $\mathbf{k}$, where $|\mathbf{k}| = k = \omega\sqrt{\varepsilon\mu_0} = nk_0$ with n the refractive index and $k_0 = \omega/c$. In the case of a spatially nonuniform dielectric function $\varepsilon(\mathbf{r})$ or potential landscape $V(\mathbf{r})$, the scalar Helmholtz and the Schrödinger equation can still be mapped onto each other for any given frequency ω, when we identify the relation for the "light potential" $V_{\text{light}}(\mathbf{r}) = E_{\text{light}}[1-\varepsilon(\mathbf{r})]$ and keep in mind that the Helmholtz equation is valid for locally homogeneous media only (Lifante, 2003).

The equivalence between the fundamental equations, which describe electronic and light scattering, is essential for many of the effects discussed in this review and for their occurrence in both of the different research fields. Note, however, that this analogy also has well-defined limits, as, e.g., when attempting to describe the microscopic details of the scattering field in a disordered medium, which goes beyond the capacity of the Helmholtz equation and requires a full treatment based on Maxwell's equations. As seen later, for many other quantities, in particular, for those related to the statistical properties of scattering amplitudes, many common aspects in electron and light scattering can be identified.

Fundamental differences between the scattering of electrons and light do, however, remain: These become apparent, e.g., when going away from the stationary picture at a given scattering energy E or frequency ω. Because of the difference between the linear dispersion relation for light ($\omega = kc$, or, equivalently, $E \propto p$) and the quadratic dispersion for matter ($E \propto p^2$), the temporal dynamics in scattering will be very different for these two cases. Consider here the free motion of a wave packet in one dimension which satisfies Eq. (4) with the linear dispersion relation $\omega = kc/n$. In free space, where $n = 1$, both the group velocity $v_g = \partial\omega/\partial k = c$ and the phase velocity $v_\phi = \omega/k = c$ are independent of ω or k such that wave packets of light preserve their shape in vacuum. In contrast, for electronic matter waves the corresponding velocities $v_g = \hbar k/m$ and $v_\phi = \hbar k/(2m)$ depend on k, such that different frequency components of the wave packet travel with different speeds, leading to wave packet spreading even in vacuum. Furthermore, since the relation $\varepsilon(\mathbf{r}) > 1$ implies that the light potential can never exceed the light energy $V_{\text{light}} < E_{\text{light}}$, a dielectric medium can never form a tunneling barrier for light in the same way as an electrostatic potential can for electrons. Also any effects related to the vectorial character of the electric field (such as the polarization of light) have no simple analogy to the electronic case. When considering stationary scattering problems in which the polarization does not play an important role, the analogy between electron and light scattering can, however, be used extensively. At points where this analogy breaks down, this is mentioned explicitly.

2. Continuity equation and flux

The scattering of electrons and the scattering of light in a lossless, static, and linear dielectric medium have in common that a conservation relation applies,

$$\partial_t W(\mathbf{r},t) + \nabla \cdot \mathbf{J}(\mathbf{r},t) = 0. \tag{9}$$

This so-called "continuity equation" states that any temporal change of the density W must be compensated by a corresponding flux $\mathbf{J}$. For the electronic case these two quantities are given by the probability density $W(\mathbf{r},t) = |\psi(\mathbf{r},t)|^2$ and by the probability current density $\mathbf{J}(\mathbf{r},t) = \mathrm{Re}[\psi(\mathbf{r},t)^* \mathbf{p} \psi(\mathbf{r},t)]/m$, respectively. The corresponding quantities for light are the electromagnetic energy density $u(\mathbf{r},t)$ and the Poynting vector $\mathbf{S}(\mathbf{r},t)$, which fulfill the relation in Eq. (9), now termed as the "Poynting theorem," when the following replacements are made: $W(\mathbf{r},t) \to u(\mathbf{r},t) = \frac{1}{2}[\varepsilon \mathbf{E}(\mathbf{r},t)^2 + \mu^{-1}\mathbf{B}(\mathbf{r},t)^2]$ and $\mathbf{J}(\mathbf{r},t) \to \mathbf{S}(\mathbf{r},t) = \mathbf{E}(\mathbf{r},t) \times \mathbf{B}(\mathbf{r},t)/\mu$ (for which definitions we used real-valued fields $\mathbf{E}$, $\mathbf{B}$) (Griffiths, 1999). Note that these quantities are of particular importance in experiments, since what detectors typically measure is the integrated flux, counted in terms of the number of electrons or of photons that hit the detector surface (van Tiggelen and Kogan, 1994; Lagendijk and van Tiggelen, 1996).

3. Green's function

A central issue that we address in this review is the question of how the radiation emitted by a set of given sources is scattered to a set of receivers. For this purpose it is convenient to resort to the concept of the Green's function (Morse and Feshbach, 1953). We start here again with Maxwell's equations for a nonmagnetic medium described by a dielectric function $\varepsilon_\omega(\mathbf{r}) = \varepsilon^r_\omega + \varepsilon^s_\omega(\mathbf{r})$ that is embedded in an infinite homogeneous reference medium ε^r_ω. In the presence of external current sources $\mathbf{J}_\omega(\mathbf{r})$ we end up with an inhomogeneous vector Helmholtz equation of the following form (Tsang, Kong, and Ding, 2004):

$$-\nabla \times \nabla \times \mathbf{E}_\omega(\mathbf{r}) + \left(\frac{\omega}{c}\right)^2 \varepsilon_\omega(\mathbf{r}) \mathbf{E}_\omega(\mathbf{r}) = i\mu_0 \omega \mathbf{J}_\omega(\mathbf{r}), \tag{10}$$

with $\omega/c = k_0$ the vacuum wave number. When simplifying the notation in the following way $-\nabla \times \nabla \times \to \boldsymbol{\mathcal{D}}$, $k_0^2 \varepsilon^r_\omega(\mathbf{r}) \to \mathbf{e}^r$, $k_0^2 \varepsilon^s_\omega(\mathbf{r}) \to \mathbf{e}^s$, Eq. (10) is written as $(\boldsymbol{\mathcal{D}} + \mathbf{e}^r + \mathbf{e}^s)\mathbf{E} = i\mu_0\omega \mathbf{J}_\omega$. The desired Green's function $\mathbf{G}$ (which is actually a dyadic tensor) satisfies the corresponding equation $(\boldsymbol{\mathcal{D}} + \mathbf{e}^r + \mathbf{e}^s)\mathbf{G} = \delta(\mathbf{r} - \mathbf{r}')\mathbf{1}$, where we used $\mathbf{G}(\mathbf{r},\mathbf{r}',\omega) \to \mathbf{G}$, and $\mathbf{1}$ is the unit tensor. With the help of the tensorial Green's function, we may relate vectorial current sources with vectorial electric fields through a convolution,

$$\mathbf{E}_\omega(\mathbf{r}) = i\mu_0\omega \int d\mathbf{r}' \mathbf{G}(\mathbf{r},\mathbf{r}',\omega)\mathbf{J}_\omega(\mathbf{r}'). \tag{11}$$

In the case that no current sources are present in a medium, the inhomogeneity in Eq. (10) vanishes. An electric field can still be present, however, when an incident field is considered. Such a scattering problem can be treated by setting up equivalent relations for the incident field $\mathbf{E}^0$ that satisfies $(\boldsymbol{\mathcal{D}} + \mathbf{e}^r)\mathbf{E}^0 = 0$ in the homogeneous and source-free reference system. With the corresponding Green's function $\mathbf{G}^0$ satisfying $(\boldsymbol{\mathcal{D}} + \mathbf{e}^r)\mathbf{G}^0 = \delta(\mathbf{r} - \mathbf{r}')\mathbf{1}$ one finds the so-called Dyson equation $\mathbf{G} = \mathbf{G}^0 - \mathbf{G}^0\mathbf{e}_s\mathbf{G}$ and $\mathbf{E} = (\mathbf{1} - \mathbf{G}\mathbf{e}_s)\mathbf{E}^0$ (Martin, Girard, and Dereux, 1995). One thus has a generalized field propagator $\mathbf{K} = \mathbf{1} - \mathbf{G}\mathbf{e}_s$ at hand that connects the incident field with the full field distribution (including the scattered part) again through a convolution,

$$\mathbf{E}_\omega(\mathbf{r}) = \int d\mathbf{r}' \mathbf{K}(\mathbf{r},\mathbf{r}',\omega)\mathbf{E}^0_\omega(\mathbf{r}'). \tag{12}$$

Note that both Eqs. (11) and (12) are valid independently of the form of the current sources or of the incident field. The central piece of information necessary to solve these equations is the system response encapsulated in the Green's tensor $\mathbf{G}$. To obtain this quantity, one may proceed through direct inversion of the Dyson equation [$\mathbf{G}^0$ is known analytically (Morse and Feshbach, 1953)], or through iteration [corresponding iteration schemes have been put forward both for electromagnetic wave propagation (Martin, Girard, and Dereux, 1995) and for mesoscopic electron scattering (Datta, 1997; Ferry and Goodnick, 1997; Rotter *et al.*, 2000)].

In the general case of a nonuniform medium, which may also change the polarization of the electric field, the tensorial character of the Green's function is essential. The reduction to a scalar Green's function is allowed, however, when considering the emission and detection in well-defined polarization directions only (Papas, 2011).

4. Scattering matrix

A primary goal in scattering theory is to connect the incoming flux that is impinging on the system of interest to the outgoing flux scattered away from this system. A convenient tool for carrying out the corresponding bookkeeping is the scattering matrix which connects all the incoming and outgoing flux "channels" to be defined in detail later. The scattering matrix, in turn, is intimately related to the Green's function since the latter connects all points in space with each other.

To illustrate this in detail, we introduce as a model system a two-dimensional slab geometry of uniform height D with a disordered dielectric medium of length L in the middle and lossless semi-infinite waveguides of the same height attached on the left and right (see Fig. 1). This model system will serve

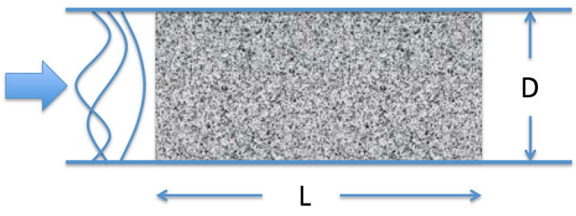

FIG. 1. Illustration of the scattering system considered in the text: A rectangular disordered region of length L fills the middle part of an infinite wave of height D. Here the flux injected from the left through transverse waveguide modes can be transmitted (to the right) or reflected (to the left).

as a convenient tool to many of the features which we want to explain below for scattering through waveguides, fibers, and disordered media in general. To simplify matters, we assume that we can use the scalar Helmholtz equation [see Eq. (8)], as for a transverse magnetic polarized electromagnetic field mode in a three-dimensional medium which is invariant in the z direction. The relevant scalar field component which we thus describe is the z component of the electric field E_z, assuming hard-wall (Dirichlet) boundary conditions at the upper and lower boundaries of the scattering domain.

In the asympotic regions (far away from the disordered part), the field in the left ($\alpha = l$) and right ($\alpha = r$) wave guide will naturally be decomposed into different waveguide modes $\chi_n(y) = \sqrt{2/D}\sin(n\pi y/D)$, as determined by the boundary conditions in the transverse direction,

$$\psi_\omega(\mathbf{x}) = \sum_{n=1}^{N} c^+_{\alpha,n}\chi_n(y)\frac{e^{ik_n^x x}}{\sqrt{k_n^x}} + c^-_{\alpha,n}\chi_n(y)\frac{e^{-ik_n^x x}}{\sqrt{k_n^x}}. \tag{13}$$

For fully defining the scattering state in the asymptotic region we summed over all $N = \lfloor \omega D/c\pi \rfloor$ flux-carrying modes for which the propagation constant $k_n^x = \sqrt{\omega^2/c^2 - (n\pi/D)^2}$ is real (evanescent modes with an imaginary propagation constant have died out asymptotically). The complex expansion coefficients $c_n^\pm$ correspond to right-moving (+) and left-moving waves (−), respectively. The terms in the denominators $\sim\sqrt{k_n^x}$ are required to make sure that all the basis states on which we expand the field have the same flux in the longitudinal direction $J_\parallel$ (see definitions in Sec. II.A.2). Based on this representation of the field in the asymptotic region, we can define the scattering matrix as the complex matrix which connects the incoming expansion coefficients with the outgoing coefficients,

$$\mathbf{c}_{\text{out}} = \mathbf{S}\mathbf{c}_{\text{in}} \quad \text{with} \quad \mathbf{c}_{\text{in}} \equiv \begin{pmatrix} \mathbf{c}_l^+ \\ \mathbf{c}_r^- \end{pmatrix}, \qquad \mathbf{c}_{\text{out}} \equiv \begin{pmatrix} \mathbf{c}_l^- \\ \mathbf{c}_r^+ \end{pmatrix}. \tag{14}$$

The $2N \times 2N$ complex coefficients in the scattering matrix can be subdivided into four block matrices,

$$\mathbf{S} = \begin{pmatrix} \mathbf{r} & \mathbf{t}' \\ \mathbf{t} & \mathbf{r}' \end{pmatrix}, \tag{15}$$

where the quadratic blocks on the diagonal contain the reflection amplitudes for incoming modes from the left (r_{mn}) and from the right (r'_{mn}), respectively. The off-diagonal blocks contain the transmission amplitudes for scattering from left to right (t_{mn}) and from right to left (t'_{mn}), respectively. Note that in the case in which the number of modes is different on the left (N) and right side (M), the reflection matrices $\mathbf{r}, \mathbf{r}'$ remain quadratic (of size $N \times N$ and $M \times M$, respectively), whereas the transmission matrices $\mathbf{t}, \mathbf{t}'$ are then just rectangular (of size $M \times N$ and $N \times M$, respectively). In this general case the total transmission T_n and reflection R_n associated with a given incoming mode n on the left read as $T_n = \sum_{m=1}^{M} |t_{mn}|^2$ and $R_n = \sum_{m=1}^{N} |r_{mn}|^2$ (equivalent relations also hold for the quantities T'_n, R'_n, T', R' with incoming modes from the right). We choose here the convention to label the incoming (outgoing) mode with the second (first) subindex in the matrices such as to coincide with the convention of matrix multiplication, i.e., $\mathbf{c}_{\text{out}} = \mathbf{S}\mathbf{c}_{\text{in}}$ is $c_{\text{out},m} = \sum_n S_{mn} c_{\text{in},n}$.

In electronic scattering the modes cannot be addressed individually, such that the relevant quantity in this context is the total transmission $T = \sum_{n=1}^{N} T_n$, corresponding to the transmission through all equally populated incoming modes from the left (similarly the total reflection $R = \sum_{n=1}^{N} R_n$). Neglecting the smearing effect of a finite temperature and counting each of the spin polarizations separately, this total transmission T can be directly related to the electronic conductance

$$G = (2e^2/h)T = (2e^2/h)\sum_{m,n}|t_{mn}|^2, \tag{16}$$

a quantity which is directly measurable in the experiment. The connection between the conductance and the transmission was first derived by Economou and Soukoulis (1981) and Fisher and Lee (1981) and is commonly known as the "Landauer formula" (Landauer, 1957). Its generalization to multiterminal systems (Büttiker, 1986) is referred to as the "Landauer-Büttiker formalism."

Since in a scattering process without gain and loss the combined value of the transmission and reflection for each mode must be 1, we can write $T_n + R_n = 1$ and $T'_n + R'_n = 1$ or, more generally, $T + R = N$ and $T' + R' = M$. These relations, together with the flux normalization of modes in Eq. (13), demonstrate the conservation of flux in systems without sources or sinks. In other words, the incoming flux in a scattering process $\sum_n |c_{\text{in},n}|^2 = |\mathbf{c}_{\text{in}}|^2$ must be equal to the outgoing flux $\sum_n |c_{\text{out},n}|^2 = |\mathbf{c}_{\text{out}}|^2$, such that

$$\mathbf{c}_{\text{out}}^\dagger \mathbf{c}_{\text{out}} = \mathbf{c}_{\text{in}}^\dagger \mathbf{c}_{\text{in}} \rightarrow \mathbf{c}_{\text{in}}^\dagger (\mathbf{S}^\dagger\mathbf{S} - \mathbf{1})\mathbf{c}_{\text{in}} = 0, \tag{17}$$

in which the relation can be fulfilled only if the scattering matrix is unitary $\mathbf{S}^\dagger\mathbf{S} = \mathbf{1}$. Inserting the block-matrix form of the scattering matrix, Eq. (15), into this unitarity condition, we arrive at the corresponding relations which the transmission and reflection matrices have to satisfy:

$$\begin{aligned} \mathbf{t}^\dagger\mathbf{t} + \mathbf{r}^\dagger\mathbf{r} &= \mathbf{t}'^\dagger\mathbf{t}' + \mathbf{r}'^\dagger\mathbf{r}' = \mathbf{1}, \\ \mathbf{r}^\dagger\mathbf{t}' + \mathbf{t}^\dagger\mathbf{r}' &= \mathbf{t}'^\dagger\mathbf{r} + \mathbf{r}'^\dagger\mathbf{t} = \mathbf{0}, \end{aligned} \tag{18}$$

as well as

$$\begin{aligned} \mathbf{t}\mathbf{t}^\dagger + \mathbf{r}'\mathbf{r}'^\dagger &= \mathbf{t}'\mathbf{t}'^\dagger + \mathbf{r}\mathbf{r}^\dagger = \mathbf{1}, \\ \mathbf{r}\mathbf{t}^\dagger + \mathbf{t}'\mathbf{r}'^\dagger &= \mathbf{t}\mathbf{r}^\dagger + \mathbf{r}'\mathbf{t}'^\dagger = \mathbf{0}, \end{aligned} \tag{19}$$

following from the alternative formulation of the unitarity condition $\mathbf{S}\mathbf{S}^\dagger = \mathbf{1}$.

The above Hermitian matrices $\mathbf{t}^\dagger\mathbf{t}, \mathbf{r}^\dagger\mathbf{r}, \mathbf{t}\mathbf{t}^\dagger, \mathbf{r}\mathbf{r}^\dagger$ and their primed counterparts play an important role in the theoretical description of multimode scattering problems. This is because they can be used to conveniently express several of the scattering quantities of interest. Consider the total

transmission T and reflection R for all incoming modes from the left, which can also be written as $T = \mathrm{Tr}(\mathbf{t}^\dagger\mathbf{t}) = \sum_n \tau_n$ and $R = \mathrm{Tr}(\mathbf{r}^\dagger\mathbf{r}) = \sum_n \rho_n$, where τ_n and ρ_n are the real eigenvalues of $\mathbf{t}^\dagger\mathbf{t}$ and $\mathbf{r}^\dagger\mathbf{r}$, respectively. Also the transmission T_n or reflection R_n of a given mode n on the left can be expressed as $T_n = (\mathbf{t}^\dagger\mathbf{t})_{nn}$, $R_n = (\mathbf{r}^\dagger\mathbf{r})_{nn}$. Note that the transmission of a lead mode T_n is different from that of a "transmission eigenchannel" τ_n, and only their sum is the same $T = \sum_n T_n = \sum_n \tau_n$ as required by the invariance of the trace. From the requirement that $\mathbf{t}^\dagger\mathbf{t} + \mathbf{r}^\dagger\mathbf{r} = \mathbf{1}$ we can further deduce that the quadratic matrices $\mathbf{t}^\dagger\mathbf{t}$ and $\mathbf{r}^\dagger\mathbf{r}$ are simultaneously diagonalizable and that their eigenvalues are related as $\tau_n = 1 - \rho_n$.

To better understand the relation between the matrices $\mathbf{t}^\dagger\mathbf{t}$ and $\mathbf{t}\mathbf{t}^\dagger$ we can write the non-Hermitian and not necessarily quadratic transmission matrix $\mathbf{t}$ in its singular value decomposition $\mathbf{t} = \mathbf{U}\Sigma\mathbf{V}^\dagger$, where the unitary matrices $\mathbf{U}$ (of size $M \times M$) and $\mathbf{V}$ (of size $N \times N$) contain, as their columns, the *left* and *right* singular vectors of $\mathbf{t}$, respectively. The matrix Σ in the center contains the real and non-negative singular values σ_i on its diagonal. These quantities are now elegantly connected to the quadratic and Hermitian matrices $\mathbf{t}^\dagger\mathbf{t}$ and $\mathbf{t}\mathbf{t}^\dagger$: The left singular vectors of $\mathbf{t}$ (contained in $\mathbf{U}$) are the orthogonal eigenvectors of $\mathbf{t}\mathbf{t}^\dagger$ and the right singular vectors of $\mathbf{t}$ (contained in $\mathbf{V}$) are the orthogonal eigenvectors of $\mathbf{t}^\dagger\mathbf{t}$. The nonzero singular values σ_i of $\mathbf{t}$ (contained in Σ) are the square roots of the nonzero eigenvalues of $\mathbf{t}^\dagger\mathbf{t}$ and $\mathbf{t}\mathbf{t}^\dagger$, i.e., $\sigma_i = \sqrt{\tau_i}$ (if these two matrices are different in size $M \neq N$, the larger matrix has at least $|M - N|$ zero eigenvalues). With the help of these identities, we can write $\mathbf{t}^\dagger\mathbf{t} = \mathbf{V}\Sigma^2\mathbf{V}^\dagger = \mathbf{V}\boldsymbol{\tau}\mathbf{V}^\dagger$ and $\mathbf{t}\mathbf{t}^\dagger = \mathbf{U}\Sigma^2\mathbf{U}^\dagger = \mathbf{U}\boldsymbol{\tau}\mathbf{U}^\dagger$, where the diagonal matrix $\boldsymbol{\tau}$ contains the transmission eigenvalues from above on its diagonal $\boldsymbol{\tau} = \mathrm{diag}(\tau_1, \ldots, \tau_M)$. From these identities we can conclude that $\mathbf{t}^\dagger\mathbf{t}$ and $\mathbf{t}\mathbf{t}^\dagger$ share the same eigenvalues (except for $|M - N|$ zero eigenvalues) and due to the identities Eqs. (18) and (19) these eigenvalues are also the same as those of the matrices $\mathbf{t}'^\dagger\mathbf{t}'$, $\mathbf{t}'\mathbf{t}'^\dagger$, $\mathbf{1} - \mathbf{r}^\dagger\mathbf{r}$, $\mathbf{1} - \mathbf{r}\mathbf{r}^\dagger$, and $\mathbf{1} - \mathbf{r}'^\dagger\mathbf{r}'$, $\mathbf{1} - \mathbf{r}'\mathbf{r}'^\dagger$.

Additional, so-called reciprocity relations (also called Onsager relations) can be obtained for the scattering matrix (Jalas *et al.*, 2013). In terms of the transmission and reflection matrix elements, reciprocity translates into an identity between the amplitude for scattering from mode m to another mode n and the amplitude for the reverse process (i.e., from mode n to mode m): $r_{nm} = r_{mn}$, $r'_{nm} = r'_{mn}$, and $t_{nm} = t'_{mn}$, corresponding to a transposition-symmetric scattering matrix $\mathbf{S} = \mathbf{S}^\mathrm{T}$. Similar reciprocity relations can also be derived for generalized transmission and reflection coefficients (Nieto-Vesperinas and Wolf, 1986). Generally speaking, these relations tell us that if one can scatter from a mode m to another mode n then the reverse process also happens with the same amplitude. One may be tempted to associate this property with time-reversal symmetry, which is, however, misleading. Time-reversal symmetry implies reciprocity, but not the other way around. The best example to illustrate this fact is a medium with absorption, for which time-reversal symmetry is obviously broken but the reciprocity relations may still hold (van Tiggelen and Maynard, 1997). Breaking the reciprocity of a medium typically requires a time-dependent dielectric function, nonlinear effects, or a magnetic field (Jalas *et al.*, 2013).

Our choice to evaluate the scattering matrix $\mathbf{S}$ in the lead-mode basis χ_n is arbitrary and other basis sets can be more useful for addressing particular problems. A natural basis, in which the scattering matrix is diagonal is, of course, its eigenbasis,

$$\mathbf{S} = \Omega\,\mathrm{diag}(e^{i\phi_1}, \ldots, e^{i\phi_{2N}})\Omega^\dagger. \tag{20}$$

Being a unitary matrix, the eigenvalues of $\mathbf{S}$ lie on the unit circle in the complex plane and can be parametrized, using the so-called scattering phase shifts ϕ_n. The transformation to the eigenbasis is mediated by the unitary matrix Ω which contains the eigenvectors of $\mathbf{S}$. In the presence of time-reversal symmetry where the scattering matrices are transposition symmetric, Ω can be chosen real and is then an orthogonal matrix $\Omega^\mathrm{T}\Omega = \mathbf{1}$.

This parametrization of the scattering matrix has the disadvantage that the modes on the left and right of the sample are strongly mixed as eigenvectors of $\mathbf{S}$ typically feature components from all modes, irrespective of their asymptotic behavior. An alternative parametrization which disentangles the modes on the left and right sides was proposed by Mello, Pereyra, and Kumar (1988) and Martin and Landauer (1992). This so-called "polar decomposition" is based on the singular value decomposition of the scattering matrix blocks and reads as follows:

$$\mathbf{S} = \begin{pmatrix} \mathbf{V} & \mathbf{0} \\ \mathbf{0} & \mathbf{U} \end{pmatrix} \begin{pmatrix} -\sqrt{\mathbf{1}-\boldsymbol{\tau}} & \sqrt{\boldsymbol{\tau}} \\ \sqrt{\boldsymbol{\tau}} & \sqrt{\mathbf{1}-\boldsymbol{\tau}} \end{pmatrix} \begin{pmatrix} \mathbf{V}' & \mathbf{0} \\ \mathbf{0} & \mathbf{U}' \end{pmatrix}. \tag{21}$$

In the general case the primed matrices satisfy $\mathbf{U}' = \mathbf{U}^\dagger$, $\mathbf{V}' = \mathbf{V}^\dagger$, and in the presence of time-reversal symmetry one has $\mathbf{U}' = \mathbf{U}^\mathrm{T}$, $\mathbf{V}' = \mathbf{V}^\mathrm{T}$. The transformation from the lead modes to the transmission eigenchannels of $\mathbf{t}^\dagger\mathbf{t}$ and $\mathbf{t}\mathbf{t}^\dagger$ has the advantage that the scattering amplitudes on either side of the medium stay well separated but their interrelation becomes maximally transparent.

The scattering matrix $\mathbf{S}$ which relates the flux amplitudes of incoming to outgoing modes at a fixed scattering frequency ω shares a very close relationship (Fisher-Lee relation) with the corresponding retarded Green's function G^+ at the same value of ω (Fisher and Lee, 1981) [see Datta (1997) and Ferry and Goodnick (1997) for a review]. This close connection is well exemplified by considering the scattering matrix elements corresponding to incoming modes from the left,

$$t_{nm}(\omega) = -i\sqrt{k_m^x k_n^x}\int_0^D dy_l \times \int_0^D dy_r\, \chi_m(y_l) G^+(y_l, y_r, \omega)\chi_n(y_r), \tag{22}$$

$$r_{nm}(\omega) = \delta_{nm} - i\sqrt{k_m^x k_n^x}\int_0^D dy'_l \times \int_0^D dy_l\, \chi_m(y'_l) G^+(y'_l, y_l, \omega)\chi_n(y_l), \tag{23}$$

where the appearing integrals are evaluated along a transverse section in the left (y_l) and the right (y_r) leads. The

corresponding relations for incoming modes from the right lead is fully equivalent. The flux normalization factors $\sqrt{k_n^x}$, which are necessary to convert field amplitudes into flux amplitudes, correspond to the direction cosines in the Fresnel-Kirchhoff diffraction theory (Born and Wolf, 1999).

Based on this, it is interesting to take note of the difference in the information content between the Green's function and the scattering matrix: Whereas the Green's function along the considered sections contains an infinite set of propagation amplitudes from any point on the transverse section to any other point, the scattering matrix relates only the finite and discrete set of flux-carrying modes to one another. The reduced information content in the scattering matrix is due to the neglect of evanescent modes which carry no flux and thus also do not contribute to transport. Note, however, that evanescent modes play a crucial role in the near field of the scattering region where they need to be taken into account if the field distribution close to the scattering region is of interest. Correspondingly, extended definitions of the scattering matrix as well as of their unitarity and reciprocity relations that also include evanescent modes have been put forward by Carminati *et al.* (2000).

Since Eqs. (22) and (23) provide a relation between the scattering matrix $\mathbf{S}$ and the scalar Green's function $G^+(\mathbf{r},\mathbf{r}',\omega)$ and the latter is, in turn, related to the Helmholtz operator $\boldsymbol{\mathcal{L}}$ defined in Eq. (5), there should also exist a direct link between $\mathbf{S}$ and $\boldsymbol{\mathcal{L}}$. To uncover this relation one first subdivides space into an interior (scattering) region $\mathcal{Q}$, where $\varepsilon(\mathbf{r})$ may vary in space, and an exterior (asymptotic) region $\mathcal{P}$ with a constant $\varepsilon(\mathbf{r})$, where the scattering matrix $\mathbf{S}$ is evaluated. Following the so-called Feshbach projection operator technique (Feshbach, 1958, 1962) [see Zaitsev and Deych (2010) for a review], such a subdivision is carried out with corresponding projection operators,

$$\boldsymbol{\mathcal{Q}} = \int_{\mathbf{r}\in\mathcal{Q}} |\mathbf{r}\rangle\langle\mathbf{r}|, \qquad \boldsymbol{\mathcal{P}} = \int_{\mathbf{r}\in\mathcal{P}} |\mathbf{r}\rangle\langle\mathbf{r}|, \tag{24}$$

which project onto the corresponding regions and satisfy $[\boldsymbol{\mathcal{P}},\boldsymbol{\mathcal{Q}}]=0$, $\boldsymbol{\mathcal{P}}+\boldsymbol{\mathcal{Q}}=\mathbf{1}$. With these operators, we can write Eq. (5) in the equivalent form as

$$\begin{pmatrix} \boldsymbol{\mathcal{L}}_{\mathcal{Q}\mathcal{Q}} & \boldsymbol{\mathcal{L}}_{\mathcal{Q}\mathcal{P}} \\ \boldsymbol{\mathcal{L}}_{\mathcal{P}\mathcal{Q}} & \boldsymbol{\mathcal{L}}_{\mathcal{P}\mathcal{P}} \end{pmatrix} \begin{pmatrix} \boldsymbol{\mu}_\omega \\ \boldsymbol{\nu}_\omega \end{pmatrix} = \frac{\omega^2}{c^2} \begin{pmatrix} \boldsymbol{\mu}_\omega \\ \boldsymbol{\nu}_\omega \end{pmatrix}, \tag{25}$$

where the Hermitian diagonal matrix blocks $\boldsymbol{\mathcal{L}}_{\mathcal{Q}\mathcal{Q}} = \boldsymbol{\mathcal{L}}_{\mathcal{Q}\mathcal{Q}}^\dagger$, $\boldsymbol{\mathcal{L}}_{\mathcal{P}\mathcal{P}} = \boldsymbol{\mathcal{L}}_{\mathcal{P}\mathcal{P}}^\dagger$ are the projections of $\boldsymbol{\mathcal{L}}$ into the scattering and asymptotic regions, respectively, and the non-Hermitian off-diagonal blocks $\boldsymbol{\mathcal{L}}_{\mathcal{Q}\mathcal{P}}^\dagger = \boldsymbol{\mathcal{L}}_{\mathcal{P}\mathcal{Q}}$ are the coupling operators between these two regions. The reduced Hermitian operators are now used to define eigenvalue problems in the spaces $\mathcal{Q}$ and $\mathcal{P}$,

$$\boldsymbol{\mathcal{L}}_{\mathcal{Q}\mathcal{Q}}\boldsymbol{\mu}_m = \frac{\omega_m^2}{c^2}\boldsymbol{\mu}_m \quad \text{and} \quad \boldsymbol{\mathcal{L}}_{\mathcal{P}\mathcal{P}}\boldsymbol{\nu}_{n,\omega} = \frac{\omega^2}{c^2}\boldsymbol{\nu}_{n,\omega}. \tag{26}$$

Because of the confinement of states $\boldsymbol{\mu}_m$ in $\mathcal{Q}$ the corresponding eigenvalues ω_m are discrete, whereas the eigenvalues ω in the unconfined asymptotic regions are continuous (n is just a channel index in this case). In both regions $\mathcal{P}$, $\mathcal{Q}$ the eigenfunctions form a complete set and can thus be used to expand modes of arbitrary complexity in the respective subspaces. The interface between $\mathcal{P}$ and $\mathcal{Q}$ can be chosen anywhere in the asymptotic region and also the boundary conditions on $\mathcal{Q}$ are arbitrary but should be such that the operator $\boldsymbol{\mathcal{L}}_{\mathcal{Q}\mathcal{Q}}$ is Hermitian (with Dirichlet or Neumann boundary conditions being the standard choices). If needed, the boundary between $\mathcal{P}$ and $\mathcal{Q}$ can also be placed in the direct vicinity of the scattering region, in which case the coupling to evanescent modes needs to be properly taken into account (Viviescas and Hackenbroich, 2003).

To make the connection with the scattering matrix $\mathbf{S}$ we place the boundary between $\mathcal{P}$ and $\mathcal{Q}$ outside the sections where the scattering matrix is being evaluated in Eq. (23). It can be shown in this case (Mahaux and Weidenmüller, 1969) [see Datta (1997), Guhr, Müller-Groeling, and Weidenmüller (1998), and Rotter (2009) for a review] that the retarded Green's function $G^+(\mathbf{r},\mathbf{r}',\omega)$ appearing in Eq. (23) with $\mathbf{r},\mathbf{r}'\in\mathcal{Q}$ can then again be written as a resolvent $\mathbf{G}_{\mathcal{Q}\mathcal{Q}} = [\omega^2 - \boldsymbol{\mathcal{L}}_{\text{eff}}]^{-1}$, with the help of an effective non-Hermitian operator $\boldsymbol{\mathcal{L}}_{\text{eff}} = \boldsymbol{\mathcal{L}}_{\mathcal{Q}\mathcal{Q}} + \Sigma(\omega)$. The so-called self-energy $\Sigma(\omega)$ can be written as

$$\Sigma(\omega) = \boldsymbol{\mathcal{L}}_{\mathcal{Q}\mathcal{P}}(\omega)\frac{1}{\omega^2 - \boldsymbol{\mathcal{L}}_{\mathcal{P}\mathcal{P}}(\omega) + i\varepsilon}\boldsymbol{\mathcal{L}}_{\mathcal{P}\mathcal{Q}}(\omega), \tag{27}$$

with ε being here an infinitesimal positive number. Through this self-energy the Green's function $\mathbf{G}^0_{\mathcal{Q}\mathcal{Q}} = [\omega^2 - \boldsymbol{\mathcal{L}}_{\mathcal{Q}\mathcal{Q}}]^{-1}$ of the closed region $\mathcal{Q}$ (the superscript 0 denotes the absence of coupling to $\mathcal{P}$) turns into the Green's function of the corresponding open system $\mathbf{G}_{\mathcal{Q}\mathcal{Q}} = [\omega^2 - \boldsymbol{\mathcal{L}}_{\mathcal{Q}\mathcal{Q}} + \Sigma(\omega)]^{-1}$ (where the coupling to $\mathcal{P}$ is included). Because of its restriction to the interface between $\mathcal{P}$ and $\mathcal{Q}$ the self-energy is nothing else than a non-Hermitian boundary condition which parametrically depends on the real scattering frequency ω in the outside domain $\mathcal{P}$. This boundary condition is known under the name of Kapur-Peierls or constant-flux boundary condition (Kapur and Peierls, 1938; Türeci, Stone, and Collier, 2006) with the latter terminology being motivated by the fact that the outgoing flux in $\mathcal{P}$ is conserved (corresponding to a real value of ω). In the context of quantum scattering, the operator $\boldsymbol{\mathcal{L}}_{\text{eff}}$ is also known as the "effective" or non-Hermitian Hamiltonian. Being non-Hermitian, the operator $\boldsymbol{\mathcal{L}}_{\text{eff}}$ has complex eigenvalues, corresponding to eigenstates which decay through the system boundaries and thus have only a finite lifetime.

To establish the link between $\boldsymbol{\mathcal{L}}_{\text{eff}}$ and the scattering matrix $\mathbf{S}$ we need to express the operators in the basis vectors of the regions $\mathcal{P}$ and $\mathcal{Q}$, respectively. For the closed system operator $\boldsymbol{\mathcal{L}}_{\mathcal{Q}\mathcal{Q}}$ the matrix elements are $H_{\lambda m} = \langle\boldsymbol{\mu}_\lambda|\boldsymbol{\mathcal{L}}_{\mathcal{Q}\mathcal{Q}}|\boldsymbol{\mu}_m\rangle = \omega_m^2\delta_{\lambda m}$ and for the self-energy we get $\Sigma_{\lambda m}(\omega) = -2\Delta_{\lambda m}(\omega) - 2i\pi(\mathbf{W}\mathbf{W}^\dagger)_{\lambda m}(\omega)$, where the real matrix elements $\Delta_{\lambda m}$ contain frequency shifts and the Hermitian matrix $\mathbf{W}\mathbf{W}^\dagger$ contains damping terms resulting from the coupling between the bounded region $\mathcal{Q}$ with the continuum region $\mathcal{P}$, i.e., $W_{\lambda m}(\omega) = \langle\boldsymbol{\mu}_\lambda|\boldsymbol{\mathcal{L}}_{\mathcal{Q}\mathcal{P}}|\boldsymbol{\nu}_m(\omega)\rangle\sqrt{k_m^x}$. These matrix elements that can be calculated analytically for simple systems (Viviescas and Hackenbroich, 2003) or numerically for complex geometries (Stöckmann *et al.*, 2002; Sadreev and

Rotter, 2003) allow us to write the effective operator $\mathcal{L}_{\text{eff}} = \mathcal{L}_{\mathcal{QQ}} - 2\mathbf{\Delta} - 2i\pi\mathbf{W}\mathbf{W}^{\dagger}$ and with it the scattering matrix in mode representation (Mahaux and Weidenmüller, 1969)

$$S_{mn}(\omega) = \delta_{mn} - 2i\left[\mathbf{W}^{\dagger}(\omega)\frac{1}{\omega^2 - \mathcal{L}_{\text{eff}}(\omega)}\mathbf{W}(\omega)\right]_{mn}, \quad (28)$$

which represents the desired relation between the scattering matrix and the differential operator $\mathcal{L}$ introduced at the beginning of this section; see Eq. (5).

An interesting correspondence that can be established based on Eq. (28) is that between the poles of the Green's function $\mathbf{G}_{\mathcal{QQ}}$ and the resonances in the transmission and reflection amplitudes in the scattering matrix $\mathbf{S}(\omega)$. The complex frequency values ω at which these poles are located are implicitly defined through the eigenvalues $\Omega_k(\omega)$ of $\mathcal{L}_{\text{eff}}(\omega)$, which have to satisfy $\omega^2 - \Omega_k^2(\omega) = 0$. To find the solutions of this equation one can iteratively track the values of ω from the real axis to the desired fixed point for each specific eigenvalue Ω_k. The complex resonance values found in this way play an important role for scattering problems, as their real parts specify the positions of scattering resonances and their imaginary parts fix the corresponding resonance widths, which, in turn, are inversely proportional to the decay time of a resonant state in this open system. Because of their finite lifetime the resonances are also often referred to as quasibound states or quasimodes of the system and starting from the original work by Gamow (1928) many theoretical studies are based on these states (Moiseyev, 2011). In contrast to the constant-flux states, the quasibound states do, however, have the problem that they diverge to infinity outside of the system boundaries, which requires much care when using them to expand a field in this set of states (Ching *et al.*, 1998). On the other hand, quasibound states do not feature a parametric dependence on the frequency outside the system (as the constant-flux states do), since for the quasibound states both of the involved frequencies are equal: $\omega_k = \Omega_k$.

5. Random matrix theory

A convenient tool to understand the statistical rather than the system-specific properties of scattering processes in disordered media is RMT. The basic assumption underlying RMT is that the statistical properties of a sufficiently chaotic or disordered system are the same as those of a suitably chosen ensemble of random matrices. This idea, which was originally introduced by Wigner to model the distribution of energy spacings in nuclei (Wigner, 1955a), has meanwhile found a broad range of applications, not only in nuclear physics (Weidenmüller and Mitchell, 2009; Mitchell, Richter, and Weidenmüller, 2010), but also in mesoscopic physics (Beenakker, 1997) and increasingly so in disordered photonics (Beenakker, 2011). The broad applicability of RMT (Stöckmann, 2006) is strongly linked to the so-called Bohigas-Giannoni-Schmitt (BGS) conjecture (Bohigas, Giannoni, and Schmit, 1984) according to which RMT describes well the spectral statistics of any "quantum" or "wave" system (governed by a wave equation) whose "classical" counterpart (governed by a corresponding Hamiltonian equation of motion) is *chaotic*. Classically, such chaotic systems are characterized by having more degrees of freedom than constants of motion. Quantum mechanically this translates into having more degrees of freedom than good quantum numbers. Finding a proof for the BGS conjecture has turned out to be very difficult [proofs in certain limits have meanwhile been proposed (Müller *et al.*, 2004)]. Extensive theoretical and experimental work (Beenakker, 1997) has, however, shown that the BGS conjecture is well satisfied in many different physical scenarios not only for mesoscopic quantum systems and the corresponding matter waves, but for many other types of waves as well (such as optical, acoustic, and microwaves) (Gräf *et al.*, 1992; Ellegaard *et al.*, 1995; Guhr, Müller-Groeling, and Weidenmüller, 1998; Stöckmann, 2006; Dietz and Richter, 2015). Furthermore, based on the analogies (see Sec. II.A.1) between quantum systems (described by a Schrödinger equation) and optical scattering systems (described by a Helmholtz equation) many of the results that have been explored in the field of mesoscopic physics can now be carried over to the domain of optical scattering. Before demonstrating this explicitly by means of concrete examples (see Sec. III), we first review the basic theoretical concepts of RMT.

Our starting point for applying RMT to the systems considered in this review is the approach by Wigner and Dyson (Wigner, 1955a), which consists of replacing the matrix representation of the differential operator $\mathcal{L}_{\mathcal{QQ}}$ in Eqs. (25) and (26) for a specific closed system $\mathcal{Q}$ by a random matrix $\mathbf{H}$. The latter contains as each of its elements H_{mn} a randomly generated number from an ensemble with the Gaussian distribution $P(H_{mn}) = (w\sqrt{2\pi})^{-1}\exp[-H_{mn}^2/(2w^2)]$ and zero average $\langle H_{mn}\rangle = 0$ (the value of w determines the mean level spacing of the corresponding eigenvalues). Since the matrix elements H_{mn} can, in general, be complex, we may choose both the real and imaginary parts from this Gaussian ensemble independently. The only additional constraint that is imposed on the matrix elements H_{mn} is that they are those of a Hermitian matrix $\mathbf{H}^{\dagger} = \mathbf{H}$, i.e., $H_{mn}^* = H_{nm}$. For a time-reversal-symmetric system, the matrix elements are real and symmetric, i.e., $H_{mn} = H_{nm} \in \mathbb{R}$. Having replaced the differential operator $\mathcal{L}_{\mathcal{QQ}}$ by a random matrix $\mathbf{H}$, all system-specific information about $\mathcal{Q}$ is lost and only statements on the statistical properties of a whole class of systems can be made that can be associated with the same Gaussian ensemble of matrices (Porter, 1965) [see Mehta (2004) for a review]. For the Hermitian matrices with complex, Gaussian-distributed elements this ensemble is called the Gaussian unitary ensemble (GUE). The term *unitary* refers here to the unitary matrices containing the eigenvectors of these Hermitian matrices. Similarly, the symmetric matrices with real, Gaussian-distributed elements are referred to as the Gaussian orthogonal ensemble (GOE), where *orthogonal* refers to the corresponding orthogonal eigenvector matrix. It can now be shown that each of these matrix ensembles has a specific distribution of eigenvalues. In particular, when we take Gaussian random matrices of very large size ($N \to \infty$) and compute the set of eigenvalues E_α, their distribution will be universal in the average over many matrix realizations. The corresponding distribution function for the eigenvalues

$$P(\{E_n\}) \approx \text{const} \times \prod_{m<n}^{N} |E_n - E_m|^{\beta} \prod_{n}^{N} \exp[-E_n^2/(2w^2)] \tag{29}$$

is known as the Wigner-Dyson distribution, following the original work by Wigner (1957, 1967) and Dyson (1962a). The parameter β here is assigned the value $\beta = 1$ for GOE and $\beta = 2$ for GUE. An interesting result contained in this distribution is the repulsion of nearby levels, i.e., $P(\delta) \to 0$ for $\delta \to 0$. More specifically, when considering the normalized spacing between nearest eigenvalues $\delta = (E_{\alpha+1} - E_\alpha)/\Delta$ with the mean level spacing $\Delta = \langle E_{\alpha+1} - E_\alpha \rangle$ then one finds that the level repulsion scales like $P(\delta \ll 1) \propto \delta^{\beta}$. Comparing this result with experimental data both for time-reversal invariant systems with $\beta = 1$ [see Fig. 2(a)] and for systems without time-reversal symmetry and $\beta = 2$ [see Fig. 2(b)] shows good agreement. Note that the results shown in Fig. 2 stem from very different physical systems, like an atomic nucleus in Fig. 2(a) and a microwave billiard with an attached isolator in Fig. 2(b).

To investigate how these results for bounded systems carry over to the case of unbounded scattering systems, we follow the so-called "Heidelberg approach" (Mahaux and Weidenmüller, 1969) [see Guhr, Müller-Groeling, and Weidenmüller (1998) for a review]. Here the random Hamiltonian matrix $\mathbf{H}$ describing the bounded region ($\mathcal{Q}$) is coupled to the unbounded outside domain ($\mathcal{P}$) by way of the frequency-dependent coupling matrices $W_{\lambda,m}(\omega)$ introduced in Sec. II.A.4. Using Eq. (28) then yields the corresponding scattering matrix for transmission and reflection through the region described by the Hamiltonian $\mathbf{H}$. Note that in this approach no approximation is introduced by the subdivision of space into $\mathcal{P}$ and $\mathcal{Q}$. When one is interested in the statistical properties of the scattering matrix, a less rigorous calculation is usually sufficient. A common approximation is to neglect the frequency dependence of the coupling matrix elements

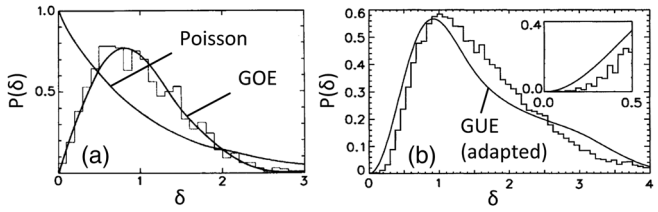

FIG. 2. (a) Comparison of the nearest neighbor level spacing distribution $P(\delta)$ in a set of nuclear scattering resonances (histogram) with the corresponding RMT prediction from the Gaussian orthogonal ensemble (GOE) for time-reversal invariant systems. The very good agreement found confirms that the statistical property of nuclei can be approached through RMT. For comparison the prediction from a Poisson distribution is also shown, corresponding to uncorrelated levels. Adapted from Bohigas, Haq, and Pandey, 1983. (b) Level spacing distribution in a quasi-two-dimensional microwave billiard with an isolator attached. Here the data are well described by the Gaussian unitary ensemble (GUE). The solid line is adapted to account for missing levels and the inset shows the quadratic increase of the level repulsion for small values as characteristic for GUE. Adapted from Stoffregen *et al.*, 1995.

$W_{\lambda,m}(\omega)$, which are then drawn from an ensemble of random numbers, just like the matrix elements of $\mathbf{H}$.

In this approach, which has found interesting applications in nuclear scattering (Verbaarschot, Weidenmüller, and Zirnbauer, 1985; Iida, Weidenmüller, and Zuk, 1990a, 1990b), the only frequency dependence in the scattering matrix comes from the ω^2 term in Eq. (28). This explicit frequency dependence is essential as it can be used to study frequency correlations in the scattering matrix elements (Guhr, Müller-Groeling, and Weidenmüller, 1998). Consider here, in particular, that the bound eigenstates of the Hamiltonian $\mathbf{H}$ are coupled by the matrix elements $W_{\lambda,m}(\omega)$ to the waveguide modes, which turns these states into quasibound resonances (as discussed at the end of Sec. II.A.4). Depending on whether the coupling strength [as determined by the matrix elements $W_{\lambda,m}(\omega)$] is smaller or larger than the mean level spacing of the Hamiltonian eigenstates (as determined by the variance of the matrix elements H_{mn}) these resonances will be isolated (weak coupling) or overlapping (strong coupling), resulting in very different frequency correlations in the scattering matrix elements [see also Brouwer (1995) for more details on the situation with nonideal waveguide coupling].

A different strategy to set up a random matrix theory for coherent scattering, also known as the "Mexico approach," starts not with the Hamiltonian $\mathbf{H}$, but with the scattering matrix $\mathbf{S}$ as the fundamental quantity (Friedman and Mello, 1985a, 1985b; Mello, Pereyra, and Seligman, 1985; Baranger and Mello, 1994; Jalabert, Pichard, and Beenakker, 1994). In this approach (Alhassid, 2000), which was developed independently of the Heidelberg approach, one replaces the scattering matrix elements by random complex numbers. In analogy to the random Hamiltonian matrix elements, which had to be chosen such as to respect the Hermiticity of the Hamiltonian, the random scattering matrix elements have to respect the unitarity of the scattering matrix. In the case of time-reversal symmetry, the scattering matrix additionally has to be symmetric (see discussion in Sec. II.A.4). The corresponding matrix ensembles are referred to as Dyson's circular ensemble (Dyson, 1962b) with the parameter $\beta = 1$ assigned to unitary symmetric and $\beta = 2$ for general unitary matrices. Assuming such a distribution leads to very specific correlations in the scattering phase shifts in Eq. (20),

$$P(\{\phi_n\}) \propto \prod_{n<m} |\exp(i\phi_n) - \exp(i\phi_m)|^{\beta}, \tag{30}$$

which were found by Blümel and Smilansky (1990) to describe the phase shifts in chaotic scattering very well. To link the circular ensemble to experimentally more accessible quantities like the statistics of transmission and reflection, the corresponding distribution of the transmission eigenvalues τ_n of the matrices $\mathbf{t}^\dagger\mathbf{t}$ and $\mathbf{t}\mathbf{t}^\dagger$ needs to be evaluated (Baranger and Mello, 1994; Jalabert, Pichard, and Beenakker, 1994). The corresponding joint probability density of transmission eigenvalues is given as follows:

$$P(\{\tau_n\}) \propto \prod_{n<m} |\tau_n - \tau_m|^{\beta} \times \prod_{p} \tau_p^{-1+\beta/2}. \tag{31}$$

The product between neighboring transmission eigenvalues leads to a level repulsion similar to the repulsion of energy eigenvalues of the random Hamiltonian $\mathbf{H}$. Note, however, that Eq. (31) also applies for the case of just a few scattering channels N down to the single-channel case where $N = 1$.

This result already contains very interesting physics. Consider the limiting case of the distribution for a very large number of scattering channels ($N \to \infty$), broken down to the one-point probability density of transmission eigenvalues $P(\tau)$. The latter is given as the mean value of the microscopic density $\rho(\tau) = \sum_n^N \delta(\tau - \tau_n)$ with respect to the ensemble average according to the probability distribution

$$P(\tau) \equiv \langle \rho(\tau) \rangle = \int_0^1 d\tau_1 \cdots \int_0^1 d\tau_N P(\{\tau_n\}) \rho(\tau), \tag{32}$$

resulting in the following bimodal distribution for the limit $N \gg 1$ illustrated in Fig. 3(a) (Baranger and Mello, 1994; Jalabert, Pichard, and Beenakker, 1994),

$$P(\tau) = \frac{1}{\pi \sqrt{\tau(1-\tau)}}. \tag{33}$$

Results for small N or for an asymmetric number of channels on the left and right are provided by Savin and Sommers (2006). Note that in the case of broken time-reversal symmetry ($\beta = 2$) for which Eq. (33) was derived, the distribution $P(\tau)$ is symmetric around $\tau = 1/2$. For the time-reversal symmetric case ($\beta = 1$), however, the second product in Eq. (31) induces an asymmetry into this distribution which leads to the following results for the average transmission (Baranger and Mello, 1994; Jalabert, Pichard, and Beenakker, 1994):

$$\langle T \rangle = \frac{N}{2} + \left(\frac{1}{4} - \frac{1}{2\beta} \right) + \mathcal{O}(1/N). \tag{34}$$

The reduction in transmission for $\beta = 1$ is called the *weak-localization* correction, which in a semiclassical picture can be partially associated with the presence of time-reversed path pairs that enhance the reflection R (hence the name "localization"). The term "weak" refers here to the fact that the correction is of the order of $\mathcal{O}(1)$, which is much smaller than the leading term $\mathcal{O}(N)$. Experimental demonstrations of this effect are discussed in Sec. III.C.

The first product in Eq. (31) involving pairs of transmission eigenvalues suppresses the likelihood of neighboring transmission eigenvalues approaching each other very closely. This eigenvalue repulsion leads also to a spacing distribution between nearest neighbor transmission eigenvalues which scales like $P(\delta \ll 1) \propto s^\beta$, where the normalized spacing is given by $\delta = (\tau_{m+1} - \tau_m)/\Delta$, with $\Delta = \langle \tau_{m+1} - \tau_m \rangle$. Note the similarity here with the spacing distribution obtained earlier for the eigenvalues of a random Hamiltonian; see Eq. (29). Because of this "spectral rigidity" the transmission eigenvalues fluctuate only between the limits imposed by their neighboring values, which is much less than for uncorrelated transmission eigenvalues described by a Poisson distribution $P(\delta \ll 1) \propto \exp(-\delta/\Delta)$. This suppression of fluctuations is so strong that the variance of the fluctuations in the total transmission [as defined below Eq. (15)] approaches a universal, but β-specfic value (Lee and Stone, 1985), which is of the order of $\mathcal{O}(1)$ and thus independent of N,

$$\mathrm{var}T = \frac{1}{8\beta}. \tag{35}$$

This prediction for universal conductance fluctuations in a chaotic cavity was obtained with the Heidelberg approach for the Hamiltonian by Verbaarschot, Weidenmüller, and Zirnbauer (1985) and Iida, Weidenmüller, and Zuk (1990a, 1990b) and with the Mexico approach for the scattering matrix by Baranger and Mello (1994) and Jalabert, Pichard, and Beenakker (1994). An extended discussion of universal conductance fluctuations can be found in Sec. III.B.

Another highly nontrivial aspect of coherent chaotic scattering is contained in the shape of the distribution function of transmission eigenvalues [see Fig. 3(a)]: Contrary to what one would naively expect, the transmission eigenvalues τ_n are not uniformly distributed between the limiting values 0 and 1; instead, Eq. (33) predicts that the τ_n are peaked near 0 and 1, corresponding to transmission channels that are almost closed (near $\tau \approx 0$) and others that are almost open (near $\tau \approx 1$)—a phenomenon also known as "maximal fluctuation theorem" (Pendry, MacKinnon, and Pretre, 1990). These open and closed transmission eigenchannels (see Fig. 3) which were first discovered by Dorokhov (1984) will play an important role for many of the effects discussed in this review. To understand the origins of the bimodal distribution consider the repulsion of transmission eigenvalues inherent in Eq. (31). The closer a given transmission eigenvalue is to 0 (to 1), the more it is repelled by its higher (lower) neighbors (simply because there are more of them). Together with the restriction to the inverval $\tau \in [0, 1]$, this leads to the clustering near the limiting values 0 and 1. It is also instructive to compare the RMT distribution for $P(\tau)$ with the distribution which one would get for the scattering of classical particles rather than of waves. Since particles (like billiard balls) that enter a scattering region connected to a left and right port can be either fully reflected or fully transmitted, but nothing in between, the corresponding classical distribution function has two delta peaks $P_{\mathrm{cl}}(\tau) = \alpha\delta(\tau) + (1-\alpha)\delta(1-\tau)$, with $\alpha = 1/2$ when assuming the probability for transmission and for reflection to be equal. We can thus conclude that the RMT distribution for the transmission eigenvalues is peaked at exactly those values of transmission which are classically allowed. In turn, only a

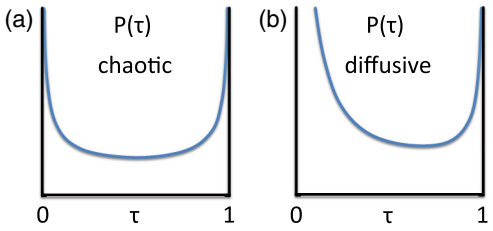

FIG. 3. Distribution of transmission eigenvalues τ for the cases of (a) chaotic scattering and (b) diffusive scattering. The corresponding analytical expressions for these functions (following from random matrix theory) are given in Eqs. (33) and (40), respectively.

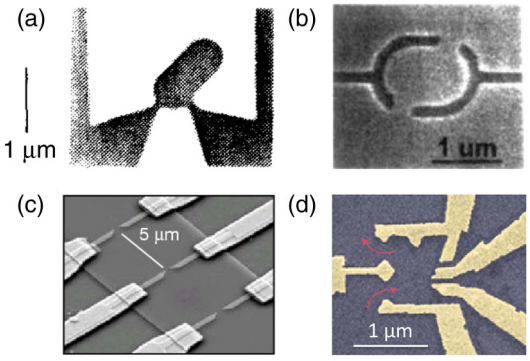

FIG. 4. Different experimental realizations of chaotic quantum dots. In all four cases these electronic billiards are fabricated based on a semiconductor heterostructure with high mobility. The current between the source and drain enters and exits through slits (quantum point contacts), which are small compared to the overall dimension of the chaotic scattering region in between. Adapted from (a) Marcus *et al.*, 1992, (b) Chang *et al.*, 1994, (c) Oberholzer, Sukhorukov, and Schönenberger, 2002, and (d) Marcus *et al.*, 1997.

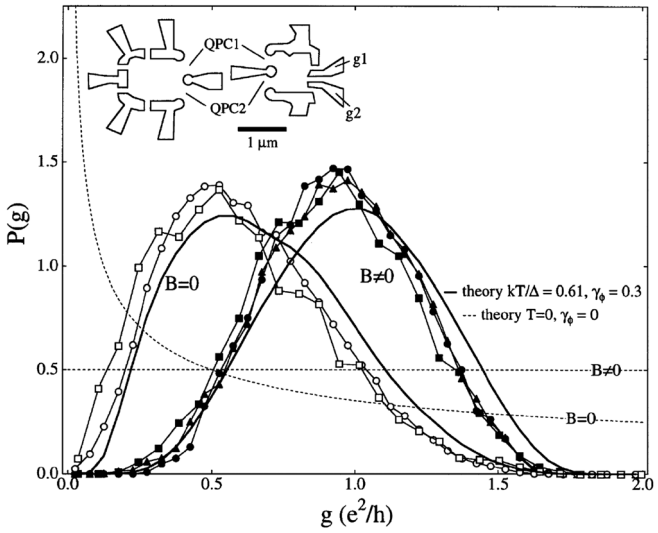

FIG. 5. Experimental results on the distribution of the conductance $P(g)$ in electrostatically defined quantum dots (see schematic on the top). Both the input and the output point contacts feature only a single open transverse mode such that these distributions are equivalent to the distribution of transmission eigenvalues in the single-channel limit. The corresponding theoretical predictions from RMT (dashed lines) do not reproduce the experimental data (connected symbols). Only when effects due to finite temperature (T) and dephasing (through the dephasing rate γ_ϕ) are taken into account (see solid lines) is good agreement found. The situation both with and without time-reversal symmetry are considered with the latter case being realized through the application of a finite magnetic field (B) applied perpendicular to the scattering area. From Huibers *et al.*, 1998.

comparatively small fraction of transmission eigenchannels features transmission in the classically forbidden region around $\tau \approx 0.5$. This analogy between the scattering of waves and particles is all the more remarkable as the open and closed transmission eigenchannels in the RMT distribution are an interference effect, in contrast to the classical case where evidently no interference occurs.

When comparing the predictions of RMT with the results of a real experiment or a simulation for a specific scattering geometry it is important to keep in mind that such a comparison can only be meaningful on a statistical level. This is because RMT does not contain any information about nonuniversal, i.e., system-specific details. Also, it is important to ask which requirements a system needs to fulfill such that its statistical properties can meaningfully be compared with RMT. For the case considered previously, where the scattering matrix was replaced by a random unitary matrix with the same number of channels on the left and right, we can think of a scattering system that is connected to an incoming and an outgoing port of equal size. Following the BGS conjecture, the scattering region in between the ports should be classically chaotic. In addition, the nonuniversal scattering contributions should be as weak as possible which is equivalent to the requirement that all incoming channels should get more or less equally randomized before exiting again from the scattering region.

Figure 4 shows a few scattering setups (for electrons) that fulfill these requirements to a satisfactory degree. The special shape of these systems already suggests that typical scatterers from the real world are, however, generally not described by RMT (the world would, indeed, be a dull place if this were the case). We also show in Fig. 5 that mesoscopic transport experiments usually suffer from several imperfections (decoherence processes, finite temperature, etc.) which severely spoil the agreement between the measurement data and an RMT prediction (even for well-engineered electron billiards as shown in Fig. 4). Figure 5 also shows that a decent agreement can be found when the influence of these real world effects is taken into account in the corresponding RMT model. As it turns out, the optical scattering through a disordered medium (as discussed later) is not well described by such simple models. The amendments to RMT that are necessary in these cases are, however, different from the ones employed for electron transport through quantum dots as in Fig. 5.

6. Dorokhov-Mello-Pereira-Kumar (DMPK) equation

The starting point for this section is the insight that a disordered system is inherently more complex than a chaotic quantum dot and its RMT description. This is because a disordered medium does more than just randomize all incoming waves in equal measure and let them escape again symmetrically on either side. In particular, depending on how long the incoming waves remain inside the medium, the degree of disorder scattering that they will suffer from will be very different. Also transmission and reflection will of course depend on the thickness of this medium as compared to the transport mean free path $\ell^\star$. To cope with this situation the simple RMT models from Sec. II.A.5 were extended by concatenating many random scattering matrices from the appropriate RMT ensemble in series. This approach was first used by Iida, Weidenmüller, and Zuk (1990a, 1990b), Weidenmüller (1990), and Altland (1991) to describe electronic scattering through a disordered wire and corresponds to

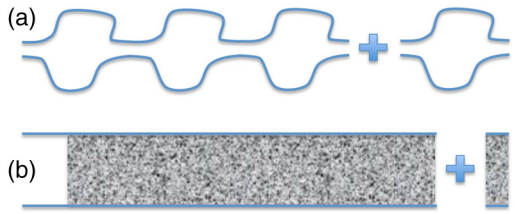

FIG. 6. (a) Stacking chaotic quantum dots behind each other leads to an effective wire geometry with statistics that can be well described by a corresponding random matrix approach. (b) In the more refined DMPK approach weakly scattering segments are recursively added to the wire geometry.

the description of a system consisting of a series of chaotic cavities; see Fig. 6(a). Whereas this ansatz allows one to conveniently extend RMT to more complicated scenarios, the approach also has several limitations, in particular, as the different transport regimes in a wire (ballistic, diffusive, localized) and their respective crossovers are hard to treat with it [see Dembowski *et al.* (1999) for a microwave experiment on coupled cavities].

To properly describe all of these regimes Dorokhov, Mello, Pereira, and Kumar had already proposed a model (Dorokhov, 1982; Mello, Pereyra, and Kumar, 1988) which subdivides the scattering region into a series of weakly scattering segments rather than using the fully randomized matrices from RMT; see Fig. 6(b). Choosing each segment of length Δz shorter than the transport mean free path $\Delta z \ll \ell^\star$, but longer than the wavelength $\Delta z \gg \lambda$ has the advantage that adding a new segment can be described as a perturbative correction. Assuming, in addition, that in each segment all incoming channels are scattered by the disorder into all of the available channels isotropically (i.e., with equal weight), one can derive a Fokker-Planck equation for the "Brownian motion" of the transmission eigenvalues τ_n (with constant diffusion coefficient). The corresponding evolution equation for the distribution of transmission eigenvalues τ_n as a function of the wire length L is known as the DMPK equation,

$$\frac{\partial}{\partial s}P(\{x_n\},s)=\frac{1}{2\gamma}\sum_{m=1}^{N}\frac{\partial}{\partial x_m}\left[\frac{\partial P}{\partial x_m}+\beta P\frac{\partial}{\partial x_m}\Omega(\{x_n\})\right], \tag{36}$$

where we substituted the transmission eigenvalues τ_n by new variables x_n according to $\tau_n = 1/\cosh^2 x_n$ and used $s = L/\ell^\star$, $\gamma = \beta N + 2 - \beta$ as well as

$$\Omega(\{x_n\}) = -\sum_{m<n}\ln|\sinh^2 x_n - \sinh^2 x_m| - \frac{1}{\beta}\sum_m \ln|\sinh 2x_m|. \tag{37}$$

The variables x used for simplifying the equations can be interpreted such that L/x_m is the channel-specific "localization length" for the transmission channel m in the disordered region (we see later what localization is).

Note that in real disordered wires the isotropy assumption, which corresponds to an ergodicity assumption in the transverse direction, is in general not well fulfilled for short lengths L. This is because any specific disorder profile typically features a nonuniform differential scattering cross section that leads to preferential coupling between specific mode pairs. Since the length scale for transverse diffusion is not taken into account in the DMPK equation, its validity is restricted to "quasi-one-dimensional" (quasi-1D) wire geometries which are much longer than their transverse width $L \gg W$. For very long systems (with $L \gg \ell^\star$) the solutions to the DMPK equation have equivalent statistics such as those of the concatenated random scattering matrix model. In a similar spirit, one can also set up an alternative model where not the scattering matrix but the Hamiltonian is the central quantity of interest. As demonstrated by Efetov and Larkin (1983) such an approach can be mapped onto a so-called supersymmetric nonlinear σ model, which was shown to be equivalent to the DMPK equation (Brouwer and Frahm, 1996) in the "thick wire limit" with many scattering channels N. Since all of these models were extensively discussed already in several reviews and books (Beenakker, 1997; Brouwer, 1997; Janssen, 2001), we will not review them again here. Rather, we present in the following a summary of the main results of the DMPK model that will be useful for later sections. For this purpose we rely on the exact solutions of the DMPK equation. As the case of broken time-reversal symmetry ($\beta = 2$) is much easier to treat, we discuss it first and then point out corrections for the case when time-reversal symmetry is restored ($\beta = 1$).

Focusing on the case of a thick wire with many transverse channels ($N \gg 1$) the DMPK equation makes specific predictions for three characteristic regimes as follows:

(i) In the *ballistic* regime the scattering is very weak, such that the system length is smaller than the mean free path $L \lesssim \ell$. In this limit the waves can be thought of as traveling ballistically on straight lines, rather than being multiply scattered by the disorder. Correspondingly, the transmission eigenvalues are all very close to 1 and no reflection occurs. In optics the ballistic regime is important since most imaging techniques work only in the ballistic limit. Correspondingly, in systems through which x rays propagate ballistically and visible light does not (a situation commonly encountered in biomedical imaging) the former type of radiation is better suited for imaging purposes.

(ii) In the *diffusive* regime, where the system length is in between the mean free path and the localization length $\ell^\star \lesssim L \lesssim \xi$ (with $\xi \approx \beta N \ell^\star$ in quasi-1D systems), the transmitted waves have already undergone many scattering events. This translates into a randomization of the transmission eigenvalues τ_n, which is quantified by solving the DMPK equation starting with a "ballistic initial condition" $\tau_n = 1$ for all n imposed at $s = L/\ell^\star = 0$ up to length L at which $s = L/\ell^\star \gg 1$. The solution for the joint probability density of transmission eigenvalues reads as follows (Beenakker and Rajaei, 1994):

$$P(\{x_n\},s) \propto \prod_{i<j}[(\sinh^2 x_j - \sinh^2 x_i)(x_j^2 - x_i^2)] \times \prod_i [\exp(-x_i^2 N/s)(x_i \sinh 2x_i)^{1/2}]. \tag{38}$$

Distilling out of this result the one-point probability density of transmission eigenvalues (by integration) one finds that in the regime of very long systems $s \gg 1$ the leading term of order $\mathcal{O}(N)$ (which is independent of β) features a uniform distribution of the transformed transmission eigenvalues x_n,

$$P(x,s) \equiv \langle \rho(x) \rangle_s = \frac{N}{s}\Theta(s-x). \tag{39}$$

Note that the only length dependence that remains here is the upper cutoff of this uniform distribution introduced by the Heaviside theta function Θ. This cutoff sets the transmission of all modes to zero for which $x \gtrsim L/\ell^\star$ and it keeps the normalization at $\int_0^\infty P(x,s)dx = N$. If we translate this result back to the transmission eigenvalues τ_n we find that out of the N transmission channels about $N\ell^\star/L$ have a finite transmission with $\tau > 4\exp(-2L/\ell^\star)$, which again follow a bimodal but asymmetric distribution [see Fig. 3(b)] (Dorokhov, 1984; Imry, 1986; Pendry, MacKinnon, and Roberts, 1992),

$$P(\tau) = \frac{N\ell^\star}{2L}\frac{1}{\tau\sqrt{1-\tau}}. \tag{40}$$

The remaining $N(1-\ell^\star/L)$ channels are closed (i.e., $\tau \approx 0$ for them). The normalization is such that $\int_{\tau_0}^1 P(\tau)d\tau = N$ with the lower integration limit $\tau_0 = 4\exp(-2L/\ell^\star)$. In practice the closed transmission eigenvalues are smeared over several eigenvalue spacings; since, however, they contribute only weakly to transport this cutoff is usually not specified in more detail. Most importantly, we thus obtained the result that even in transmission through a highly scattering quasi-1D system open transmission channels with $\tau \approx 1$ exist, which are chiefly responsible for the transmission (i.e., conductance). For the typical situation encountered in optics it is important to know that these open transmission channels are also present in the case of a disordered slab (see Sec. IV.A), which, contrary to the assumptions in the DMPK model, is much shorter than its transverse width $L \ll W$ (Goetschy and Stone, 2013).

The results obtained for $\beta = 2$ are subject to corrections of next to leading order $\mathcal{O}(1)$ for the time-reversal symmetric case of $\beta = 1$. These corrections were measured in the experiment (Mailly and Sanquer, 1992) and also appear in the average transmission and the variance of the fluctuations of the transmission as induced by changing the disorder configuration or an external parameter (like the scattering wave number k),

$$\begin{aligned}\langle T \rangle &= \frac{Nl}{L} + \frac{\beta-2}{3\beta} + \mathcal{O}(1/N),\\ \mathrm{var}T &= \frac{2}{15\beta} + \mathcal{O}(1/N).\end{aligned} \tag{41}$$

Note the interesting analogy of the leading order term in transmission $\propto 1/L$ to the Ohmic behavior of a classical wire whose resistance ($\propto 1/T$) scales linearly with the length L. Given the fact that we used a wave picture of transport rather than a classical trajectory picture (as in the Drude model), this analogy is far from obvious, in particular, in view of the bimodal distribution of transmission eigenvalues. Another interesting observation based on Eq. (41) is that the application of a mechanism that breaks time-reversal symmetry (like a magnetic field for electrons) leads to a slight increase of the average transmission (weak localization) and to a twofold decrease of the transmission fluctuations var$T$. The latter are apparently also universal in the case of diffusive scattering, with an N-independent value for the leading order term var$T = 2/(15\beta)$. Note that these results exactly agree with those from an independent calculation using a diagrammatic perturbation theory (Anderson, Abrahams, and Ramakrishnan, 1979; Gorkov, Larkin, and Khmelnitskii, 1979; Altshuler, 1985; Lee and Stone, 1985). Extensive reviews of the diagrammatic framework can be found in Dragoman and Dragoman (2004), Montambaux (2006), and Akkermans and Montambaux (2007). Diagrammatic techniques have the downside that they do not provide access to the full distribution of transmission eigenvalues, which is why we review them only briefly in Sec. III.B.

(iii) In the *localized* regime we are in the situation where the system length is larger than the so-called localization length $L \gtrsim \xi$, which in quasi-1D systems is connected to the mean free path $\ell^\star$ by $\xi \approx \beta N \ell^\star$. The effect of localization, originally proposed by Anderson (1958), exponentially suppresses transmission due to multiple interference and is thus entirely due to the wave nature of the scattered flux (the effect is nonexistent in a trajectory picture as for classical particles). As reviewed by Lagendijk, Tiggelen, and Wiersma (2009) and Abrahams (2010), several experiments have meanwhile successfully demonstrated localization of different kinds of waves (as for sound, microwaves, light, and cold atomic gases). Solving the DMPK equation in the localized limit ($s \gg N$) (Dorokhov, 1982, 983; Pichard, 1991) yields a joint probability density of the transmission eigenvalues which factorizes into a product of Gaussian distributions,

$$P(\{x_n\},s) = \left(\frac{\pi s}{N}\right)^{-N/2}\prod_{n=1}^{N}\exp\left[-(N/s)(x_n-\bar{x}_n)^2\right] \tag{42}$$

centered around the regularly spaced mean values $\bar{x}_n = (s/N)(2n-1)/2$. Since, in the limit $s \gg N$, the width of the Gaussians is much smaller than the spacing to the nearest neighbors, the transmission eigenvalues $1 \ll x_1 \ll x_2 \ll \cdots \ll x_N$ "crystallize" on a regular lattice with a lattice spacing of $\delta x = N/Ll$ (for $N \gg 1$) (Muttalib, 1990; Pichard *et al.*, 1990; Stone *et al.*, 1991; Frahm, 1995). It is interesting to compare this crystal-like behavior in the localized regime with the liquidlike behavior found for the diffusive regime, where x_n are uniformly distributed; see Eq. (39). In the transition region between these two regimes the distribution function is also intermediate between a constant function with a cutoff and a series of Gaussians as expected for a partially melted solid (see also experimental data in Fig. 13).

If we translate this result for x_n to the conventional transmission eigenvalues $\tau_n = 1/\cosh^2 x_n$, we can use the fact that $x_n \gg 1$ to simplify $\tau_n \approx 4\exp(-2x_n)$. The transmission eigenvalues thus have a log-normal distribution. Since for the total transmission T the first transmission eigenvalue τ_1

then dominates over all others, we also find that the total transmission $T \approx 4\exp(-2x_1)$ takes on a log-normal distribution with the following mean value and variance:

$$\langle T\rangle = -s/N + \mathcal{O}(1), \quad \mathrm{var}\langle T\rangle = -2\langle \ln T\rangle = 4L\xi. \quad (43)$$

These results were calculated for the case of broken time-reversal symmetry $\beta = 2$. The connection between the mean and the variance of the conductance, however, stays valid for other values of β (Pichard, 1991; Beenakker, 1994). Note how, based on this relationship, the variance of the transmission increases as the transmission itself is reduced, a result which contrasts the constant value of the transmission fluctuations in the diffusive case. To arrive at this result one uses the fact that the crystallization of transmission eigenvalues in the localized regime reduces the multichannel scattering problem effectively to a one-channel problem.

This single-channel regime of transport occurring in the deeply localized limit is also instructive for relating the transmission eigenchannels with the internal modes in the system—a connection that is already inherent in the definition of the scattering matrix, see discussion after Eq. (28). The internal "quasibound states" or "resonances" are responsible for mediating the transmission from one side of the medium to the other. In most circumstances, as in the diffusive scattering regime, these modes will have a resonance width $\delta\nu$ which exceeds their mean level spacing $\Delta\nu$, resulting in a ratio (called the Thouless number) (Edwards and Thouless, 1972; Thouless, 1977) $\delta \equiv \delta\nu/\Delta\nu > 1$ for which many modes are strongly overlapping such that they are extractable from the transmission data only through special techniques (Persson *et al.*, 2000; Kuhl *et al.*, 2008). The opposite limit of well-resolved modes and with it the regime of Anderson localization itself is characterized by $\delta < 1$ (Thouless criterion). Thouless (1977) and Abrahams *et al.* (1979) showed that in the localized limit the transmission T through the system [or, equivalently, the dimensionless conductance $g = Gh/(2e^2)$] and the Thouless number become the same $g = \delta$ (whereby the spectral and the transport properties become intimately connected). The Thouless number also turns out to govern all statistical properties of Anderson localization (Abrahams *et al.*, 1979).

As successfully demonstrated in an experimental microwave study, the good resolution of modes in the localized limit ($\delta < 1$) allows one to decompose a speckle pattern of radiation transmitted through a disordered sampled into a sum of only a few individual mode patterns (Wang and Genack, 2011). Not only do a very few localized modes dominate transmission in the localized regime, but also just a few transmission channels are open. As was demonstrated explicitly, these modes and channels are not merely strongly correlated (Choi, Park, and Choi, 2012), but, in fact, directly linked with each other (Peña *et al.*, 2014): In the deeply localized regime the single dominant transmission eigenchannel is given either by a single localized mode or by a so-called "necklace state," which is a highly transmitting superposition of overlapping localized modes (Pendry, 1987). Another curious observation in this deeply localized limit is that due to the dominance of a single transmission eigenchannel, the entire scattering system can be mapped onto a strictly one-dimensional system with the same statistical properties, provided that its localization length is properly renormalized (Peña *et al.*, 2014). Such a mapping can also be carried out for media with multiple open transmission channels that can then be mapped onto a sum of several one-dimensional systems, not only in terms of the transmission statistics, but also in terms of the density of states in the medium and the corresponding time delay (Davy, Shi, Park *et al.*, 2015; Davy, Shi, Wang *et al.*, 2015).

B. Open transmission eigenchannels and shot noise

One of the most spectacular predictions of RMT and of the DMPK equation is the existence of "open transmission eigenchannels" which were first discovered by Dorokhov (1984) (see the corresponding distribution of transmission eigenvalues in Fig. 3). Because of the absence of wave front shaping tools for coherent electron scattering, directly probing these channels with electrons is, however, possible only for simple geometries like quantum point contacts. As noted first by Imry (1986), the open transmission eigenchannels do, however, leave very conspicuous statistical signatures on the transport properties of electrons. In particular, as explained in the following, the presence of open transmission eigenchannels is detectable in the electronic shot noise (not to be confused with photonic shot noise or conductance fluctuations).

The term "shot noise" was originally introduced by Walter Schottky who was measuring the temporal fluctuations of the electric current in a vacuum tube (Schottky, 1918). As he first pointed out, these time-dependent fluctuations around the mean current value are due to the granularity of the electronic charge. In other words, since electrons come in discrete charge packets (i.e., the elementary charge) they do not produce a fluidlike flow of current but rather a random succession of discrete charge impact events. Comparing this situation to the (acoustic) noise produced by the small metal pellets from a "shot gun" when impinging on a solid surface, Schottky predicted shot noise to be a convenient tool to measure the value of the electron charge. Specifically, he proposed a relationship between the so-called shot-noise spectral density $S(\omega) = \langle \delta I(\omega)^2\rangle/\delta\omega$ based on the frequency-dependent current fluctuations around the mean current value $\delta I(\omega) = I(\omega) - \langle I(\omega)\rangle$ and the mean current $S(\omega) = 2e\langle I(\omega)\rangle$. (Note that the factor of 2 comes from the contribution of positive and negative frequencies and that the formula holds only in the limit where contributions from thermal or $1/f$ noise can be disregarded.) Since both $S(\omega)$ and $\langle I(\omega)\rangle$ can be measured in an experiment, one should be able to determine the elementary charge e according to Schottky, who assumed electrons to be completely uncorrelated (Poisson distributed) to derive this relation. Because of the residual correlations among electrons (even in a vacuum tube), Schottky's prediction, however, failed to reach the accuracy of the seminal Millikan experiment using oil droplets (Blanter and Büttiker, 2000; Beenakker and Schönenberger, 2003).

Contrary to the expectation from the famous Franck-Hertz experiment, the shot noise produced in Schottky's vacuum tube can be understood completely classically (Schönenberger *et al.*, 2001). In the mescoscopic limit, however, where electrons behave as quantum matter waves (as in ultrathin

wires at a few milli-Kelvin) the correlations that lead to deviations from the Schottky formula become dominant. These deviations are typically quantified in terms of the so-called "Fano factor" $F = S/S_P$, which is the ratio of the noise spectral density S for a given system (with correlations), as compared to the uncorrelated value of Schottky for Poissonian statistics $S_P = 2e\langle I\rangle$. In the mesoscopic limit these quantities can be conveniently evaluated using the Landauer-Büttiker framework (see Sec. II.A.4) to estimate both the current (Büttiker, 1988) $\langle I\rangle = (2e^2/h)V\sum_{n=1}^{N}\tau_n$ and the noise spectral density (Khlus, 1987; Lesovik, 1989; Büttiker, 1990)

$$S = 2e(2e^2/h)V\sum_{n=1}^{N}\tau_n(1-\tau_n). \tag{44}$$

Note that the latter prediction relates the magnitude of the time-dependent current fluctuations (S) with the time-independent transmission eigenvalues τ_n. An intuitive interpretation for this expression can be given as follows (Beenakker and Schönenberger, 2003): Since according to the Pauli principle, at zero temperature (as considered here) all levels up to the Fermi energy E_F are filled with electrons and above E_F all levels are empty, all thermal fluctuations are suppressed. The quantum shot noise thus comes from the electrons in a given transmission eigenchannel, attempting to transmit from source to drain with transmission probability τ_n. Since the electron in channel n can either pass or not pass, one gets binomial statistics as in a sequence of statistically independent yes or no experiments, each of which has a probability of τ_n to give "yes" as an answer. Correspondingly, the fluctuations in the transmitted current will be proportional to $\tau_n(1-\tau_n)$ for channel n; since, furthermore, all channels are statistically independent, the total fluctuations will be proportional to $\sum_{n=1}^{N}\tau_n(1-\tau_n)$, just as predicted in Eq. (44) for the noise spectral density. Note that in contrast to classical electronic shot noise which is due to the randomness associated with the emission of electrons, for quantum electronic shot noise the randomness in emission is completely suppressed by the Pauli principle. Instead, the noise here is due to the intrinsic indeterminism inherent in any quantum transmission problem to which only a transmission "probability" can be assigned. Because of the different statistics (Bose-Einstein versus Fermi-Dirac) the shot noise will also be different when replacing electrons with photons—even when considering systems with the same scattering matrix. Loosely speaking, photons are more "noisy" due to bunching, whereas electrons are more "quiet" due to antibunching. As a consequence, the results cannot be directly mapped from the electronic to the photonic case, where primarily amplification and absorption, rather than scattering, shift the Fano factor away from its Poissonian value (Beenakker and Patra, 1999). More recent work, however, has also found that mesoscopic fluctuations influence the photocount statistics of coherent light scattered in a random medium (Balog *et al.*, 2006).

To make contact with the open and closed transmission eigenchannels, consider that the noise spectral density S for electrons is a very sensitive measure of the distribution of transmission eigenvalues $P(\tau)$ studied in Secs. II.A.5 and II.A.6. To understand this point, consider that, for many scattering channels, $N \gg 1$, the expression for S can be conveniently rewritten as $S = 2e(2e^2/h)V\int_0^1 P(\tau)\tau(1-\tau)d\tau$, from which we conclude that the distribution function $P(\tau)$ enters the spectral density S through its first and second moments [i.e., $\int_0^1 P(\tau)\tau^n d\tau$ with $n = 1, 2$]. With the first moment just being the average transmission, the shot-noise power thus additionally provides access to the second moment of $P(\tau)$, a quantity which is strongly influenced by the presence of open and closed channels. In particular, if we replace $P(\tau)$ with the bimodal distributions obtained from RMT and from the DMPK equation, one finds specific values for the Fano factor.

Consider first the case where we assumed the scattering matrix to be distributed according to Dyson's circular ensemble with $P(\tau) = 1/\pi\sqrt{\tau(1-\tau)}$ [see Eq. (33)]. In this case the shot-noise Fano factor can be calculated by hand to take on the universal value $F = 1/4$ (Baranger and Mello, 1994; Jalabert, Pichard, and Beenakker, 1994), corresponding to a shot-noise spectral density S which is reduced to one-fourth of the Poissonian value S_P of Schottky (1918). When taking, instead, the transmission eigenvalue distribution which we found for the wire in the diffusive regime $P(\tau) \propto 1/\tau\sqrt{1-\tau}$ [see Eq. (40)] one finds the shot noise to be suppressed to one-third with a corresponding Fano factor of $F = 1/3$ (Beenakker and Büttiker, 1992; Nagaev, 1992), which is entirely independent of the mean free path $\ell^\star$ and of the system length L. In the transition from the diffusive to the ballistic limit (where all eigenchannels open up) the Fano factor vanishes, $F \to 0$ (de Jong and Beenakker, 1992), and in the transition to the localized limit (where all eigenchannels get closed) the Fano factor approaches 1, $F \to 1$ (Frahm, 1995). Note that in both of the nontrivial limits where the Fano factor takes on fractional values, low-temperature experiments with coherent electrons (Steinbach, Martinis, and Devoret, 1996; Oberholzer, Sukhorukov, and Schönenberger, 2002) have meanwhile confirmed the theoretical predictions (see Fig. 7), thereby providing a convincing proof for the existence of open transmission channels in transport through chaotic and disordered media, respectively. As we will see, going beyond this statistical evidence by accessing transmission

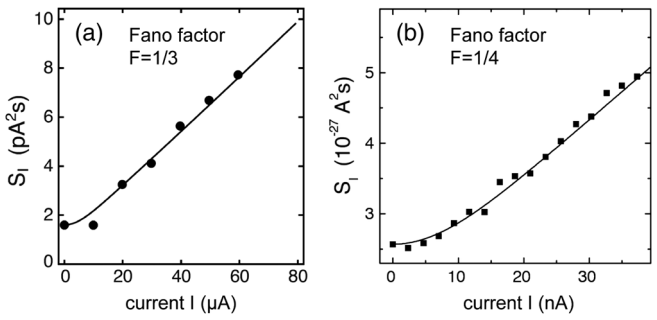

FIG. 7. Shot-noise power (a) in a metallic diffusive wire and (b) in a chaotic quantum cavity. The linear rise of the experimentally obtained noise power with increasing current has a slope that follows the theoretical predictions for the universal Fano factors $F = 1/3$ and $1/4$, respectively. For small currents the noise deviates from the linear increase due to finite temperature effects. Adapted from (a) Henny *et al.*, 1999, and (b) Oberholzer, Sukhorukov, and Schönenberger, 2002.

eigenchannels in optics directly will become possible only through the techniques of wave front shaping; see Sec. IV.

The universal values for the Fano factor rely on the assumption that waves entering in a scattering region get perfectly randomized before exiting this region. In fact, this assumption is the starting point for RMT and in weaker form, also enters the DMPK equation through the approximation of transverse isotropy. There are of course many ways in which a specific scattering system can fail to fulfill these assumptions: First, a scattering region might neither be fully chaotic nor disordered (Agam, Aleiner, and Larkin, 2000; Oberholzer, Sukhorukov, and Schönenberger, 2002; Aigner, Rotter, and Burgdörfer, 2005), or its disorder might feature spatial correlations which lead to very specific transmission statistics (Izrailev and Makarov, 2005). Also any effects like absorption (Brouwer, 1998; Méndez-Sánchez *et al.*, 2003) and dephasing (Baranger and Mello, 1995; Brouwer and Beenakker, 1995; Huibers *et al.*, 1998) have a significant influence (see Fig. 5). Consider also that the way in which one couples to a disordered region (as by barriers or point contacts) can lead to the situation that part of the incoming flux is immediately backreflected, rather than being randomized. Such nonuniversal contributions to the transport statistics can, however, be suitably described with tools like the Poisson kernel (Brouwer, 1995). Alternatively, one might also be confronted with systems like thin disordered interfaces which, on the one hand, scatter incoming waves strongly but which are shorter than the wavelength, on the other hand, such that they fall outside of the predictions for ballistic, diffusive, or localized samples; see Schep and Bauer (1997) for a successful treatment of such cases.

A particularly interesting challenge to conventional theories arises for the case when the randomization in a given scattering system affects only a subpart of the scattered flux. This situation occurs when "direct" scattering processes are able to penetrate the random medium in a time that is below the time scale necessary for randomization to set in (Gopar and Mello, 1998; Agam, Aleiner, and Larkin, 2000). For conventional strongly scattering media the fraction of such "ballistic" scattering states decreases exponentially with the system size. In imaging, this strong suppression of "ballistic light" in turbid media is in fact one of the key challenges for techniques based on light in the visible part of the spectrum, which is scattered significantly, e.g., in biological tissue (Ntziachristos, 2010). Also in the field of quantum shot noise a whole body of work exists in which the influence of such nonuniversal contributions has been investigated in detail (Agam, Aleiner, and Larkin, 2000; Nazmitdinov *et al.*, 2002; Oberholzer, Sukhorukov, and Schönenberger, 2002; Silvestrov, Goorden, and Beenakker, 2003; Jacquod and Sukhorukov, 2004; Aigner, Rotter, and Burgdörfer, 2005; Schomerus and Jacquod, 2005; Sukhorukov and Bulashenko, 2005; Marconcini *et al.*, 2006; Rotter, Aigner, and Burgdörfer, 2007). Generally speaking, one finds that ballistic scattering contributions reduce the Fano factor below the universal values. This is because the fully closed or fully open transmission eigenchannels (with $\tau = 0, 1$) associated with ballistic scattering are "noiseless" in terms of their contribution to shot noise (Silvestrov, Goorden, and Beenakker, 2003). We see in the next section and in Sec. V.C.2 that such ballistic noiseless states in electronic quantum transport correspond to geometric optics states in light scattering, i.e., light rays to which the eikonal approximation applies and which have a well-defined time delay (Rotter, Ambichl, and Libisch, 2011).

C. Time delay

When speaking of dynamical aspects of scattering problems, well-defined time scales are required to provide an estimate for the duration of a scattering process. Whereas many different definitions of such time scales are available in the literature, the most rigorously defined and most commonly used ones are the *time delay* (also called delay time or group delay) and the dwell time, which quantities measure the duration of a scattering process and the time spent inside a designated region, respectively. As can be expected, these two time scales turn out to be quantitiatively similar for many practical purposes, but also the subtle differences between them provide instructive insights.

The foundations for work on time delay were laid by Eugene Wigner and his student Leonard Eisenbud who studied the single-channel scattering phase shifts in resonant quantum scattering (Eisenbud, 1948; Wigner, 1955b). Their fundamental insight was that the time delay $\tau_\phi(E)$ an incident wave accumulates during a resonant scattering event (in one specific channel) as compared to nonresonant free propagation can be estimated by taking the energy derivative of the scattering phase shift $\phi(E)$ (see Fig. 8). The corresponding Wigner (or Wigner-Eisenbud) phase delay time is then given as $\tau_\phi(E) = \hbar\partial\phi(E)/\partial E = \partial\phi(\omega)/\partial\omega$, where E is the scattering energy of a quantum particle and ω its angular frequency. Since the energy derivative at a sharp scattering resonance can be very large, the corresponding time delay will also, correspondingly, take on very large positive values at such resonant energy values. Note, however, that the value of the time delay can, in principle, also be negative as, e.g., for the case of scattering through a repulsive potential. In this case one talks of a "time advance," the value of which is limited by causality constraints.

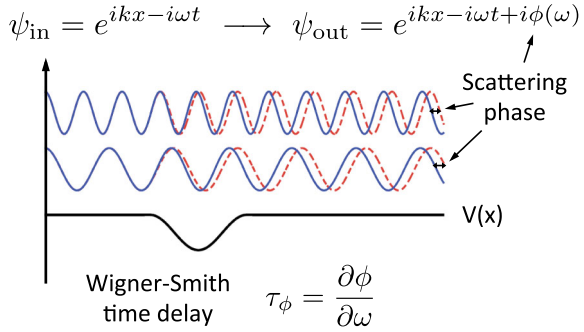

FIG. 8. The Wigner-Smith time delay is calculated as the derivative of the scattering phase accumulated due to the presence of a scattering potential, here given as $V(x)$. The solid (blue) and the dashed (red) lines schematically display the scattering wave function in the presence and absence of this potential, respectively (two different scattering energies are shown and reflections by the potential are ignored). From Pazourek, Nagele, and Burgdörfer, 2015.

Subsequent work (Jauch, Sinha, and Misra, 1972; Martin, 1976; Ilić *et al.*, 2009) showed that the definition of the time delay can be reformulated as follows:

$$\tau_\phi(E) = \frac{1}{\sigma_{\text{scat}} v} \int d^3 r [|\psi_E(\mathbf{r})|^2 - 1]. \tag{45}$$

This integral contains the single-channel scattering states $\psi_E(\mathbf{r})$ and extends over all of space. σ_{scat} is the scattering cross section and v is the velocity of the incident flux. Multiplied together, $\sigma_{\text{scat}} v$ is equal to the incident flux on the scatterer J_{in} (see Sec. II.A.2). Neglecting a self-interference term outside the scattering region Ξ [which usually averages out (Smith, 1960; Winful, 2003)], the time delay τ_ϕ thus measures an excess in the dwell time

$$\tau_d = \frac{1}{J_{\text{in}}} \int_\Xi d^3 r |\psi_E(\mathbf{r})|^2 \tag{46}$$

inside the scattering region Ξ as compared to propagation in free space. Both the scattering states $\psi_E(\mathbf{r})$ and the incoming flux associated with them are normalized here such that the integral $\int_\Xi d^3 r |\psi_E(\mathbf{r})|^2 = 1$ when the scattering region Ξ is replaced by free space (for which case the excess dwell time is zero).

To understand intuitively why Eq. (46) represents a dwell time, consider that the integral which appears there measures the intensity stored inside the scattering region Ξ. To obtain the time that this intensity stays inside the scattering region, one has to divide it by the outgoing flux J_{out}, which for a stationary scattering state like $\psi_E(\mathbf{r})$ is equal to the incoming flux J_{in} (the absence of gain and loss in the medium is assumed here). The identity in Eq. (46) thus corresponds to what one would expect from a simple classical picture. To emphasize this analogy we mention that the dwell time of water molecules in a bath tub can also be estimated equivalently based on the knowledge of the water volume contained in the tub and the incoming water flux (provided that the latter is equal to the outgoing flux).

These expressions were originally derived for the scattering of matter waves as described by the Schrödinger equation. Using the analogy with the Helmholtz equation (see Sec. II.A.1) these results can now be carried over to light scattering. Note, however, that in this case the electromagnetic energy density $u(\mathbf{r}, \omega)$ defined in Sec. II.A.2 enters the definition of the dwell time τ_d, which gives rise to additional terms related to a potential energy density stored in the dielectric medium. This contribution is particularly large when the dielectric constant of the medium is much larger than the vacuum value. Details on these terms as well as on their relation to the energy dependence of the optical potential V_{light} introduced in Sec. II.A.1 have been provided by Lagendijk and van Tiggelen (1996); see Sec. 3.2.3 there.

The reason why the concept of time delay has been so successful and widely used in a variety of different contexts is because it allows one to extract temporal information out of spectrally resolved scattering quantities like the scattering phase shift. A second major asset of the time-delay concept is its close relation to other physically relevant quantities of which the stored intensity inside a scattering region is just one. Another one is the absorption time τ_a, which measures the exponential decay of the light intensity in an absorbing medium (Lagendijk and van Tiggelen, 1996). Specifically, if we consider a light ray in a uniformly absorbing medium of constant refractive index $n = n_r + i n_i$ then the corresponding wave amplitude along the ray path can be written as $\psi_\omega(x, t) = A \exp(iknx - i\omega t)$, with A being an overall amplitude and x the spatial coordinate along the ray trajectory. The incoming wave intensity $|\psi_{\text{in}}|^2 = |A|^2$ will have decreased exponentially due to absorption $|\psi_{\text{out}}|^2 = |A|^2 \exp(-2 n_i k L)$ when leaving the medium. The trajectory length L inside the medium is now easily related to a corresponding time $\tau = L n_r / c$, which is now both the dwell time inside the medium (due to its relation with L) and the absorption time (due to its relation with the decreased intensity $|\psi_{\text{out}}|^2$). The simple physical reasoning behind this correspondence is that a wave suffers more from absorption the longer it stays inside an absorbing medium. In the limit of small absorption, where $n_i k L \ll 1$, this time can be estimated as follows (Lagendijk and van Tiggelen, 1996):

$$\tau = \lim_{n_i \to 0} \frac{n(1 - |\psi_{\text{out}}|^2 / |\psi_{\text{in}}|^2)}{2 n_i \omega}. \tag{47}$$

Note that in this relation the ratio of outgoing to incoming wave intensity emerges, which is known as the albedo of a scatterer $a = \langle |\psi_{\text{out}}|^2 \rangle / \langle |\psi_{\text{in}}|^2 \rangle$. For the visible part of the light spectrum the albedo (measured in reflection) ranges from values below 10% for very dark substances (like coal) to almost 90% for very bright substances (like snow). According to this simple derivation, such albedo measurements provide accurate information about the time light stays inside a given medium (Feshbach, 1962; Tiggelen, Tip, and Lagendijk, 1993). Note that for very inhomogeneously absorbing media the dwell time and the absorption time may also be quite different from each other as the absorption time then depends significantly on whether regions of high absorption are visited by a scattering wave or not.

In a seminal paper Smith (1960) showed that the time-delay concepts can be straightforwardly extended to multiple channels. In particular, for flux-conserving systems without loss or gain a corresponding multichannel time-delay matrix $\mathbf{Q}$ can be defined based on the unitary scattering matrix $\mathbf{S}$ in the following way:

$$\mathbf{Q} = -i\hbar \mathbf{S}^\dagger \frac{\partial \mathbf{S}}{\partial E}. \tag{48}$$

This Wigner-Smith (or Eisenbud-Wigner-Smith) time-delay matrix $\mathbf{Q}$ generalizes the concept of the "phase delay time" from above to multiple channels. However, care must be taken with respect to the definition of the asymptotic states that are related by the scattering matrix: Depending on whether the asymptotic states incorporate the free space propagation between the incoming and outgoing asymptotic regions, the Wigner-Smith matrix measures the times associated either with the phase delays or with the phases themselves. The matrix $\mathbf{Q}$ has the same number of $2N \times 2N$ complex elements

as the scattering matrix itself (see Sec. II.A.4) and it is Hermitian by construction. Its real eigenvalues q_n are referred to as the "proper delay times" which, when assuming an RMT distribution for the matrix elements of $\mathbf{S}$, can be shown to follow very specific distribution functions in the chaotic (Brouwer, Frahm, and Beenakker, 1997) and the diffusive limit (Ossipov, Kottos, and Geisel, 2003) [see also Méndez-Bermúdez and Kottos (2005) and Kottos (2005) for a review].

The Wigner-Smith time-delay matrix, in turn, shares a deep connection to the density of states (DOS) $\rho(\omega)$ of an open scattering system. Specifically, for a finite open medium the DOS can be defined as the sum over all quasibound states or resonances evaluated at the frequency ω (Breit and Wigner, 1936),

$$\rho(\omega) = \frac{1}{\pi}\sum_m \frac{\Gamma_m/2}{(\Gamma_m/2)^2 + (\omega-\omega_m)^2}, \tag{49}$$

where each of the Lorentzian mode profiles in this sum is spectrally normalized. Following the work of Gamow (1928) the resonance energies ω_m and their widths Γ_m are the real and imaginary parts of complex resonance eigenvalues at which the scattering matrix $\mathbf{S}(\omega)$ has its poles (see Sec. II.A.4). Based on this connection Krein, Birman, Lyuboshitz, and Schwinger (Schwinger, 1951; Krein, 1962; Lyuboshitz, 1977; Birman and Yafaev, 1992) showed that the DOS is directly expressible through the scattering matrix $\rho(\omega) = [-ic/(2\pi)]\mathrm{Tr}\mathbf{S}^\dagger\partial\mathbf{S}/\partial\omega$, and thus through the trace of the Wigner-Smith time-delay matrix $\rho(\omega) = [c/(2\pi)]\mathrm{Tr}\mathbf{Q}$, a connection which has meanwhile been verified also numerically (Yamilov and Cao, 2003) and experimentally (Davy, Shi, Wang *et al.*, 2015). From this relation we conclude that the DOS is directly proportional to the sum of the time delays associated with all the $2N$ channels described by the scattering matrix (Wigner, 1955b; Smith, 1960). Since, in addition, the local DOS $\rho(\mathbf{r},\omega)$ [where the DOS $\rho(\omega) = \int dr^3\rho(\mathbf{r},\omega)$] is also connected to the imaginary part of the Green's function $\rho(\omega,\mathbf{r}) = -2\omega\mathrm{Im}[G(\mathbf{r},\mathbf{r}',\omega)]/\pi$ [assuming a scalar field, see Wijnands *et al.* (1997), Chap. 4], these relations also uncover a direct connection between the time delay and the Green's function [see also the Krein-Friedel-Lloyd formula as discussed by Faulkner (1977)].

The close connection between the time delay and the DOS also has a very fundamental insight in store that can be obtained through a result derived by Hermann Weyl (Weyl, 1911; Arendt and Schleich, 2009). This so-called "Weyl law" states that the average DOS in a finite domain asymptotically (for increasing eigenfrequencies) follows a universal function (in frequency) that just depends on the volume and the surface area of the system, but not on the specific geometric details of the scattering potential. Through the equivalence between the DOS and the time delay, the latter is thus also determined by the volume and the surface of the scattering domain—a universal result that holds independently of whether the underlying medium leads to ballistic, diffusive scattering or even Anderson localization (Pierrat *et al.*, 2014). One interesting consequence of this result is that, through the connection between the time delay and the dwell time [see Eqs. (45) and (46)], this "universal" time delay can also be directly linked to the energy stored in the medium for unit incident flux in each of the scattering channels.

To explicitly show this we, however, first need to generalize the definition of the dwell time in Eq. (46) from a single to multiple scattering channels—in a way similar to what was done earlier for the time delay. For the corresponding definition of a "dwell-time operator" to be meaningful, we demand that the expectation value of this operator, for a given multichannel incoming state, yields the corresponding dwell time τ_d of this state. Since, according to Eq. (46), the dwell time involves the integral of the corresponding scattering state over the scattering volume, the definition of the dwell-time operator needs to incorporate the knowledge on the scattering states. Following Sec. II.A.3 we know that any scattering state can be connected to its incoming waves by way of the Green's function $\mathbf{G}$, with the result that the dwell-time operator $\mathbf{Q}_d$ is given as follows (Sokolov and Zelevinsky, 1997; Ambichl, 2012):

$$\mathbf{Q}_d = \hbar^2\mathbf{W}^\dagger(\mathbf{G})^\dagger\mathbf{G}\mathbf{W}, \tag{50}$$

where $\mathbf{W}$ is the energy-dependent coupling matrix from the scattering to the exterior region introduced in Eq. (28). We emphasize here that the expression for $\mathbf{Q}_d$ involves knowledge of the Green's functions on all points inside the scattering medium such that an evaluation of $\mathbf{Q}_d$ based on Eq. (50) is very complex (i.e., numerically costly and experimentally close to impossible). Alternatively, one can connect this dwell-time matrix with the definition of the Wigner-Smith time-delay matrix (which involves only the knowledge of the scattering matrix): When restricting the action of the energy (frequency) derivative of the scattering matrix in Eq. (48) to only the explicit energy dependence in Eq. (28) and neglecting the energy dependence of the coupling matrix $\mathbf{W}$, the time-delay and the dwell-time operators for unitary scattering systems are the same (Sokolov and Zelevinsky, 1997). In this sense, the time delay and the dwell time differ only by the "self-interference" term which involves also the evanescent modes in the near field of the scatterer (Ambichl, 2012).

In a similar way, the connection between the dwell time τ_d and the absorption time τ_a for the single-channel case suggests that such a relation might also exist on the more formal operator level. Following this idea, Savin and Sommers (2003) showed that for any uniformly absorbing medium [$n_i(\mathbf{r})$ is uniform in space] with arbitrary spatial complexity [$n_r(\mathbf{r})$ varying in space] the following relation holds between the scattering matrix $\mathbf{S}$ and the dwell-time operator $\mathbf{Q}_d$:

$$\mathbf{1} - \mathbf{S}^\dagger\mathbf{S} = \Gamma_a\mathbf{Q}_d, \tag{51}$$

where the parameter Γ_a is a phenomenological absorption rate and both $\mathbf{S}$ and $\mathbf{Q}_d$ are evaluated in the presence of absorption. Equation (51) suggests that in a uniformly absorbing medium the time-delay operator is nothing else than the operator which measures the unitarity deficit or the "subunitarity" of the scattering matrix. Since, in addition, the scattering matrix connects the incoming with the outgoing states in a scattering problem, which, in turn are related to each other through the albedo a, Eq. (51) is in fact nothing else than the multichannel generalization of Eq. (47).

As the last point in this section, we mention that the concepts on time delay may also be used to work out appropriately defined velocities. This is particularly relevant for the case of resonant wave scattering in a disordered medium, for which the conventionally used group and phase velocities fail to satisfy the causality relations required from special relativity (Lagendijk and van Tiggelen, 1996). A viable alternative here is the transport or energy velocity v_E, which determines the speed of energy transport (Brillouin, 1960) and is thus strictly causal also near the resonances of scatterers in the medium. Characteristic differences between v_E for light and electrons were discussed by Lagendijk and van Tiggelen (1996).

III. MESOSCOPIC EFFECTS IN OPTICAL SYSTEMS: THEORETICAL AND EXPERIMENTAL ANALOGIES

The theoretical framework presented in Sec. II has been and continues to be applied to a whole host of different questions arising in the context of mesoscopic scattering. Many experiments, in particular, for coherent electronic transport through mesoscopic conductors, such as quantum point contacts, "quantum billiards," nanowires, etc., have meanwhile been carried out in which many of the predictions could be studied in detail. Our emphasis here is on predictions from mesoscopic scattering theory, which could be realized both in *electronic transport* and in *optical* experiments that are here compared with each other. We review the first generation of such experiments, where also in the optical context "mesoscopic physics" effects have been revealed without resorting to wave front shaping techniques. Note that when we mention mesoscopic effects in optics, we do not refer to the signatures of the quantum (optical) nature of the electromagnetic field; rather, we refer here to signatures of light scattering that are intrinsically related to the finite mode number of a medium as well as to correlations between these modes.

A. Conductance quantization

One of the foundational experiments in mesoscopic transport was the demonstration of conductance quantization. By varying the opening width of a so-called quantum point contact (through electronic gates on top of a heterojunction) the conductance was observed to change in quantized steps of height $2e^2/h$; see Fig. 9(a) (van Wees *et al.*, 1988; Houten and Beenakker, 1996). The origin of this effect is the quantization of the transverse momentum in the quantum point contact; in other words, the electrons get transmitted through individual transverse modes, which are labeled with a discrete quantum number m or n (see Sec. II.A.4 where we introduced this concept already). Since each of these modes has a specific threshold that depends on the width of the quantum point contact, the conductance increases in a stepwise fashion whenever such a threshold is crossed. The experiment by van Wees *et al.* was thus crucial to lend credibility to the Landauer formula [see Eq. (16)] that describes the conductance G as a problem of coherent transmission T through multiple modes. As this description is, however, solely due to the wave nature of electrons, one should observe it also with other types of waves, including electromagnetic radiation. This idea was picked up by Montie *et al.* (1991), where a corresponding experiment was realized with light waves that were sent through a slit of tunable width; see Fig. 9(b). To mimic the way in which electrons impinge on the quantum point contact, the optical experiment featured a diffuse light source to distribute the incoming flux equally over all available transverse modes. With this type of illumination the light intensity transmitted through the slit was observed to follow the same steplike pattern as the electrons do in the mesoscopic analog; see Fig. 9(b).

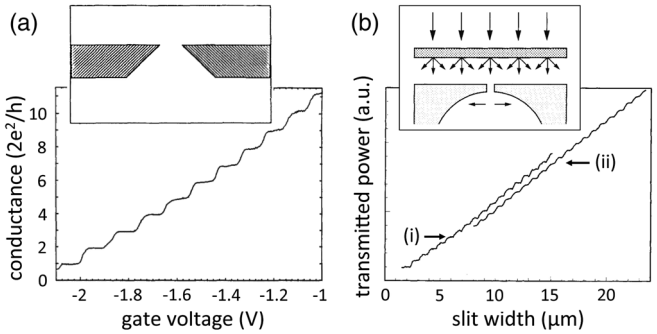

FIG. 9. (a) Conductance quantization in coherent electron transport through a quantum point contact (see upper inset and similar point contacts at the openings of the quantum billiards in Fig. 4). The conductance shows steps at integer values of the conductance quantum $2e^2/h$. Adapted from van Wees *et al.*, 1988. (b) Power of light transmitted through a slit with variable width (see upper inset). Similar steps as in (a) occur here when the slit width corresponds to integer multiples of $\lambda/2$ with λ the light wavelength. Before propagating through the slit the light is sent through a diffuser realized (i) with a piece of paper and (ii) with an array of parallel glass fibers. Adapted from Montie *et al.*, 1991.

Surprisingly, this optical experiment, which is much easier to carry out than its preceding electronics counterpart, was performed only after the corresponding physics was first understood in a mesoscopic context. This point underlines the main message of this review and indicates that a strategy along these lines may have many more interesting insights and surprises in store. Note here, in particular, that in optics the transmission through and the reflection from a scattering object are typically accessible in a mode-resolved way, which is not the case for electrons. This is also the case when studying the scattering through an extended disordered region where both the incoming and outgoing modes are quantized. To probe the total optical transmission $T = \sum_m T_m = \sum_{mn} T_{nm}$ as inherent in electronic conductance, one can use a diffuser [as in Fig. 9(b)] to ensure a nearly isotropic spatial illumination that excites all modes equally. In contrast, an illumination through a collimated laser beam with a well-defined incoming angle would probe the transmission through a suitable defined incoming mode $T_m = \sum_n T_{nm}$. The information on the transmission $T_{nm} = |t_{nm}|^2$ through the outcoupling modes n is contained in the speckle pattern appearing behind the scattering region, which contains the spatially resolved transmission pattern.

B. Conductance fluctuations

Experiments that were crucial for uncovering the nontrivial correlations in these different types of coherent transmission amplitudes were those reporting on conductance fluctuations in small metallic wires and rings (Umbach *et al.*, 1984; Washburn *et al.*, 1985; Webb *et al.*, 1985). These fluctuations observed in low-temperature measurements as a function of an applied magnetic field [see Fig. 10(b)] were actually unexpected. Their origin was first believed to be finite size effects of the conductor; it was, however, soon revealed (Lee and Stone, 1985) that these fluctuations are due to the multiple disorder scattering and the corresponding multipath interference, which sensitively depends on the system parameters (such as the disorder configuration, the Fermi energy, the magnetic field, etc.). In this sense the conductance fluctuations are like a fingerprint of the medium, which is highly complex but fully reproducible when measuring the conductance again a second time. An intriguing aspect of these conductance fluctuations is that their variance has a universal value of the order of e^2/h (at zero temperature), which is independent of the degree of disorder (in the diffusive regime) and the sample size, hence the name "universal conductance fluctuations" (UCFs). As demonstrated in Secs. II.A.5 and II.A.6, this surprising result and the exact value of the universal fluctuations can be understood based on the spectral rigidity of the transmission eigenvalues. Alternatively, one can also obtain very instructive insight into this phenomenon based on so-called diagrammatic techniques (Lee and Stone, 1985; Feng *et al.*, 1988; Berkovits and Feng, 1994) [see also Dragoman and Dragoman (2004), Montambaux (2006), and Akkermans and Montambaux (2007) for reviews of these techniques].

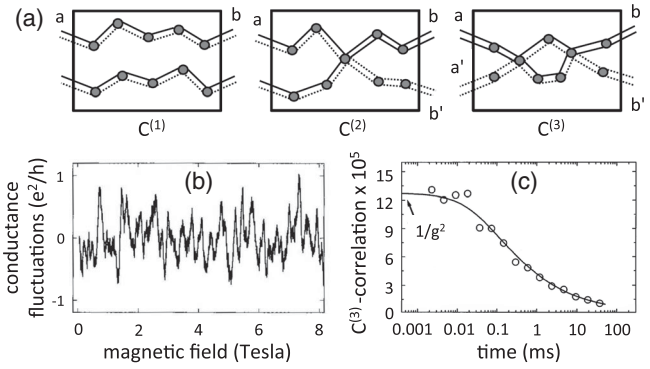

FIG. 10. (a) Schematic of the different scattering paths in a disordered medium and their correlations due to crossings. Nonintersecting paths ($C^{(1)}$) as in the left panel give rise to short-range speckle fluctuations. Those paths with a single crossing ($C^{(2)}$) as in the middle panel are already correlated with each other. The universal conductance are, however, induced by paths with two crossing ($C^{(3)}$) as in the right panel. Adapted from Scheffold and Maret, 1998. (b) Fluctuations of the electronic conductance G with respect to its mean value $\langle G\rangle$, measured in a 310 nm long and 25 nm wide gold wire at 10 mK as a function of a perpendicular magnetic field B. The variance of the conductance $\Delta G \approx 0.09e^2/h$ corresponds well to the theoretical prediction $(1/15)e^2/h$ given in Eq. (41). Adapted from Washburn and Webb, 1986. (c) Universal conductance fluctuations of light $C^{(3)}(t)$, measured dynamically in a turbid colloidal suspension. The experimental data are compared with a theoretical prediction using a dimensionless conductance of $g = 89$ and a sample thickness of $L = 13.1$ μm. Adapted from Scheffold and Maret, 1998.

Conceptually, the universal value of the electronic conductance fluctuations is a clear signature of the quantum coherence in the scattering process. We should thus expect to observe similar effects also with coherent disorder scattering of light. Since the optical speckle patterns contain sizable fluctuations as well, one may be tempted to think that UCFs are just a different aspect of speckle fluctuations. As it turns out, this is, however, not the case. To understand this in more detail consider the relation for the variance of the fluctuations, which for the transmission of light is given by $\sigma = \langle T^2\rangle - \langle T\rangle^2$. Writing $T = \sum_{mn} T_{mn}$ and $\delta T_{mn} = T_{mn} - \langle T_{mn}\rangle$, we obtain $\sigma = \sum_{mnm'n'} C_{mnm'n'}$, where $C_{mnm'n'} = \langle \delta T_{mn} \delta T_{m'n'}\rangle$. For evaluating this expression for coherent scattering processes, a classical diffusion equation is clearly insufficient; instead, one can employ a perturbative approach in the limit of weak but multiple scattering, where the perturbation parameter is $1/k\ell^\star \ll 1$ with $\ell^\star \ll L$ ($\ell^\star$ is the transport mean free path as discussed in Sec. II and L is the medium thickness). In the corresponding expansion (Feng *et al.*, 1988) the contributions to the correlation function $C_{mnm'n'} = C^{(1)}_{mnm'n'} + C^{(2)}_{mnm'n'} + C^{(3)}_{mnm'n'} + \cdots$ can be distinguished based on their different contributing scattering diagrams [see Fig. 10(a)] (only the first three terms in this expansion are considered in the following).

The first term $C^{(1)}_{mnm'n'}$ is always present (also in the absence of phase coherence) and of order zero in the expansion parameter $1/k\ell^\star \ll 1$. It corresponds to contributions from scattering paths that do not intersect while transmitting through the medium; see Fig. 10(a), left panel. In the absence of such intersections, correlations between modes are also largely absent (the only correlations remaining in rather thin media give rise to the so-called memory effect discussed in Secs. III.D and V.A). In $C^{(1)}_{mnm'n'}$ the most dominant contributions to the transmission arise when the difference between both the incoming and outgoing transverse momenta is zero $\Delta q_n = q_n - q_{n'} = \Delta q_m = q_m - q_{m'} = 0$. (Note that we implicitly used here the fact that our modes m, n have a well-defined transverse momentum q_n.) As a result one finds that the fluctuations in the speckle pattern are of the order of the average $\langle \delta T^2_{mn}\rangle = \langle T_{mn}\rangle^2$. This fact, also known as the Rayleigh law, is directly reflected in the granularity of a speckle pattern which features strong fluctuations between dark and bright spots. Why do these large fluctuations not translate to correspondingly large fluctuations of the total transmission and conductance? The answer is that the correlation term $C^{(1)}_{mnm'n'}$ has contributions only for specific mode combinations and thus, although being formally of the largest scale, their relative contribution to fluctuations diminishes with the number of modes considered. Overall, $C^{(1)}$ correlations yield only a subdominant contribution to the total transmission fluctuations.

This is where the additional correlation functions $C^{(2)}_{mnm'n'}$ and $C^{(3)}_{mnm'n'}$ come into play; see Fig. 10(a), middle and right

panels, respectively. In the diagrammatic expansion those two contributions come from scattering paths with one and two quantum crossings in the transmission process. Corresponding to the reduced likelihood for such crossings to occur, the scale of these contributions is reduced. In the sum for the total correlation, this reduction is, however, compensated by a less restrictive angular selection in terms of the differences Δq_n, Δq_m: Whereas the $C^{(1)}_{mnm'n'}$ term features only short-range correlations, the $C^{(2)}_{mnm'n'}$ and $C^{(3)}_{mnm'n'}$ terms feature long- and infinite-range correlations, respectively. It turns out, however, that not the long-range angular correlations inherent in $C^{(2)}_{mnm'n'}$, but only the infinite-range correlations in $C^{(3)}_{mnm'n'}$ yield the desired universal contribution to UCFs $\sigma = \sum_{mnm'n'} C_{mnm'n'} \approx \sum_{mnm'n'} C^{(3)}_{mnm'n'} \approx 1$.

Optical experiments can go much farther than simply remeasuring the universal value of UCFs found already earlier in mesoscopic transport. Scheffold and Maret (1998) recorded the time-dependent correlation functions $C^{(2)}(t)$ and $C^{(3)}(t)$ in transmission through a small pinhole filled with a turbid colloidal suspension. The temporal fluctuations of the transmitted light were due to the Brownian motion of scattering particles. By finding quantitative agreement with the theoretical predictions based on the diagrammatic terms, it thus became possible to not only establish UCFs in light scattering, but also to verify their microscopic origins; see also the corresponding experiments with microwaves (Shi and Genack, 2012a; Gehler *et al.*, 2016). As discussed by Berkovits and Feng (1994) the concepts on the correlation functions can be conveniently extended to also describe correlations in frequency as well as in the angle or in the spatial position of the emission from the disordered medium. Note also the possibility offered in optics to probe other quantities, such as the $C^{(0)}$ correlations (Shapiro, 1999; Cazé, Pierrat, and Carminati, 2010) that arise when the source is embedded inside the scattering medium, a setup that could be used for imaging purposes (Skipetrov and Maynard, 2000; Carminati *et al.*, 2015).

C. Weak localization

Another fundamental phenomenon for which the angular correlations play an important role and which also relies on specific quantum crossings of scattering paths is the so-called weak-localization effect (Abrahams *et al.*, 1979; Bergmann, 1983; Khmel'nitskii, 1984; Akkermans and Maynard, 1985; Wolf and Maret, 1985) [see Bergmann in Dragoman and Dragoman (2004), Montambaux (2006), Akkermans and Montambaux, (2007), and Abrahams (2010) for reviews]. The term "weak" refers to the overall weakness of this effect as compared to the "strong" (Anderson) localization for which weak localization is a precursor. Our starting point here is the observation from mesoscopic transport theory (see Secs. II.A.5 and II.A.6) that the transmission through a chaotic scattering system or a disordered wire is reduced by a small amount (again of the order of e^2/h) as compared to the value expected from a classical (i.e., incoherent) estimate. This suggests already that interference effects which are based on the coherence of the scattering process are at the heart of this phenomenon.

To properly capture this effect, we employ a similar diagrammatic picture as in the previous section in which the total transmission $T = |\sum_\alpha s_\alpha|^2$ can be written as a sum over all paths α with a corresponding complex amplitude s_α (the phase of which is given by the classical action). This expression not only contains the incoherent summation over all individual probabilities $\sum_\alpha |s_\alpha|^2$ for scattering paths to go from one side of the disordered medium to the other (as inherent in the classical Drude formula), but also features interference terms $\sum_{\alpha\neq\beta} s_\alpha s^*_\beta$ (corresponding to products of scattering amplitudes for different paths). One might argue that these interference terms average out to zero, since their random phases will lead to constructive and destructive interference with equal measure. Upon close inspection, this argument turns out to be incorrect, however; this is because certain path pairs have the same or very similar phase due to reciprocity (see Sec. II.A.4) and may thus lead to a certain bias away from the classical result, as seen in the following. Consider here, in particular, those paths that emanate from a source (outside of the medium) and return to it after scattering in the disordered medium [see Fig. 11(a)]. Since these loops can be traversed in two possible directions, we end up with two paths in the loop which have exactly the same phase as well as amplitude and thus always interfere constructively $|s_\alpha + s_\alpha|^2 = 4|s_\alpha|^2$, independently of the disorder configuration. Since this contribution of such time-reversed path pairs to the reflection is larger as compared to the classical result, where $|s_\alpha|^2 + |s_\alpha|^2 = 2|s_\alpha|^2$, they enhance the portion of the waves that are "coherently backscattered" to the source by a factor of 2 and thus increase the reflection R. In order to conserve the unitarity of the entire scattering process this increased reflection must be compensated by a corresponding decrease of the transmitted waves—in perfect correspondence with our earlier observation (see Secs. II.A.5 and II.A.6). The transmitted scattering paths that are responsible for this reduction can be shown to be self-crossing paths which feature loops in their scattering patterns which can be traversed in both a clockwise and a counterclockwise direction (Akkermans and Montambaux, 2007).

Although it turns out that the coherent backscattering contribution (resulting from time-reversed path pairs) explains the weak-localization effect only partially (Hastings, Stone, and Baranger, 1994), a controlled breaking of reciprocity will eventually destroy weak localization entirely and restore the classical (i.e., incoherent) transport result. For electronic scattering problems this can easily be done by applying an external magnetic field perpendicular to the scattering region. As shown in Fig. 11(b) the resistivity of an array of chaotic scatterers is, indeed, reduced when the magnetic field is applied (note that the reduction is independent on the sign of the field, due to the Onsager relations, see Sec. II.A.4).

For light waves, implementing a reciprocity-breaking mechanism is not so straightforward (adding absorption to the medium is not sufficient as it breaks only time-reversal symmetry, but not reciprocity). A viable alternative is provided here by the access to the spatial degrees of freedom of light. Specifically, to measure the weak localization of light its

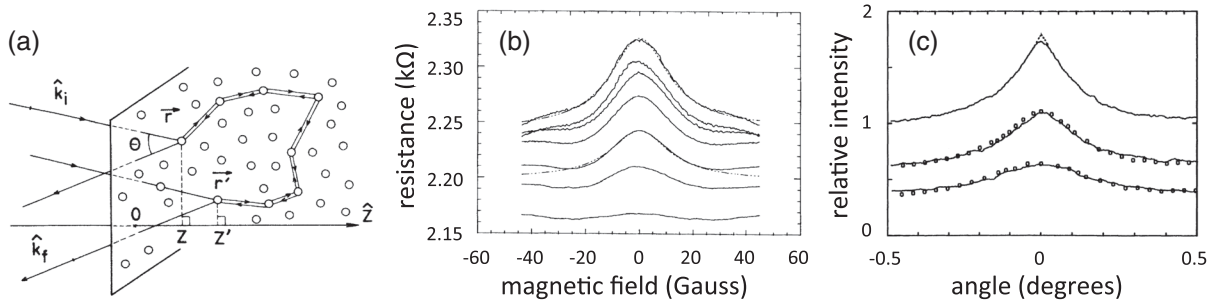

FIG. 11. (a) Electron or light paths associated with the weak-localization effect. Because of disorder scattering, the reflected wave vector $\hat{\mathbf{k}}_f$ is rotated by an angle θ with respect to the incoming wave vector $\hat{\mathbf{k}}_i$. From Akkermans, Wolf, and Maynard, 1986. (b) Resistance of an array of stadium-shaped quantum dots as a function of a perpendicular magnetic field. Different solid curves show experimental data at different temperatures (from top to bottom: $T = 50$ mK, $T = 200$ mK, $T = 400$ mK, $T = 800$ mK, $T = 1.6$ K, $T = 2.4$ K, and $T = 4.2$ K). The dash-dotted lines are Lorentzian fits. Adapted from Chang *et al.*, 1994. (c) Angular dependence of the light intensity backreflected from a disordered medium. Different curves show experimental results for samples with different degrees of absorption, as measured by the absorption mean free path ℓ_a. From top to bottom: $\ell_a = \infty$, $\ell_a = 810$ μm, and $\ell_a = 190$ μm. The intensity is normalized with respect to the value at 1°, measured in the nonabsorbing sample ($\ell_a = \infty$). The dots are predictions from diffusion theory. Adapted from Wolf *et al.*, 1988.

dependence on the angle of the light backscattered from the medium has been used as a key signature [see the angle θ in Fig. 11(a) and its influence on the backscattered intensity in Fig. 11(c)]. Since only those paths that return directly to the source find a partner with the same phase, the enhanced reflection is concentrated in a very narrow backreflection cone which is rather difficult to measure. Employing a Fraunhofer diffraction analysis, Akkermans, Wolf, and Maynard (1986) showed that the phase difference between two time-reversed reflected scattering paths is given as $(\mathbf{k}_i + \mathbf{k}_f)(\mathbf{r} - \mathbf{r}')$, where $\mathbf{k}_i$ and $\mathbf{k}_f$ are the initial and final wave numbers, respectively, that impinge on the disordered medium at the first scatterer position $\mathbf{r}$ and leave it again at the last encountered scatterer position $\mathbf{r}'$ [see Fig. 11(a)]. When the backscattering is perfect, $\mathbf{k}_i = -\mathbf{k}_f$, we obtain the enhancement by a factor of exactly 2 (as previously found). This number can be reduced slightly when recurrent scattering events occur in the strong scattering limit (Wiersma *et al.*, 1995). This maximum, however, degrades when the angle θ between $\mathbf{k}_i$ and $\mathbf{k}_f$ satisfies $|\theta - \pi| > \lambda/|\mathbf{r} - \mathbf{r}'|$, where λ is the wavelength. For the shortest possible loop involving just two scattering events, the typical value of $|\mathbf{r} - \mathbf{r}'|$ is given by the mean free path $\ell^\star$, resulting in a typical angular width of the backscattering cone $\theta \approx \lambda/\ell^\star$. Larger excursions of light paths in the medium with increased differences $|\mathbf{r} - \mathbf{r}'|$ are responsible for the peak of the cone, which was predicted to take on an approximately triangular shape (Akkermans, Wolf, and Maynard, 1986). In the presence of absorption this shape gets rounded as dissipative mechanisms affect primarily longer paths [see Fig. 11(c)].

Sophisticated optical experiments could meanwhile measure the details of this cone line shape, from which not only the value of $\ell^\star$ but essentially the entire path length distributions in the scattering medium can be extracted (Akkermans, Wolf, and Maynard, 1986) [compare also with similar studies for electronic scattering (Chang *et al.*, 1994)]. Note that in the optical regime the weak-localization effect also depends on the polarization of light as pointed out both theoretically (Akkermans, Wolf, and Maynard, 1986) and experimentally (Albada and Lagendijk, 1985; Dragoman and Dragoman, 2004). Recent experiments have even been able to go a step further in that they could actively suppress the coherent backscattering of light by exposing the medium to an ultrafast pump pulse (Muskens *et al.*, 2012), which opens up interesting opportunities for actively controlling mesoscopic interference phenomena.

D. Memory effect

In Sec. III.B on the universal conductance fluctuations we already analyzed the different correlations that exist between modes involved in the scattering process across a disordered medium. Using diagrammatic scattering techniques, it was discovered in the same context that the correlation function $C^{(1)}_{mnm'n'}$ points to the existence of correlations between incoming modes that have a similar transverse momentum, i.e., for which $\Delta q < 1/L$ (Feng *et al.*, 1988). The inverse proportionality with respect to the thickness of the medium L means that the angular range over which such correlations exist becomes smaller for increasing medium thickness—a result that is notably independent of the value of the transport mean free path $\ell^\star$, and on the exact realization of disorder. Quite interestingly, this so-called "memory effect" was discovered based on mesoscopic transport theory, although in mesoscopic electron transport an experimental study of this effect is not possible, since no angular resolution is available in electron scattering. It was realized very quickly, however, that the memory effect can be directly mapped to optical scattering setups where a laser beam with well-defined transverse momentum is sent onto a disordered medium (Freund, Rosenbluh, and Feng, 1988). We also see in Sec. V.A how this phenomenon has developed into a useful and practical effect with consequences for imaging through or inside a disordered medium (with and without wave front shaping).

Within the angular range discussed, a small angular rotation in the input beam then leads to a rotation of the output speckle pattern by the same angle (see Fig. 12), and correspondingly

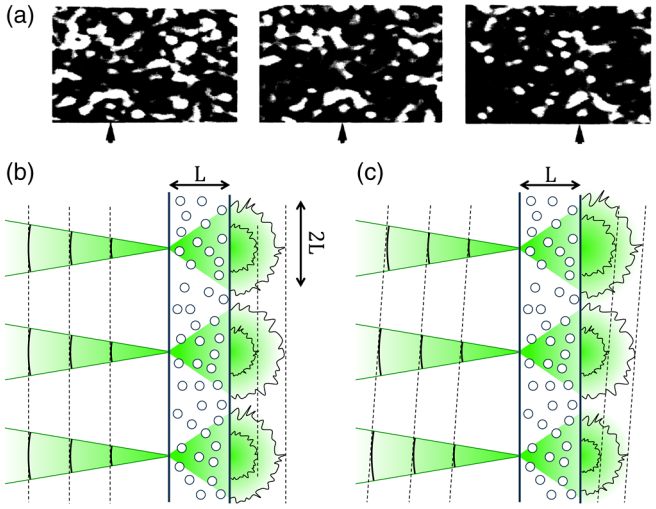

FIG. 12. (a) Speckle pattern as recorded behind a thin disordered medium for different incident angles (0, 10, and 20 mdeg from left to right). The arrows below the three panels point to a specific pattern (arc above a bright spot) that serves as a convenient visual reference for seeing the rightward move of the speckle pattern with increasing tilt of the input laser. Adapted from Freund, Rosenbluh, and Feng, 1988. (b), (c) Schematic illustrations to explain this memory effect: (b) A plane wave, represented here by three focal spots with the same phase, impinges on a disordered slab of thickness L and creates a speckle pattern in transmission. The distance of $2L$ between the input spots is the minimal one for which the output speckles do not yet significantly overlap. (c) When tilting the incoming laser a phase gradient is imposed on the incoming wave. Provided that the tilt is smaller than a critical angle $\theta \lesssim \lambda/(4L)$, this gradient is faithfully mapped onto the transmitted wave, resulting eventually in a shift of the speckle image recorded at a screen in the far field as in (a).

to a shift at a distance from the medium. For larger angles, the transmitted speckle pattern will rapidly become totally uncorrelated with the original (unshifted) speckle image. This behavior can be intuitively understood by considering that shifting the angle of incident light corresponds to a linear phase shift between the Huygens spots at which the incoming beam hits the disordered medium [see Fig. 12(b)]. In the diffusive regime, each of these spots will produce a cone of scattering pathways which reach the back side of the medium as a circular speckle halo, the diameter of which is about $2L$, where L is the medium thickness. To successfully transfer the phase ramp from the input beam onto these output speckle patterns, the speckle disks at the back side of the medium may not acquire a phase that is larger than about π from one disk to its nearest nonoverlapping neighbor [see Fig. 12(c)]. Using simple trigonometry, this condition, which is intuitively necessary to prevent phase mixing, can be translated to the requirement $\Delta q < 1/L$ found already earlier using diagrammatic techniques (Feng *et al.*, 1988). Practically, this restriction limits the thickness of the disordered optical medium to a few tens of micrometers in order to have a measurable effect. The first experiments (Freund, Rosenbluh, and Feng, 1988) on the optical memory effect were performed soon after the theoretical proposal (Feng *et al.*, 1988), in which the predicted shift of the speckle pattern could be unambiguously identified [see Fig. 12(a)].

When measuring correlations in reflection from a disordered medium $C_{mnm'n'} = \langle \delta R_{mn} \delta R_{m'n'} \rangle$ rather than in transmission, one ends up in the interesting situation that both the memory effect and the weak-localization corrections come into play. It turns out that, to first order, the angular width of the coherent backscattering cone and the memory effect angle are the same in reflection. This is because both effects rely on the diffuse spot size, i.e., the width of both peaks is now related to the mean free path $\Delta q < 1/\ell^\star$, which may be quite different from the memory effect angle in transmission that is related to the thickness of the disordered sample $\Delta q < 1/L$. The interplay between both effects was studied by Berkovits and Kaveh (1990), again through the different contributions $C^{(1)}_{mnm'n'}, C^{(2)}_{mnm'n'}, C^{(3)}_{mnm'n'}$. It turns out that due to reciprocity these correlation functions get additional peaks as compared to the corresponding expressions for transmission. Consider the first contribution without quantum crossings $C^{(1)}_{mnm'n'}$, which, in reflection, not only has a single peak at $\Delta q = 0$ (corresponding to $q_n = q_{n'}$ and $q_m = q_{m'}$), but also a second one at $\Delta q = q_n + q_m$ (corresponding to $q_m = -q_{n'}$ and $q_n = -q_{m'}$) which is due to the time-reversed contributions. Similar arguments can also be made for the next contribution $C^{(2)}_{mnm'n'}$ [see Berkovits and Kaveh, (1990) for details and Dragoman and Dragoman (2004) for a review]. Corrections to these results may be necessary due to internal surface reflections, as pointed out by Freund and Berkovits (1990). Recent acoustical measurements use the memory effect in reflection to obtain information on the path distribution in a random medium close to the transition to Anderson localization, finding a strong recurrence of scattering paths at the point where they enter the medium (Aubry *et al.*, 2014).

E. Distribution of transmission eigenvalues

As seen in the theoretical calculations presented in Sec. II, many interesting transport effects have their origin in the statistical distribution of the so-called "transmission eigenvalues" τ_n, which are the eigenvalues of the Hermitian matrix $\mathbf{t}^\dagger\mathbf{t}$ (or the squared singular values of $\mathbf{t}$ itself). In principle, the weak-localization correction to the conductance and the UCFs can be expressed through the distribution of the τ_n and their correlations, respectively. Mesoscopic experiments, however, went much further in also addressing the interesting consequences of the bimodal distribution of the transmission eigenvalues $P(\tau)$, which we derived earlier both for chaotic cavities [see Eq. (33)] and for diffusively scattering waveguides [see Eq. (40)]. Since the first moment of this distribution $\langle \tau \rangle = \int_0^1 d\tau P(\tau)\tau$ corresponding to the average transmission per incoming channel is basically unaffected by the bimodal shape of $P(\tau)$, measurements of the electronic conductance alone (which is just proportional to $\langle \tau \rangle$) do not reveal any signatures of the bimodality. This is different for other experimental observables, which depend on the higher moments of this distribution $\langle \tau^n \rangle = \int_0^1 d\tau P(\tau)\tau^n$ as, e.g., the quantum shot-noise power of electrons which probes the second moment $\langle \tau^2 \rangle$ in addition to the first (see Sec. II.B

for more details). The corresponding mesoscopic transport measurements with cavities and nanowires (Steinbach, Martinis, and Devoret, 1996) [see Blanter and Büttiker (2000) for a review] could not only observe the shot-noise suppression below the Poissonian value, corresponding to different predictions for the values of the Fano factor F (see Fig. 7); in fact, even the deviations from such universal behavior could be measured in detail (Oberholzer, Sukhorukov, and Schönenberger, 2002) and understood (Agam, Aleiner, and Larkin, 2000; Jacquod and Sukhorukov, 2004; Aigner, Rotter, and Burgdörfer, 2005; Sukhorukov and Bulashenko, 2005; Marconcini *et al.*, 2006; Rotter, Aigner, and Burgdörfer, 2007).

Whereas a fair amount of convincing evidence for the bimodal law has thus been put forward, no direct measurement of the transmission eigenvalues or of their distribution could be achieved in the mesoscopic context. For electromagnetic waves such measurements are also challenging, as the knowledge of the complete transmission matrix $\mathbf{t}$ is required to have access to its eigenvalues and eigenvectors, which determine the corresponding transmission channels. In particular in optics, where the number of such channels is large (as being proportional to the sample cross section and to the inverse squared of the wavelength $N \propto A/\lambda^2$), measuring the entire transmission matrix of a disordered sample is currently still out of reach (S. M. Popoff *et al.*, 2010; Yu *et al.*, 2013). This condition is, however, much more relaxed for waves with a longer wavelength, as for microwaves or also for acoustic waves. First microwave measurements (Shi and Genack, 2012b) on the full transmission matrix through metallic tubes, filled with randomly placed and strongly scattering aluminum spheres, already confirmed many of the predictions discussed in the theory Sec. II: In the diffusive regime, theory predicts that the largest transmission eigenvalue τ_1 is close to unity and thus corresponds to an open channel. In the localized regime, in turn, this largest transmission eigenvalue dominates the total transmission $T = \sum_n \tau_n$, such that $\tau_1 \gg \tau_{n>1}$. The crossover between these two regimes involving a "crystallization of transmission eigenvalues" (see Sec. II.A.6) with an equidistant spacing between the "crystal sites" ($\ln \tau_n$) was, indeed, observed in a microwave experiment (see Fig. 13).

In spite of this good theory–experiment correspondence, the elusive bimodality of the transmission eigenvalue distribution could so far not be verified with microwaves. An alternative strategy was recently put forward based on the propagation of elastic Lamb waves in a two-dimensional macroscopic metal stripe into which holes were drilled to emulate disorder (Gérardin *et al.*, 2014). Although the scattering matrix recorded here with laser interferometry was also not fully unitary, the bimodality of $P(\tau)$ could be verified with this setup. An advantage of this experimental setup is that it not only allows one to measure all transmission and reflection amplitudes, but, in fact, also the scattering wave functions inside the disordered medium in analogy to similar scanning techniques used for electrons (Topinka *et al.*, 2001), microwaves (Höhmann *et al.*, 2010), and optical fields (Fallert *et al.*, 2009).

In Sec. V we discuss the optical experiments dedicated to unraveling or exploiting open and closed channels.

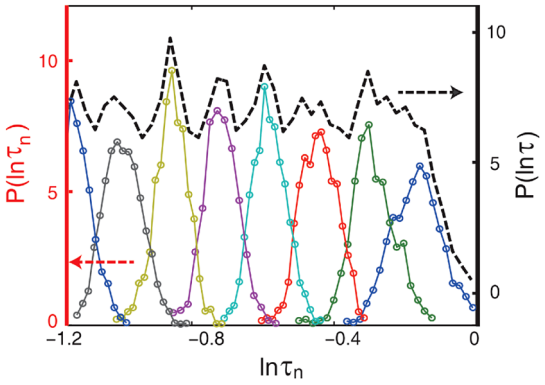

FIG. 13. Experimental results on the distribution of individual transmission eigenvalues τ_n (labeled with different colors) in microwave scattering through a strongly disordered quasi-1D geometry. As predicted theoretically, Anderson localization leads to a "crystallization" of transmission eigenvalues, corresponding to an equidistant spacing (on a logarithmic scale) between neighboring peaks of the corresponding distribution functions $P(\ln \tau_n)$. The top curve in black shows the distribution of the overall transmission $P(\ln \tau)$, where $\tau = \sum_n \tau_n$. From Shi and Genack, 2012b.

IV. OPTICAL WAVE FRONT SHAPING IN COMPLEX MEDIA

Progress in semiconductor and electronic engineering has led to the emergence of a now vast range of techniques and devices to actively manipulate light, in particular, spatial light modulators (SLMs). SLMs are mostly based either on liquid crystal technology (Lueder, 2010) or on microelectromechanical systems (MEMS) (Hornbeck, 2001; Gehner *et al.*, 2006; Gad-el Hak, 2010; Cornelissen, Bifano, and Bierden, 2012); see Fig. 14. They are nowadays offering control of up to a few million of spatial degrees of freedom (pixels) of light in phase or amplitude (van Putten, Vellekoop, and Mosk, 2008; Conkey, Caravaca-Aguirre, and Piestun, 2012; Goorden, Bertolotti, and Mosk, 2014) and are meanwhile widely used in imaging and microscopy (Maurer *et al.*, 2011). The advent of digital image sensors [mainly charge-coupled device (CCD) and complementary metal oxide semiconductor (CMOS)] also allows one to detect a correspondingly large number of degrees of freedom in intensity or in amplitude with the help of digital holography (Leith, Upatnieks, and Haines, 1965; Yamaguchi and Zhang, 1997; Cuche, Marquet, and Depeursinge, 2000). In the last 50 years, deformable mirror technology (Babcock, 1953) and adaptive optics concepts have revolutionized imaging through the atmosphere (Lee and Harp, 1969) and thereby also Earth-based astronomy (Roddier, 1999). In Secs. IV.A and IV.B, we show how these methods and concepts have been applied successfully to complex media. The starting point will be the paradigmatic case of the so-called "opaque lens" concept (Cartwright, 2007), which has a large range of applications, in particular, in imaging. We detail a few more specific systems of particular interest in Sec. IV.C.

A. The thin disordered slab: An opaque lens

In Sec. II, we treated the important case of a disordered wire and introduced in this context the concepts of ballistic wave

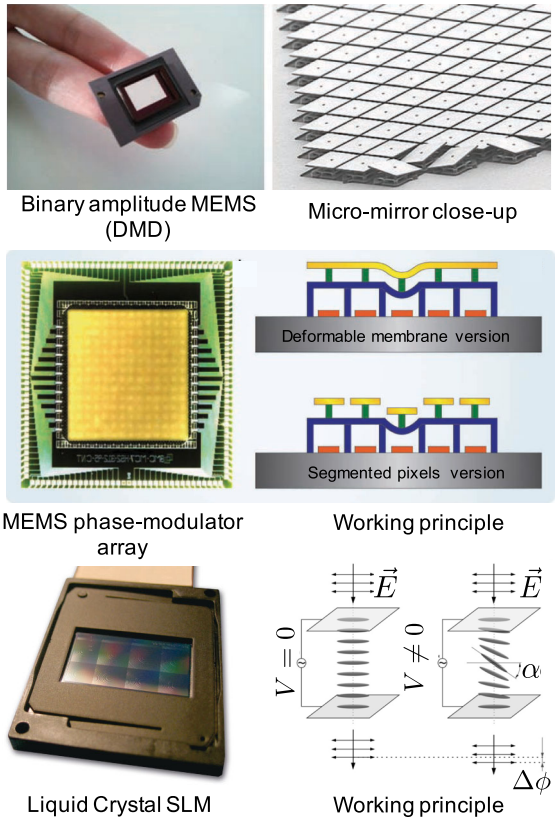

FIG. 14. Widely used types of digital spatial light modulators (SLMs). (Top) MEMS-based binary amplitude modulators from Texas Instruments. Adapted from Rabinovitz, 2011. (Middle) MEMS-based phase-only SLM, available with isolated pixels or a deformable membrane. Adapted from Bifano, 2011. (Bottom) Liquid crystal based phase-only SLM. Left: Courtesy of Holoeye Photonics AG. Right: Working principle in phase-only mode. Courtesy of Monika Ritsch-Marte.

scattering, transport mean free path, modes, the scattering matrix, etc. These concepts from the mesoscopic formalism will now be mapped to the optical domain. However, there is no exact optical equivalent of the disordered wire. In particular, the impenetrable and lossless boundaries of a wire cannot be easily reproduced in optics. Multimode optical fibers could be considered a strictly bounded complex system with a limited number of modes (and is described in Sec. IV.C.1), but they behave very differently from the disordered wire since there is no significant bulk disorder (scattering mostly comes from the boundaries), and almost no backscattering. Rather than a multimode fiber, the paradigmatic system in optics is the slab geometry: a disordered slab of finite thickness L and infinite lateral extension, with a transport mean free path $\ell^\star$ that is short enough to push the system into the multiple scattering regime $\ell^\star \ll L$. From now on we refer to this system as the opaque lens (Cartwright, 2007).

A common experimental realization of the opaque lens is typically a layer of dielectric scatterers of micrometer or submicrometer size, randomly packed, deposited on a transparent holder, such as a glass slide. To ensure sufficient scattering, the layer should be thick enough (a few micrometers to a few tens of micrometers), producing a white and opaque appearance, provided that the material is nonabsorptive (see

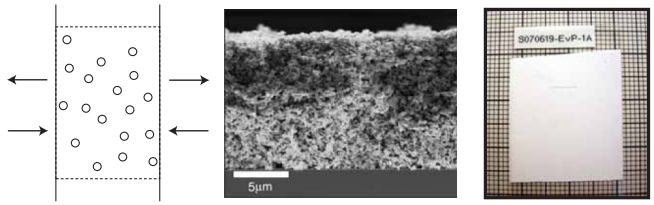

FIG. 15. The opaque lens in optics: a thin disordered slab of scattering material. (Left) Schematic model. Adapted from Yaqoob *et al.*, 2008. (Center) Scanning electron microscope (SEM) side view. (Right) Photograph of a ZnO opaque lens. Middle and right panels adapted from Vellekoop, 2008.

Fig. 15). This realization has the specific advantage of being easy to fabricate and extremely stable. Wave front shaping techniques are by nature relatively slow, making the stability of a particular realization of disorder an essential requirement. Of course, this simple system can be mapped to several practical situations and materials. Snow, biological tissues, white paper, egg shell, and bones are just a few examples of thin or thick materials that can be understood with the same formalism. An important difference between these systems and electronic mesoscopic systems is the very large number of modes supported: Since objects in optics are usually macroscopic, often in the millimeter scale or larger, the number of optical modes, which scales as A/λ^2 (with A the transverse area and λ the wavelength), can easily be in the 10^6 range or higher. Most of the results also extend to dynamical systems (such as milk, fog, clouds, etc.) although the geometry and the fast dynamics make them challenging for wave front shaping.

To describe an opaque lens more formally, we now consider a three-dimensional slab of finite thickness L that features complex inhomogeneities of the refractive index, such as to be fully disordered. Such a case is realized for a slab composed of a random packing of particles of high refractive index of different sizes, in a matrix of low refractive index (as, e.g., in air). These inhomogeneities scatter light in a very complex way, but as seen in Sec. II, this does not prevent us from describing such a system with the formalism of the scattering or transmission matrix, as long as the system is linear (see Fig. 15).

We consider the case when the light that is transmitted through the sample has been multiply scattered (i.e., $\ell^\star \ll L$) and absorption can be neglected (although absorption or gain do not necessarily break the linearity assumption). We also need to make sure that the scattering strength is not too strong ($k\ell^\star \gg 1$) to avoid effects related to strong localization. In essence, we suppose that light is subject to a purely diffusive process when going through the slab. While we described in Sec. III the fact that different mesoscopic effects can be present in such a situation, these effects are typically elusive. Especially in the case of only partial control and detection, we can often consider to first order that no mesoscopic correlations are present.

In this limit, we can assume that any coherent monochromatic wave front incident on one side of the slab will be multiply scattered such as to produce a fully developed speckle on the other side (Goodman, 1976). Two speckle patterns corresponding to two different illuminations will be

completely uncorrelated provided the inputs are sufficiently uncorrelated. Still, each speckle is the deterministic result of the multiple scattering process and is specific to the medium and to the chosen input wave front. Because of the high complexity of the multiple scattering propagation, it is in practice impossible to calculate *a priori* the speckle pattern. However, as discussed in Sec. III.B, speckle patterns have some well-defined statistical properties. While complete books are devoted to these phenomena (Goodman, 2007), we recall here only some fundamental aspects for polarized, monochromatic, and spatially coherent incident light: (i) Because of the multiple scattering process, the incident polarization is mixed during the propagation. After the medium, the light has a well-defined but unpredictable polarization state at any point: The vectorial field distribution is the sum of intensities of two uncorrelated fully developed speckles for two orthogonal polarization states (e.g., vertical and horizontal polarization). (ii) For a given polarization, the distribution of intensities follows the Rayleigh law (for each polarization). (iii) The characteristic grain size depends on the geometry of the system, corresponds to diffraction-limited spots, and is related to the spatial correlation $C^{(1)}$ (defined in Sec. III.B).

1. Transmission matrix in the spatial domain

In this section, we consider the transmission matrix of a disordered slab, i.e., of an opaque lens. This transmission matrix is labeled as $\tilde{\mathbf{t}}$ and links the fields of the N input to the M output pixels of the SLM and the detector, respectively.

We have seen in Eq. (14) that the transmission matrix $\mathbf{t}$ connects the incoming field modes from the left to the outgoing field modes on the right, written as $\mathbf{c}_r^+ = \mathbf{t}\mathbf{c}_l^+$. The difference between the experimentally measured $\tilde{\mathbf{t}}$ and the full transmission matrix $\mathbf{t}$ of the disordered medium is that $\tilde{\mathbf{t}}$ also comprises the propagation of the field from the SLM to the medium and from the medium to the detector. In addition $\tilde{\mathbf{t}}$ contains only a small part of the full transmission matrix $\mathbf{t}$, usually decomposed in pixels, which do not constitute a complete basis. Since additionally the pixels, in both modulation and detection, are typically illuminated at close to normal and constant incidence, we can usually neglect in practice the problem of flux normalization discussed in Sec. II.A.4. For simplicity, we note these outgoing (incoming) modes as $\tilde{\mathbf{E}}^{\text{out}}$ ($\tilde{\mathbf{E}}^{\text{in}}$), in which notation the field on the mth output pixel is $\tilde{E}_m^{\text{out}} = \sum_n \tilde{t}_{mn}\tilde{E}_n^{\text{in}}$, or equivalently $\tilde{\mathbf{E}}^{\text{out}} = \tilde{\mathbf{t}}\tilde{\mathbf{E}}^{\text{in}}$. We explain in Sec. IV.A.3 how to retrieve $\tilde{\mathbf{t}}$.

In the same way as the singular values σ_i of $\mathbf{t}$ and the corresponding transmission eigenvalues $\tau_i = \sigma_i^2$ give access to the physics of wave propagation through the disordered wire (see Sec. II), we now work with the singular values and singular vectors of the transmission matrix $\tilde{\mathbf{t}}$ for the opaque lens, first in the monochromatic picture, and then including the temporal and spectral aspects.

In the limit defined previously, where one has access only to a small number of well-separated modes of the open system, i.e., where each input mode n gives rise to an independent speckle uncorrelated with the others, the singular values of the transmission matrix $\tilde{\mathbf{t}}$ are expected to follow the so-called Marčenko-Pastur law (Marčenko and Pastur, 1967) that describes the singular value distribution (SVD) of rectangular random matrices without correlations. In essence, this law states that, for a $N \times M$ random matrix ($M \geq N$) of uncorrelated identically distributed elements, the distribution of singular values $\tilde{\sigma}$ (normalized to the average transmission) depends only on the ratio $\gamma = M/N \geq 1$ and converges to

$$P_\gamma(\tilde{\sigma}) \approx \frac{\gamma}{2\pi\tilde{\sigma}}\sqrt{(\tilde{\sigma}^2 - \tilde{\sigma}_{\min}^2)(\tilde{\sigma}^2 - \tilde{\sigma}_{\max}^2)} \quad \forall\ \tilde{\sigma} \in [\tilde{\sigma}_{\min}, \tilde{\sigma}_{\max}]$$
$$\approx 0 \quad \text{otherwise}, \tag{52}$$

where $\tilde{\sigma}_{\min} = 1 - \sqrt{\gamma^{-1}}$ and $\tilde{\sigma}_{\max} = 1 + \sqrt{\gamma^{-1}}$. Correspondingly, the normalized SVD is bounded in the domain $[1-\gamma^{-1}, 1+\gamma^{-1}]$. We supposed having more input than output channels, $M \geq N$, but the SVD remains the same if we reverse the role of N and M. The interesting case of the square matrix $N = M$ gives rise to a circular distribution of the singular values in the interval [0, 2] and is usually referred to as the "quarter-circle law." Still, for N, M finite, Eq. (52) is an approximation and the eigenvalue density outside the indicted interval is exponentially small, but not zero.

This result is routinely used in telecommunications to assess the bit rate and the error rate of data transmission (Chizhik *et al.*, 2003). The Marčenko-Pastur distribution was also measured experimentally through a multiply scattering medium in acoustics (Sprik *et al.*, 2008; Aubry and Derode, 2009). In Sec. IV.A.4, we show how the transmission matrix $\tilde{\mathbf{t}}$ can be measured and the same distribution can be experimentally recovered from it also in optics (Popoff, Lerosey *et al.*, 2011) (see Fig. 16). The question that immediately arises at this point is how this result relates to the bimodal

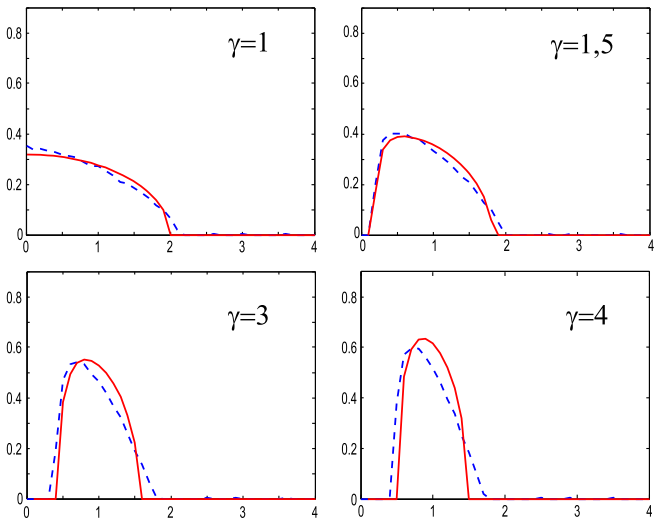

FIG. 16. Normalized distribution of singular values $\tilde{\sigma}$ of transmission matrices of opaque lenses as a function of the ratio γ between the number of output to input modes M/N. (Values of $\tilde{\sigma}$ are normalized to the average transmission and can thus be larger than 1.) Dashed blue lines: experimental data; red lines: independent identically distributed random matrices. The discrepancy can be attributed to residual correlations in the measured matrices. For the value $\gamma = 1$ one obtains the so-called "quarter-circle law." Adapted from Popoff, Lerosey *et al.*, 2011.

distribution of transmission eigenvalues derived in Sec. II. The crucial point to observe here is that in the experimental conditions we considered, we access only a small fraction of the modes. Under these conditions, the bimodal distribution reduces to the Marčenko-Pastur law when decreasing the number of input and output channels considered, whereby correlations get increasingly lost (Goetschy and Stone, 2013). To approach the regime where mesoscopic correlations start playing a role, particular care has to be taken to control and measure a large fraction of the modes, also for large solid angles (e.g., by using high numerical aperture optics), and for both polarizations. This particular topic is covered in Sec. V.B. For the time being, in most practical cases we can consider the disordered slab as a "perfect" mixer for light, obeying Marčenko-Pastur's law.

So far we have not discussed what happens in reflection from the disordered slab. In principle, the reflection matrix can also be defined in the same way as for transmission. However, reflected light comprises not only multiply scattered light, but also singly scattered components, as well as all components in between. The reflection will therefore not be as perfectly "mixed" as the transmission, in particular, in terms of the polarization of light that is conserved for single scattering and can be partially conserved for few scattering events (MacKintosh *et al.*, 1989). Weak-localization effects such as the coherent backscattering cone described in Sec. III are also present, although their signature has not been observed directly in the optical reflection matrix [see Aubry and Derode (2009) and Aubry *et al.* (2014) for realizations in acoustics]. Still, most of the results and experiments described later translate almost perfectly from transmission to reflection. We see in Sec. IV.C.2 how these deviations from perfect mixing can be retrieved and exploited for imaging.

2. Temporal and spectral aspects

In the temporal domain, light enters a disordered slab of thickness L, diffusely propagates in it, and exits on either side, or is absorbed. Knowing the diffusion parameters for light, such as the diffusivity $D = v_E \ell^\star/3$ (here $\ell^\star$ is the transport mean free path and v_E is the energy velocity defined in Sec. II.C), it is possible to recover the so-called Thouless time τ_D of the medium (Thouless, 1977). The parameter τ_D corresponds to the average time that a photon, already in the medium, takes to reach the medium boundaries and is related to the Thouless number defined in Sec. II.A.6. The time τ_D scales with $L^2/\pi^2 D$ and corresponds to a spectral bandwidth $\Delta\omega_D = 1/\tau_D$. While this time intrinsically describes the photon lifetime in the medium, it is not exactly the relevant quantity for transmission and reflection, where a photon first needs to enter the medium before exiting on either side. For the thin but multiply scattering slab geometry, where $\ell^\star \ll L$, the reflection time τ_R is typically much shorter than the transmission time and the Thouless time τ_D, since a photon typically explores only a small volume of depth $\ell^\star$ before exiting on the same side; as such, τ_R is of the order of $\ell^\star/v_E$. Meanwhile, the transmission time τ_T will be on average slightly longer than τ_D since the photon must first enter the medium before exiting (Landauer and Büttiker, 1987; Vellekoop, Lodahl, and Lagendijk, 2005), but the distribution

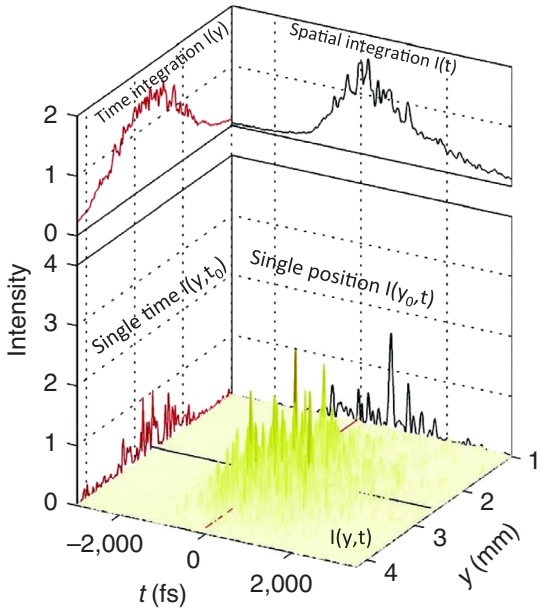

FIG. 17. Representation of a spatiotemporal speckle resulting from the propagation of a focused ultrashort pulse through a thin ZnO sample. The speckle is measured along one spatial dimension and as a function of time. One observes a complex spatiospectral structure $I(y,t)$ with speckle statistics that are apparent when looking at a temporal or a spatial section for a given time or position, i.e., $I(y_0,t)$ and $I(y,t_0)$. When looking at a projection (integration) along the temporal or spatial coordinate, i.e., $I(y)$ or $I(t)$, one retrieves, respectively, the diffuse halo, and the average temporal broadening of the pulse. Adapted from McCabe *et al.*, 2011.

of transmission times will have an exponential tail of exponent $-t/\tau_D$. A rigorous way to define and assess these scattering times is through the concepts of time delay and dwell time, discussed in Sec. II.C. For practical purposes it is often convenient to use Monte Carlo simulations (Patterson, Chance, and Wilson, 1989) or to measure the times experimentally (Vellekoop, Lodahl, and Lagendijk, 2005; Curry *et al.*, 2011; McCabe *et al.*, 2011) (see Fig. 17 for a spatiotemporal speckle and its spatial and temporal averages). To these transmission and reflection times spectral bandwidths $\Delta\omega_T$ and $\Delta\omega_R$ are associated, which will in turn correspond to a spectral correlation of the respective transmission and reflection matrices of the slab.

3. Accessing the monochromatic transmission matrix of an opaque lens

The monochromatic transmission matrix of a complex medium can indeed be measured (S. M. Popoff *et al.*, 2010). In essence, it is possible to send a set of input spatial modes, to record for each of these modes the transmitted amplitude, and to determine directly from these input-output measurements the transmission matrix elements $\tilde{t}_{mn}$ linking the input mode pixels of the SLM to the output pixels on a CCD camera.

In an initial implementation (see Fig. 18), the input spatial modes were generated using a liquid crystal SLM, and the output amplitudes were obtained using phase-shifting

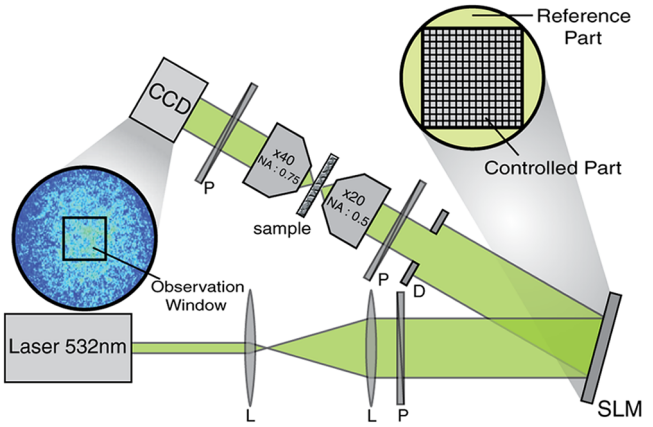

FIG. 18. Setup of the first measurement of the transmission matrix. The laser is expanded and reflected off an SLM. Part of the SLM is unmodulated and serves as a reference for the interferometric measurement of the output field. The phase-modulated beam is focused on the multiple scattering sample and the output intensity speckle pattern is imaged by a CCD camera. Additional elements: lens (L), polarizer (P), and diaphragm (D). Adapted from S. M. Popoff *et al.*, 2010.

holography (Yamaguchi and Zhang, 1997), i.e., by recording several images on the CCD, resulting from the interference of the output wave to be measured with a reference wave with different phase shifts. Later on, several variants were used to either modulate or detect the amplitude of the field and recover the transmission matrix. Y. Choi *et al.* (2011) illuminated the medium with a plane wave, with an angle of illumination that was varied using a galvanometer-mounted tilting mirror (Choi *et al.*, 2007). While this method allows one to directly measure every input angle, thanks to the movable mirrors, it does not permit one to directly generate a given arbitrary wave front. On the detection side, in order to record the amplitude hologram of the output speckle in a single image rather than in a sequence, off-axis holography was implemented (Kim *et al.*, 2012; Akbulut *et al.*, 2016). Using a set of polarization beam splitters and polarization optics, it is also possible to control or to detect both polarizations at the same time, thus accessing a polarization-resolved transmission matrix (Tripathi *et al.*, 2012). Finally, using phase-retrieval algorithms, it is even possible to infer the phase and amplitude of the field from intensity measurements, without the need of the reference (Drémeau *et al.*, 2015). Once the transmission matrix has been measured, one can use it to either study the medium by looking at the modes (see Fig. 16 and the discussion in Sec. V.B) or control the light transmitted through the medium, as seen in Sec. IV.B.

4. Accessing the temporally or spectrally resolved transmission matrix

In the monochromatic approach, one characterizes the behavior of the medium at a specific wavelength, at the expense of ignoring the richness of the spectral and temporal behavior of light in the medium. This additional information can, in turn, be extremely useful when trying to either control spectrally or temporally the transmitted light. It also provides additional insights into the modes of the medium.

Two approaches were introduced in order to explore this additional dimension. The first one is based on accessing a spectrally resolved transmission matrix, which amounts to measuring a monochromatic transmission matrix at many frequencies. In this way the spectral behavior of the medium can be fully determined, provided the measurement is done with a spectral resolution comparable to, or better than the spectral correlation of the medium. This was achieved by using a tunable continuous-wave laser and measuring several monochromatic transmission matrices for a set of closely spaced wavelengths (Andreoli *et al.*, 2015; Mounaix *et al.*, 2016).

Another possibility, complementary to the first one, consists of measuring a time-resolved matrix, which can be conveniently achieved when using broadband light via low-coherence interferometry. Since the interference between the transmitted light and the reference beam only takes place when their path length difference lies within the (short) coherence length of the source, it means that the recorded interferogram contains information only about a given fraction of the light, which had a time of flight defined by the path delay of the reference beam. By varying the length of the reference arm, it is therefore possible to achieve a time-resolved measurement. This technique was implemented in reflection (Choi *et al.*, 2013; Kang *et al.*, 2015), as well as in transmission (Mounaix, Defienne, and Gigan, 2016).

B. Light manipulation through the opaque lens

Digital tools have provided a way to change the configuration of the light incident on an opaque lens in a controlled way. We will see that, even prior to the measurement of the transmission matrix of a complex medium, wave front shaping tools have allowed some light control through the opaque lens. Here we take a didactic rather than an historic approach to introduce the different techniques and concepts that have been applied to this problem.

1. Time reversal, analog, and digital phase conjugation through the opaque lens

The concepts of phase conjugation and time reversal tell us that, thanks to the reversibility and reciprocity of the wave equation, an initial input wave can be recovered when the wave resulting from the scattering of the incident wave by the slab is phase conjugated and sent back through the medium. In practice, such a procedure requires perfect phase conjugation, and thus a collection of all the scattered light on both sides of the slab. In real experiments with the slab geometry, however, we generally have access only to one side of the medium and to a limited fraction of the incident light as well as of the scattered light. As was shown both in optics and in acoustics, in the case of multiply scattering materials (and also in the case of chaotic cavities) even limited phase conjugation or incomplete time reversal can partially reconstruct the initial wave (Derode, Roux, and Fink, 1995; Draeger and Fink, 1997; Calvo and Pastawski, 2010). In essence, the different modes that are phase conjugated contribute in a constructive way to reinject energy into the initial mode. If the initial mode originates from a particular position, the wave will refocus to

this position, with an efficiency that depends on the fraction of the energy that is phase conjugated.

Optical phase conjugation (OPC) was first performed by recording a hologram on a photographic plate (Leith and Upatnieks, 1966). However, based on the emergence of nonlinear optics in the 1960s and 1970s, it was suggested by Yariv (1976) that this holographic optical phase conjugation could be performed in real time, using various nonlinear processes. An implementation of this concept was first realized via four-wave mixing (Bloom and Bjorklund, 1977; Yariv and Pepper, 1977; Yariv, 1978), and via stimulated Brillouin scattering (Králiková *et al.*, 1997), in liquid crystals (Karaguleff and Clark, 1990), or using three wave mixing (Voronin *et al.*, 1979; Ivakhnik *et al.*, 1980). For a review on OPC, see Fisher (2012).

For complex media investigations, OPC suffers, however, from several shortcomings that are mainly due to the limitations of the physical effects giving rise to the phase conjugate of an optical wave. Nonlinear wave mixing (Gower and Proch, 1994) is usually complex to implement, as it requires nonlinear crystals, specific wavelengths, and often intense laser sources. Nonetheless, phase conjugation has been employed since its early days to refocus through a complex medium (Yariv, Fekete, and Pepper, 1979). Photorefractive crystals are another alternative for OPC, which, albeit being slow, was successfully used to refocus through thick biological tissues (Yaqoob *et al.*, 2008). Recently, new photorefractive materials have provided very high conjugation speeds comparable to fast SLMs (Farahi *et al.*, 2012; Y. Liu *et al.*, 2015). Gain media (such as laser crystals) also typically provide very fast OPC but work only for a narrow spectral range. They allow for amplification of the phase-conjugated wave (Feinberg and Hellwarth, 1980) and have been used for imaging in turbid media (Jayet, Huignard, and Ramaz, 2013). Three wave mixing is fast and broadband, but is only effective over a very small angular range, yet was used for imaging through turbid media (Devaux, Guiot, and Lantz, 1998). Despite all its constraints, OPC has the advantage that it can conjugate a very large number of modes simultaneously over the surface of the OPC material (Xu, Liu, and Wang, 2011), typically 1 or 2 orders of magnitude larger than what is currently achievable by digital means. OPC therefore remains a very competitive technique, especially for biomedical applications.

Thanks to the emergence of digital SLMs, it is now possible to envision a digital counterpart of optical phase conjugation (DOPC). Provided one can measure the complex amplitude of a field, an SLM can in principle generate its phase conjugate. First experimental demonstrations of this concept were performed to cophase several beams through a fiber bundle (Paurisse *et al.*, 2009), then applied to a thin scattering slab (Cui and Yang, 2010) and later to multimode fibers (Lhermite *et al.*, 2010; Papadopoulos *et al.*, 2012). In all cases, an input beam is incident on the medium and the transmitted light is recorded on a camera that has to be matched pixel to pixel to a spatial light modulator situated in a conjugated plane by means of a beamsplitter (see Fig. 19). One then needs to recover the field on the camera and display the corresponding pattern on the SLM so that a laser beam reflected off this SLM carries the phase-conjugated wave front. In its simplest implementation, off-axis digital holography provides the necessary tool for both operations: A reference plane wave interferes at an angle with the unknown input wave, producing an interferogram on the camera that contains the phase and amplitude information of the unknown input field. It can be shown that the same tilted reference plane wave diffracting off the same interferogram now displayed on the SLM will generate the phase conjugate of the unknown wave field, thus producing a refocusing on the source.

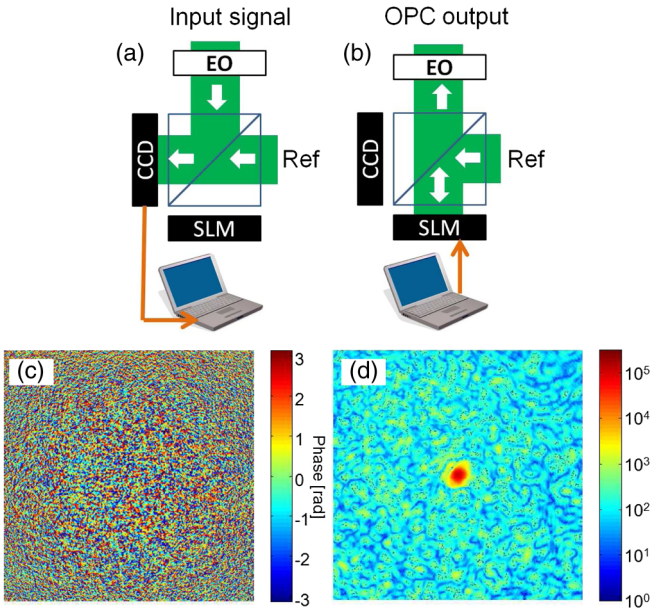

FIG. 19. Principle of digital optical phase conjugation (DOPC): (a) in a recording step, the interference pattern between a reference wave and the signal to be phase conjugated is recorded on a CCD, phase shifting their relative phase difference with an electro-optic (EO) modulator. In a digital playback step (b), the recorded pattern is displayed on the SLM, and the same reference beam, diffracting on the SLM, generates the phase-conjugate beam: (c) the DOPC measured phase profile, and (d) the measured signal at the OPC output before the opaque lens, showing a strong focus in the center, on the original signal mode. Adapted from Cui and Yang, 2010.

Although it cannot match conventional OPC in terms of number of modes, DOPC has several advantages compared to its analog counterpart, in particular, to conjugate a speckle field. Specifically, since the complex wave fronts are actually recorded in a memory, it is possible to record the output for different waves and then replay them at a later time in any order, which is not possible in analog phase conjugation, where the hologram engraved in a crystal is transient by nature. Even more interestingly, it is possible to modify the interferogram before displaying it on the SLM, or combine several holograms together, which also brings an additional flexibility compared to its analog counterpart, a feature that will become particularly important as seen in later examples related to imaging. Still, rather cumbersome alignments are required (Cui and Yang, 2010), although simplified implementations were proposed (Hillman *et al.*, 2013). A promising direction to simplify DOPC is to design a unique monolithic device that would play the role of the detector and the modulator simultaneously (Laforest *et al.*, 2012).

2. Focusing and iterative optimization

The seminal experiment by the group of Allard Mosk in Twente published in 2007 (Vellekoop and Mosk, 2007) expanded this concept of OPC to a new level by removing the need for a source. In essence, instead of recording a wave front from a source and then reemitting its phase conjugate, thus achieving refocusing, they proposed an iterative optimization technique to find the optimal wave front at the input of a disordered slab that would maximize the intensity at a given position at the other side of the slab. In this experiment, each pixel controlled on the SLM is assumed to generate an independent speckle on the far side of the disordered slab on a camera. The resulting speckle on the camera therefore corresponds to the coherent sum of all the speckle contributions from all input pixels, which by itself is also a fully developed intensity speckle pattern, since each speckle grain at the output is the result of a sum of different contributions with uncorrelated phases. In the formalism of the transmission matrix, it means that the field on pixel m is given by $E_m = \sum_{n=1}^{N} A_n t_{mn} e^{i\phi_n}$, where A_n is the field incident on input pixel n, ϕ_n is the phase delay (or advance) imposed by the SLM at the pixel, and t_{mn} is the transmission matrix of the complex medium between the pixels of the SLM and those of the CCD. By optimizing the phase ϕ_n at each input pixel (i.e., by modifying the spatial wave front) to maximize the intensity on a given output position, it is possible to converge to a constructive interference at this target position. A simple qualitative way to understand this process is to remember that the intensity distribution of a speckle is the consequence of the fact that each speckle grain is a sum of phasors (complex amplitudes) with uncorrelated and evenly distributed phases. When optimizing the phase of N input pixels, the situation where the N contributions add with uncorrelated phases is changed to a situation where N contributions all add in phase. This corresponds to an increase of the final amplitude of the order of $\sqrt{N}$ and accordingly to an increase of the final intensity that scales with N (Vellekoop and Mosk, 2007), where N is the number of pixels controlled. In the first realization (Vellekoop and Mosk, 2007), a focus more than 2000 more intense than the average of the unoptimized speckle background was observed (see Fig. 20).

This important result deserves extensive comments. First, the methodology assumes full independence between the different speckles generated by each pixel, i.e., no correlations must be present, which is one of the main assumptions for the opaque lens. This makes the optimization process very simple, since there is a unique optimum (up to a global phase) that any algorithm can find. Only when noise or decorrelation comes into play will different algorithms perform differently (Vellekoop and Mosk, 2008a). We detail in Sec. V.B what happens when correlations are present and how the results are modified. Second, it is interesting to link this approach with phase conjugation. Indeed, it can be shown that the final wave front is very close to the phase-conjugate solution or, more precisely, to the phase conjugate of the field emitted by a source placed at the target position, with the important advantage, however, that no source is required. An important difference with respect to OPC is that the SLM is phase only, so while the spatial phase corresponds to the phase-conjugate

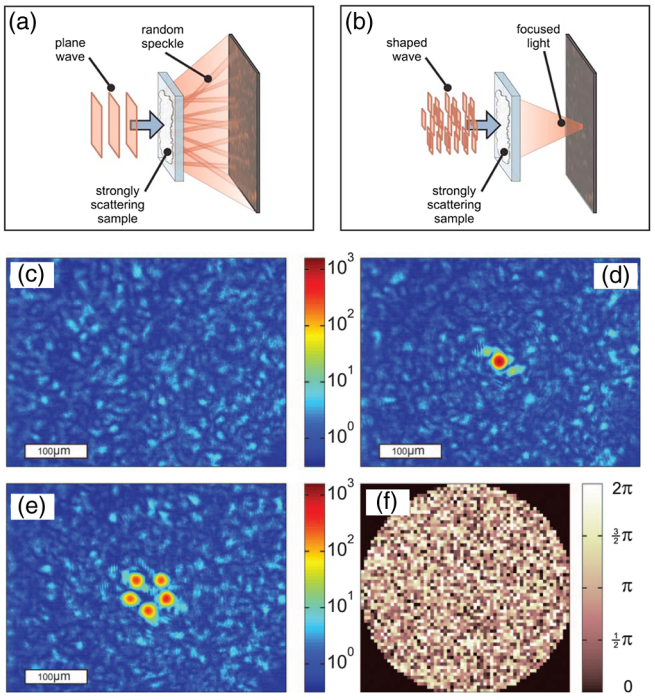

FIG. 20. Principle of wave front optimization through a complex medium: A plane wave (a) incident on an opaque multiply scattering layer of white paint gives rises to a speckle field on the far side (c). After optimization of the wave front, an optimally shaped wave (b) gives rise to a speckle field that has a strong focus at a chosen position (d). (e) A wave front can also be focused on several positions at the same time. (f) Typical phase mask on the SLM after optimization, showing the apparent randomness and high complexity of the obtained solution. Adapted from Vellekoop and Mosk, 2007.

solution, the amplitude cannot be controlled and depends on the illumination: it is constant for a plane wave incident on the SLM. Still, the wave produces a focus, corresponding to the earlier insight in acoustics that the phase is the most important parameter when the aim is to put a maximum energy at a given point: In terms of signal-to-noise ratio, it was even shown that the focusing efficiency is nearly equivalent to the one expected for perfect phase conjugation (Derode, Tourin, and Fink, 1999, 2001a, 2001b). Additionally, with the assumption of independence of the input modes and of uncorrelated elements of the transmission matrix, the background speckle is not statistically modified when the wave front is optimized, nor is the energy of the total transmission. We study deviations from this behavior in more detail in Sec. V.B.

Another important feature of the focusing effect is the spatial size of the focus. The output speckle field has a well-defined grain size which corresponds to its $C^{(1)}$ spatial intensity correlation (see Sec. III.B). The optimization procedure can locally create a constructive interference, and the spatial extent of this focus is given by the correlation distance, i.e., of the size of a speckle grain. This has two important consequences that have led to the concept of the "opaque lens" (Vellekoop, Lagendijk, and Mosk, 2010): (i) The optimized focus is perfect, in the sense that it is diffraction limited, without aberrations, and it sits on a speckle background that can be orders of magnitude lower in intensity. (ii) The size of

the focus is given only by the $C^{(1)}$ correlation of the medium in this plane, which is independent of the entire optical system located in front of the slab and its possible imperfections. Hence one can overcome the diffraction limit imposed by the limited angular apertures and the imperfections of the optical system. It is interesting to note that the same concept was previously proposed in adaptive optics to maximize a focus intensity by dithering the phase of multiple elements (Bridges *et al.*, 1974), albeit with only a few degrees of control. In contrast to this last work, the optimization through a multiply scattering medium requires a very large number of degrees of freedom to be effective, but takes advantage of the statistical properties of the speckle to have a well-defined focusing efficiency and focus size. We also refer the interested reader to a review on optimization methods (Vellekoop, 2015).

All the previously described techniques can be used to focus light to a single speckle grain. Digital phase conjugation and optimization techniques readily provide the wave front that focuses light to one or multiple targets, with the difference that optimization provides a phase-only approximation of the exact phase-conjugated field. In the case in which the transmission matrix is recorded, the corresponding wave front can also be directly computed and displayed using an SLM. As described by S. M. Popoff *et al.* (2010), the input field $\tilde{\mathbf{E}}^{\text{in}}$ that approximates the desired target $\tilde{\mathbf{E}}^{\text{target}}$ can be deduced from the matrix as

$$\tilde{\mathbf{E}}^{\text{in}} = \tilde{\mathbf{t}}^{\dagger}\tilde{\mathbf{E}}^{\text{target}}, \tag{53}$$

where $\tilde{\mathbf{E}}^{\text{target}}$ is set to 1 at the desired focus (or focii) position, and 0 elsewhere. To understand this, let us go back to the fundamental relation $\tilde{\mathbf{E}}^{\text{out}} = \tilde{\mathbf{t}}\tilde{\mathbf{E}}^{\text{in}}$, which would suggest that to get a desired output field, one needs to invert the transmission matrix. Inversion is, however, rather unstable; an inversion is also suboptimal for focusing since it would try to match the output as closely as possible, including minimizing the field outside of the focus. Taking instead the Hermitian conjugate of $\tilde{\mathbf{t}}$ as in Eq. (53) amounts to a time reversal (or phase conjugation) of the transmitted field (Prada and Fink, 1994). Since, however, the reflected field and the unmeasured modes are not part of the time reversal (for a unitary $\tilde{\mathbf{t}}$ inversion and Hermitian conjugation would be equivalent), this reconstruction is not perfect, but turns out to be stable to measurement noise. Depending on the modulation scheme, a phase-only approximation (S. M. Popoff *et al.*, 2010) or a more exact phase and amplitude input (Kim *et al.*, 2012) can be generated. All theses techniques basically provide the same phase-conjugated field as a solution and share a comparable efficiency (i.e., proportional to the number of controlled input pixels). For imaging purposes also more advanced operators can be useful, as discussed in Sec. IV.B.3.

Several general remarks can be made at this point: Phase-only and full modulation both provide comparable focusing efficiencies, up to a factor of 2 in intensity. Phase-only modulation does not diminish the overall speckle intensity and is optimal for delivering the maximal amount of energy to a given point (Vellekoop and Mosk, 2007). Amplitude-only modulation has also been shown to permit focusing (Akbulut *et al.*, 2011; Drémeau *et al.*, 2015), by essentially turning off a fraction of the input pixels to leave only pixels that contribute constructively at the focus, thus simultaneously reducing the background. Joint phase and amplitude modulation provides a compromise between signal-to-noise ratio and focusing efficiency, by diminishing the contribution of pixels that contribute little to the focus, but significantly to the background. A general comparative discussion of the focusing efficiency in the context of acoustics can be found in Tanter, Thomas, and Fink (2000) and is fully applicable in optics. In transmission, an additional control of the polarization state does not change the overall performance, except by doubling the number of modes effectively controlled.

Extensive studies in acoustics and in the radio-frequency domain are dedicated to the minimum attainable size of the focus (Lerosey *et al.*, 2007). As already recalled, far away from the scattering region the focus is limited by the speckle grain size (i.e., by the $C^{(1)}$ correlation function), and as such it can surpass the diffraction limit of conventional optics (Vellekoop, Lagendijk, and Mosk, 2010; Y. Choi *et al.*, 2011) and can get very close to the limit of $\lambda/(2n)$ allowed by diffraction. For instance, van Putten *et al.* (2011) showed that the focus could be made smaller than 100 nm for a monochromatic laser at 561 nm and a refractive index of $n = 3.41$. The possibility to modify the size of the focus by optimizing on a subpart of the momentum space forming the speckle (using a spatial mask) was proposed and realized by Di Battista, Zacharakis, and Leonetti (2015): By exploiting a fraction of the speckle with a smaller $C^{(1)}$ correlation, a focus notably smaller than the average speckle grain was demonstrated, albeit at the cost of a much lower efficiency. This was extended to arbitrary point spread functions with a transmission matrix approach in Boniface (2017). However, to break the diffraction limit and generate a focus smaller than $\lambda/(2n)$, it is necessary to have access to evanescent waves (Carminati *et al.*, 2007; Lerosey *et al.*, 2007; Pierrat *et al.*, 2013), such as just above the surface or inside the medium itself. Another approach is to use an active sink, as proposed by Carminati *et al.* (2000) and realized experimentally in acoustics (de Rosny and Fink, 2002). The possibility of using a passive sink in optics was also suggested by Noh, Popoff, and Cao (2013). Different ways of focusing *inside* the medium have been considered. One of them proceeds with a source for digital phase conjugation (Hsieh, Pu, Grange, and Psaltis, 2010), and another one works with a probe for iterative optimization (Vellekoop *et al.*, 2008). In both cases, an unambiguous proof that the focus is sub-Rayleigh is difficult to obtain. In contrast, focusing at the surface of the scattering medium can be achieved using a scanning near field optical technique (Park *et al.*, 2013). Note that when using resonant systems, such as structured metallic layers that exhibit plasmon resonances, a subwavelength focus was also demonstrated (Gjonaj *et al.*, 2011).

The ideal signal-to-background ratio η in focusing is easy to calculate and depends essentially on the number of modes controlled, e.g., for phase-only optimization it was calculated to be $\eta = (\pi/4)(N-1)+1$ (Vellekoop and Mosk, 2007). However, the effective enhancement depends on the experimental conditions as well as on the algorithm used and on the number of iterations steps for the optimization. It was also

shown that most methods are affected by the signal-to-noise ratio of the detection and are ultimately limited by shot-noise fluctuations (Yilmaz, Vos, and Mosk, 2013). Another limiting factor is the stability of the medium, which is affected by small changes over time that decrease the efficiency of the process. In practice, most reported enhancement factors range between 20% and 80% with respect to the ideal case. Genetic algorithms have been shown to be particularly efficient in low signal-to-noise situations (Conkey *et al.*, 2012).

Focusing to multiple points or to areas larger than a speckle grain is possible with all the techniques described. The total energy deposited with phase conjugation depends only on the number of degrees of control. As a consequence, the energy distributed over one or many targets is the same, but the signal-to-noise ratio is reduced by the number of modes that one seeks to control (Tanter, Thomas, and Fink, 2000). This insight was evident already from the first optimization experiment (Vellekoop and Mosk, 2007), where focusing to five spots was realized [see Fig. 20(e)], and in S. M. Popoff *et al.* (2010), where focusing on three spots yielded a threefold reduction in the focus to background intensity ratio. Interestingly, if the transmission matrix of a medium is known, it is possible not only to perform digital phase conjugation by using the conjugate transpose operator as in Eq. (53), but also to go beyond the theoretical limits of phase conjugation, or to optimize a different metric by using a more advanced operator, such as inversion for instance (S. Popoff *et al.*, 2010) (see the next section).

3. Imaging

Focusing or refocusing a wave behind a scattering medium is indeed an important milestone also for imaging. In particular, the ability to scan a focus is at the basis of many imaging techniques (e.g., multiphoton microscopy), since focusing at different points allows one in principle to form an image, e.g., by fluorescence measurement as described by Vellekoop and Aegerter (2010b). We see in Sec. V.A that in some occurrences the so-called memory effect allows one to scan an optimized focus over a narrow angular range, without the need to run an optimization algorithm for every point or to measure a transmission matrix.

Directly recovering a spatial distribution of intensity or phase from an object (i.e., direct imaging) from its transmitted speckle pattern is more challenging. The phase-conjugation operation is by nature limited in the signal-to-noise ratio when trying to form a complex shape (as determined by the ratio of input to output degrees of freedom). Optical phase conjugation, such as in Yaqoob *et al.* (2008), benefits from a very large optical etendue: Phase conjugation is effective for a very large number of speckle grains within the nonlinear crystal, thus allowing one to reform a complicated image. In a similar way and in perfect analogy to Eq. (53), the transmission matrix allows one to reconstruct an object field $\tilde{\mathbf{E}}^{\mathrm{obj}}$ from the output field $\tilde{\mathbf{E}}^{\mathrm{out}}$ through the phase-conjugation operation,

$$\tilde{\mathbf{E}}^{\mathrm{obj}} = \tilde{\mathbf{t}}^{\dagger}\tilde{\mathbf{E}}^{\mathrm{out}}. \tag{54}$$

First reconstructions were limited to very simple objects (one or two pixels turned on), using a square transmission matrix (S. M. Popoff *et al.*, 2010). Later, a more complex object (a resolution target) of $N = 20.000$ pixels could be retrieved by Y. Choi *et al.* (2011), by exploiting a transmission matrix measured over a very large number M of output pixels (the full camera). An additional advantage of the transmission matrix is that it is not restricted to phase conjugation. Other operators than phase conjugation were successfully implemented by S. Popoff *et al.* (2010), to demonstrate image recovery using, e.g., the so-called Tikhonov regularization (Tikhonov, 1963). This regularized inversion operation has a much better performance than phase conjugation and is robust to experimental noise.

4. Deterministic mixing

Another feature that can be exploited is the strong and optimal mixing produced by the opaque lens, linked to the fact that its transmission singular values follow the Marčenko-Pastur distribution. Specifically, the complex mixing of light by a multiply scattering material, that is too complex to be copied or mimicked, has been considered for cryptography and security (Pappu *et al.*, 2002). Important implications for the information capacity of such a medium have also been discussed for communication (Skipetrov, 2003). In the context of wave front shaping, this natural optimal mixedness can be exploited in numerous ways and has probably many more potential applications. Among the emerging ideas that directly exploit this deterministic and efficient mixing, one can cite the generation of quantum-secure classical keys (Goorden *et al.*, 2014) relying on the one-to-one association between an optimized wave front and a medium for few-photon states. Another interesting application is compressive imaging that can provide the reconstruction of a sparse object with only a few measurements, provided each local measurement carries global information about the object (Candes and Tao, 2006; Donoho, 2006), which is the case for a detector behind a disordered medium, as demonstrated by Liutkus *et al.* (2014).

5. Polarization control

When considering the vectorial nature of light, a question that naturally arises is that of polarization control. We have seen earlier that, at each elastic scattering event, the polarization of the scattered wave is modified in a deterministic way. In a classical picture, during a scattering event from incident wave vector $\mathbf{k}$ to a scattered wave vector $\mathbf{k}'$, the input and output polarization vectors $\mathbf{n}$ and $\mathbf{n}'$ are related by $\mathbf{n}' \propto \mathbf{n} - (\mathbf{k}'\cdot\mathbf{n})\mathbf{k}'$ (MacKintosh *et al.*, 1989). For this reason, forward and backward scattering events tend to maintain polarization, while large angle scattering tends to modify polarization more strongly. In the opaque lens case, all transmitted light has been scattered a sufficient number of times to ensure a fully mixed polarization. As a consequence, the speckle resulting from the propagation through the opaque lens also has a complex polarization state at any point, which is in general elliptic. In essence, it is the sum of two orthogonally polarized speckles, uncorrelated to each other. This feature was proposed as a way to exploit the opaque lens for polarimetric measurements (Kohlgraf-Owens and Dogariu, 2008, 2010).

It is important to point out that the polarization behavior of the opaque lens, which is universal in transmission, is clearly

system dependent in reflection. First, a single scattering contribution is always present. Just as for a reflection off a mirror at normal incidence, it has the same polarization as the input in the backreflection direction for a linear input polarization, and a reversed helicity for an elliptical input polarization. Second, the reflected light also has contributions from multiply scattered light with few scattering events that retain partial polarization memory. This second contribution strongly depends on the scattering properties of the medium (MacKintosh *et al.*, 1989). When working in reflection, it is possible to eliminate the single scattering contribution and a fraction of the light that endured few scattering events by selecting a specific polarization of the reflected light [e.g., the orthogonal polarization for linearly polarized (LP) input light], a trick used for measuring the coherent backscattering cone (van Albada, de Boer, and Lagendijk, 1990).

In the context of wave front shaping, early experiments (Vellekoop and Mosk, 2007; S. M. Popoff *et al.*, 2010) were realized by placing a polarizer between the opaque lens and the detector, so as to obtain on the camera an intensity pattern corresponding to a single scalar speckle rather than the sum of two uncorrelated speckles (Goodman, 1976). Only later was it demonstrated experimentally that this additional degree of freedom can be turned to an advantage and allows one to generate an arbitrary polarization state at the focus (Guan *et al.*, 2012; Tripathi *et al.*, 2012) (see Fig. 21). Since the total speckle is the sum of two orthogonally polarized speckles, one can generate any polarization state (linear, circular, or elliptic) at will. The final quality of the polarization state follows the usual signal-to-noise restrictions common to all phase-conjugation techniques discussed previously.

6. Temporal and spectral control

While all focusing and imaging experiments through the opaque lens discussed so far have considered a specific wavelength only, i.e., a monochromatic light source in conjunction with the spatial degrees of freedom of the medium at this wavelength, we have seen that the behavior of the opaque lens is strongly wavelength dependent—a feature that has been exploited for a long time to retrieve diffusion properties of the medium (Vellekoop, Lodahl, and Lagendijk, 2005; Curry *et al.*, 2011). Correspondingly, in the context of focusing, it was shown that if a phase pattern generates a focus for a given wavelength, then the focus will be resilient to a small wavelength variation. The corresponding bandwidth is exactly the frequency bandwidth of the medium (van Beijnum *et al.*, 2011), a property that was exploited to use the medium as a spectral filter (Small *et al.*, 2012). Performing optimization with polychromatic light is possible and has been shown to result in a narrowing of the spectrum (Paudel *et al.*, 2013). When measuring a multispectral transmission matrix (Andreoli *et al.*, 2015), it is also possible to focus several spectral components at a single or multiple positions (see Fig. 22).

In the acoustic time-reversal community, it was realized from the early days on that spatial and temporal degrees of freedom of a complex medium could be coupled (Fink, 1997). In particular, it was understood that time reversing the signal received at a given location would allow spatiotemporal focusing on the source at a specific time. Also, thanks to the reciprocity of the propagation, reemitting at the source the time-reversed signal from the detector would yield spatiotemporal focusing on the detector. Nonetheless, when performing such a single-channel time-reversal experiment in an open system, the observed spatiotemporal focusing is truly a temporal focusing only: When integrating the energy at the source position over time a significant energy increase is not observed. To truly enhance the total energy at the source position requires either multiple detectors to be time reversed simultaneously or a closed system such as a chaotic cavity (Draeger and Fink, 1997).

An analog of such a single-channel time reversal in optics was performed by McCabe *et al.* (2011). A short pulse from a femtosecond laser was sent through a layer of paint and the complex spatiotemporal speckle figure was recorded on the far side using an imaging spectrometer (see Figs. 17 and 23).

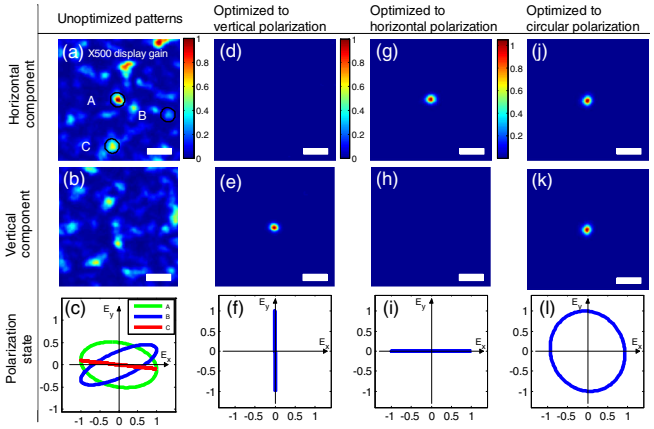

FIG. 21. Illustration of the full control of the output polarization state. Since the output polarized speckle is composed of two uncorrelated speckle patterns of orthogonal polarizations (left column), it is possible to focus independently on one or the other polarization (second and third columns). Combining the two wave fronts that focus at the same position for either polarization state, one can generate at this point a focus with arbitrary polarization (here circular, last column). Adapted from Guan *et al.*, 2012.

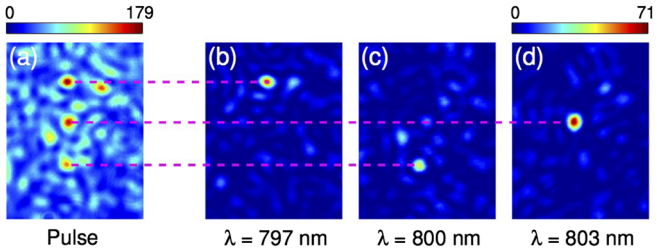

FIG. 22. Spatiospectral control of broadband light. Using the information gathered from the multispectral transmission matrix of an opaque lens, it is possible to (a) spectrally focus different spectral components of a broadband pulse at arbitrary positions. (b)–(d) Scanning in continuous mode the same laser demonstrates that each focus corresponds to a different wavelength. In this way the opaque lens is turned into a generalized grating with a spectral resolution given by its spectral correlation bandwidth. Adapted from Andreoli *et al.*, 2015.

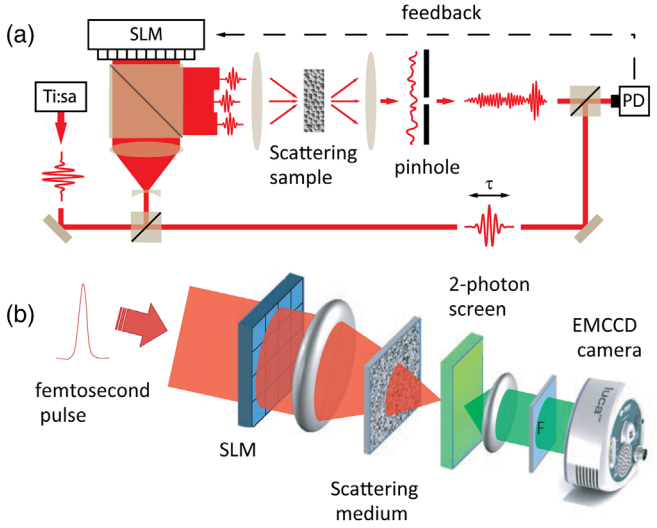

FIG. 23. Schemes for temporal focusing via spatial-only shaping. (a) Spatial shaping and optimization on the intensity at a given time delay. From Aulbach *et al.*, 2011. (b) Spatial shaping and optimization of a nonlinear signal. From Katz *et al.*, 2011.

Note that due to the difficulty of measuring and controlling an optical signal directly in the time domain, both the temporal measurement and the temporal emission were performed in the spectral domain: The temporal speckle was measured using spatially and spectrally resolved Fourier-transform interferometry (SSI) (Tanabe *et al.*, 2002), and the pulse was time shaped using a spectral shaper (Monmayrant, Weber, and Chatel, 2010). In this experiment, the time-reversed signal (measured via SSI) was sent from the source (the pulse shaper at the output of the femtosecond laser) to the detector. At the output position, it was shown that the pulse was compressed temporally close to the initial pulse duration, thanks to the reciprocity of the wave equation. Still, integrated over the pulse duration, the total intensity at the target spot was not increased. Just like spatial focusing can be seen as an extension of adaptive optics to multiply scattering material, this work can be seen as an extension of temporal precompensation of dispersion of an ultrashort pulse (Delagnes *et al.*, 2007) to the opaque lens.

While temporal control provides temporal focusing, and spatial control spatial focusing, spatial and temporal degrees of freedom are coupled in a complex medium. We now describe this spatiotemporal coupling and related experiments exploiting this effect in the opaque lens, i.e., a diffusive slab in the multiply scattering regime. As shown by McCabe *et al.* (2011), a spatiotemporal speckle along a line, as measured behind an opaque lens by SSI, has a scalar field distribution $E(x,\omega)$, characterized by a short-range spatial correlation function $\langle E(x,\omega)E(x',\omega)\rangle$ that has a well-defined width that is given by the speckle grain size and by a spectral correlation function $\langle E(x,\omega)E(x,\omega')\rangle$, whose width is directly related to the traversal time of the medium τ_T (defined in Sec. IV.A.2). These spectral correlation functions can be retrieved from the wavelength correlation within the transmission matrix $\tilde{\mathbf{t}}(\omega)$. In the time domain, a given input time t correspondingly couples to all times $t' > t$ within a few τ_T, and that coupling strongly depends on the input and output positions. This in turn means that there can be spatiotemporal couplings within this range.

This behavior can also be understood within the mode formalism: The existence of a well-defined traversal time and of this spatiotemporal coupling can be linked to the fact that in the diffusive regime the mean spacing between the modes is much smaller that their average linewidth, as characterized by the Thouless number δ defined in Sec. II.A.6. If one sends an optical pulse of duration shorter than the average transmission time of the medium τ_T, its spectrum is therefore broadband compared to the average distance between the modes. As a consequence, it couples to many different transmission modes, at different frequencies, that recombine in a complex way after the medium, thus producing a complex spatiotemporal pattern (Wang and Genack, 2011). This behavior is modified in the localization regime, where modes are spectrally isolated and where a short pulse might couple to only one of a few transmission channels (Peña *et al.*, 2014).

A consequence of the spatiotemporal coupling is that spatial shaping can generate a temporal focus at a given position, by setting a constructive temporal interference at a given time between different frequency components, as pointed out by Lemoult *et al.* (2009). This was exploited in two seminal works in optics, where spatial-only phase control over a broadband pulse was shown to be able to induce temporal focusing as well as time-integrated spatial focusing. Both approaches were based on a 2D-SLM optimization algorithm, but using different signals as a feedback. Aulbach *et al.* (2011) performed the optimization on the intensity at a given position and time using a heterodyne pulsed detection, while Katz *et al.* (2011) used a two-photon absorption signal at a given position. As this signal depends on the square of the intensity, it is proportional not only to the total energy integrated in time, but also to the average pulse duration. Both approaches are summarized in Fig. 23. As an alternative to optimization techniques, a matricial approach can also be taken. Measuring the multispectral transmission matrix (Andreoli *et al.*, 2015), it is possible to demonstrate arbitrary pulse shaping, provided the spectral phase can be addressed. This was demonstrated by Mounaix *et al.* (2016), where not only pulse recompression was shown, but also more advanced temporal functions were realized such as two pulses with a controllable delay.

Another possible approach for temporal control that was investigated is a time-resolved matrix measurement (Choi *et al.*, 2013; Kang *et al.*, 2015). These approaches have been performed in reflection geometry, mainly to achieve depth sectioning and light delivery at a certain depth, in analogy with optical coherence tomography, using ballistic light. However, they also allow for temporal focusing at the detection plane and are an alternative to spectral or nonlinear measurements.

C. Other complex scattering systems

1. Multimode optical fibers

An interesting system has recently emerged as a complex medium in optics: multimode optical fibers. Depending on the diameter of the core and the wavelength, one or many

transverse modes can be supported. If only one tranverse mode propagates within the core, then the fiber is called a single-mode fiber (SMF). When many cores are implemented in a single fiber, one talks of a multicore fiber (MCF). If the diameter of the core is increased, then the fiber can support a few modes and is called a few-mode fiber (FMF), while for many modes it is called a multimode fiber (MMF). The available number of modes scales with the diameter D of the core and with the numerical aperture (NA) as $(D \times \mathrm{NA}/\lambda)^2$, resulting in up to thousands of modes. FMFs and MMFs are increasingly considered in the context of high bitrate fiber communications for space-division multiplexing, which means using several transverse modes as independent transmission channels (Berdagué and Facq, 1982) [see Richardson, Fini, and Nelson (2013) for a review]. Spatial degrees of freedom thus come as extra degrees of freedom for information transmission, complementary to wavelength and polarization, to carry more than one channel of information on a single optical fiber. While multicore fibers (i.e., fiber bundles) have long been used as independent spatial modes (despite some cross coupling), using a single core FMF or MMF remains a challenge because of the complex nature of the modes.

An ideal MMF should support well-defined modes, where the LP mode family is generally used (Snyder and Love, 1983) to describe eigenmodes of the fiber. However, due to fabrication imperfections and bendings, the ideal LP modes are not in general the eigenmodes of the system: The eigenmodes of a large-core MMF tend to be different from the ideal case. Nonetheless, it is possible to generate the so-called "principal modes" (PMs) of an MMF (Fan and Kahn, 2005; Shemirani *et al.*, 2009), which are unaffected by modal dispersion to first order of frequency variation. Their design principle bears strong similarities with the eigenstates of the Wigner-Smith time-delay matrix described in Sec. II.C (a detailed comparison between principal modes and so-called "particlelike states" is provided in Sec. V.C). Only in the case of an ideal straight fiber where all modes have different group velocities do the principal modes coincide with the LP fiber modes. In practice, the exact phase delay is very sensitive to experimental conditions, and each mode has its own group delay, which means that a short (broadband) pulse will be stretched. Interestingly, the distribution of delay times follows a semicircle law as shown based on a suitable random matrix model (Ho and Kahn, 2011). Even for bent or long fibers, principal modes tend to remain well isolated from each other. Measurements are challenging (Milione, Nolan, and Alfano, 2015), but have meanwhile been reported (Carpenter, Eggleton, and Schröder, 2014b, 2015; Xiong *et al.*, 2016) (see Fig. 24). Without these techniques, a monochromatic input is typically injected into more than one principal mode and will give rise at the output to a complex superposition of these modes, i.e., a speckle pattern.

Many of the concepts developed to take advantage of opaque lenses for imaging and spatial and temporal control can therefore be translated to MMFs. The first set of experiments in this context is related to MCFs and FMFs that were studied in terms of their potential as high power fiber lasers and fiber amplifiers. For this class of problems, the difficulty

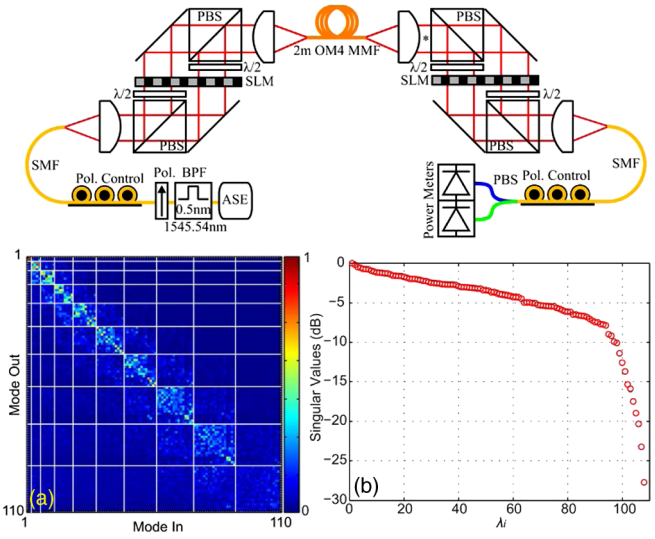

FIG. 24. Measurement of a 110×110 transmission matrix of a multimode fiber in the LP modes basis. (Top) Experimental setup: two SLMs on each side to control two polarizations are recombined on a polarizing beam splitter (PBS), allowing the near-perfect detection and injection of a well-defined mode at the input and output of the fiber to measure the corresponding coefficient on the matrix. (Bottom left) Amplitudes of the transmission matrix in the LP modes basis. (Bottom right) Singular value decomposition, showing the mode-dependent losses. In the considered weak mode-coupling limit, the transmission matrix is relatively block diagonal as subfamilies of LP modes are preferentially coupled. Adapted from Carpenter, Eggleton, and Schröder, 2014b.

is to exploit several transverse modes to achieve higher intensity. Unfortunately, due to the dispersion between the modes, the output laser mode is typically very multimode spatially, which is detrimental when high spatial quality is required. In the context of multicore fiber arrays, maintaining or retrieving a common phase between the different output modes is necessary in order to maintain a high transverse spatial quality (i.e., a beam quality factor close to unity). Corresponding cophasing methods, similar to phase conjugation, can be either passive (Lhermite *et al.*, 2007) or active using piezoelectric fiber stretchers (Yu *et al.*, 2006) or spatial light modulators (Bellanger *et al.*, 2008; Lhermite *et al.*, 2010).

Following the progress made in scattering media, this kind of monochromatic phase conjugation was extended to imaging. In particular, it was realized that, just as in a scattering medium, wave front shaping could allow the formation of a sharp focus on the far side of a fiber, be it by optimization (Čižmár and Dholakia, 2011; Di Leonardo and Bianchi, 2011) or digital phase conjugation (Čižmár and Dholakia, 2012; Papadopoulos *et al.*, 2012; Caravaca-Aguirre *et al.*, 2013; Morales-Delgado *et al.*, 2015) or even by way of measuring the transmission matrix of the fiber (Bianchi and Di Leonardo, 2012; Y. Choi *et al.*, 2012). Thanks to the ability to focus to single or multiple points, or reconstruct an image, a wide variety of imaging modalities were proposed and realized, in particular, fluorescence microscopy (Čižmár and Dholakia, 2012; Papadopoulos, Farahi *et al.*, 2013) and photoacoustic

microscopy (Papadopoulos, Simandoux *et al.*, 2013). In all these endoscopic applications images are retrieved in depth, with a diffraction-limited resolution given by the numerical aperture of the fiber. Beyond imaging, the possibility to create one or several foci at the tip of an MMF was also shown to allow optical trapping of dielectric particles (Bianchi and Di Leonardo, 2012).

Of course, the exact mode mixing in the fiber strongly depends on its specific configuration. The stability of the fiber can be extremely good when left untouched, but movements, temperature drifts, etc., may degrade the stability of the focusing considerably. Overall, this sensitivity scales with the numerical aperture of the fiber, its length, and its diameter. For example, the resilience of the transmission matrix to bending of the fiber was investigated by Y. Choi *et al.* (2012), who showed that it remained exploitable when moving the tip of the fiber by 1 cm, for a 1 m long, 200 μm diameter fiber of numerical aperture 0.48. Different methods were proposed to compensate for fiber movements, e.g., fast optimization to a point (Caravaca-Aguirre *et al.*, 2013). Another approach relies on storing a set of phase-conjugate patterns for different fiber positions and determining the fiber position at any time using a so-called "virtual holographic beacon" (Farahi *et al.*, 2013) and correlating the emission from this beacon with the set of measurements to recover the fiber position and use it for imaging. A more recent approach relies on predicting the TM by evaluating the effect of propagation and bending on the phase retardation of each principal mode (Plöschner, Tyc, and Čižmár, 2015).

In practice, many of the results of the opaque lens on imaging and focusing apply to MMFs as well, but they also have several unique features that arise from their particular propagation properties. In the weak coupling limit the correlations in the spatial pattern on the far side of the fiber strongly depend on the injection mode, because the major contributions in the transmission matrix are centered around the diagonal (see Fig. 24). The distribution of the input mode in k space (i.e., the angular range) matters: In particular, injecting a plane wave at low incidence will preferentially populate the low order fiber modes, while a strongly focused wave will result in a decomposition over higher order modes that will partially survive propagation (at least for short distance) and result at the output in variable speckle grain sizes. Symmetries are also important: A focused beam will produce qualitatively very different speckle patterns depending on the input position.

Moreover, since the number of modes is well defined and the numerical aperture is limited, the TM can be completely measured, as by Y. Choi *et al.* (2012), Carpenter, Eggleton, and Schröder (2015), and Xiong *et al.* (2016). In addition, since most of the light is transmitted in the forward direction, most singular values of the transmission value are of modulus close to unity (although, in practice, absorption and imperfect injection degrades the flatness of the distribution) (see Fig. 24, bottom right). This means that, in contrast to scattering systems, imaging is much more robust to noise and image reconstruction can be straightforwardly achieved using phase conjugation (Y. Choi *et al.*, 2012; Čižmár and Dholakia, 2012). Polarization mixing is present during propagation in MMFs (Shemirani *et al.*, 2009) and can be compensated via phase-conjugated techniques (McMichael, Yeh, and Beckwith, 1987). In the endoscopic works with digital wave front control, a control of both polarizations has been achieved (Čižmár and Dholakia, 2011). Finally, in contrast to the opaque lens, the number of modes in an MMF is limited; therefore it is possible to near-perfectly control the ouput pattern with an SLM [with 95% fidelity reported by Loterie *et al.* (2015)]. A consequence for focusing is that the fraction of light intensity that can be brought to the focus can be close to unity, thereby strongly diminishing the background speckle. This in turn means that the speckle grains are not completely independent as in the opaque lens, but are correlated, due to energy conservation and the fact that one can achieve almost complete modal control. (We see how speckle correlations affect the opaque lens in Sec. V.)

As discussed, the temporal or spectral behavior of MMFs is highly complex and of immediate relevance for telecommunications. Similar to opaque lenses, spatiotemporal coupling is present and can in principle be exploited. For instance, temporal focusing of an ultrashort pulse by DOPC was demonstrated (Morales-Delgado *et al.*, 2015). An interesting application also proposed is to use an MMF as a high resolution spectrometer (Redding and Cao, 2012; Redding, Popoff, and Cao, 2013). In essence, a fixed spatial input (a SMF) serves to inject a well-defined spatial mode that generates on the far side a complex speckle that depends on the wavelength, with a sensitivity proportional to the fiber length. The system must first be calibrated with a tunable monochromatic source. In the second step, a complex spectrum is injected and it produces on the distal side a superposition of many different speckle patterns that add incoherently, i.e., in intensity rather than in amplitude. The spectrum responsible for this pattern can finally be retrieved by inversion. As shown in Fig. 25 the resolution can be extreme for long fibers (they demonstrate 8 pm resolution for a 20 m fiber of 105 μm core, with 0.22 NA).

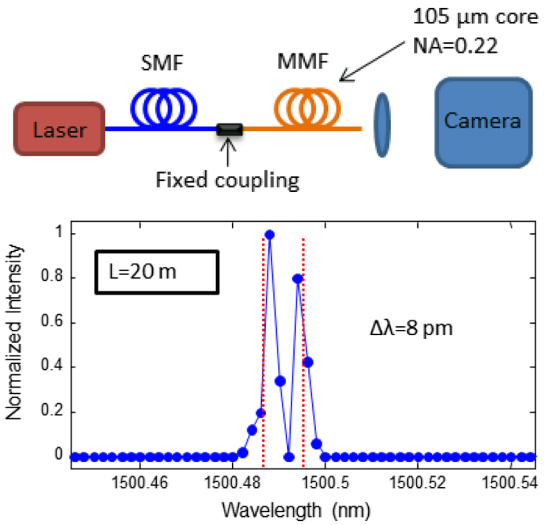

FIG. 25. Multimode fiber based spectrometer. (Top) Experimental setup. (Bottom) Example of laser line determination with 8 pm accuracy. Two laser lines separated by 8 pm can be resolved through the reconstruction from the speckle pattern. Adapted from Redding, Popoff, and Cao, 2013.

2. Biological tissues

A complex system of much interest for imaging and wave front shaping is biological tissue. While optical imaging in biological tissues is a vast field, in particular, with an endless variety of coherent or incoherent imaging techniques able to retrieve ballistic information from the multiple scattering background and depth resolution (Ntziachristos, 2010; Wang and Hu, 2012; Wang and Wu, 2012; Yu *et al.*, 2015), a commonly accepted order of magnitude for the scattering mean free path ℓ of tissues is of the order of 100 μm in the visible range. But due to the high forward anisotropy of the scattering, the transport mean free path $\ell^\star$ is usually of the order of a millimeter. Obviously, there is a strong variability from tissue to tissue, and a vast amount of literature exists on measurements of scattering properties of tissues (Cheong, Prahl, and Welch, 1990).

While most of the concepts developed in the framework of a multiple scattering slab can be adapted to biological tissues, such as focusing or imaging with wave front shaping, there are some specific questions to be addressed when dealing with imaging in biological tissues. The first one is the problem of decorrelation that is inherent to soft media: The distribution of the refractive index changes relatively rapidly with time, similar to what is encountered in atmospheric adaptive optics. Measuring the transmission matrix or running an optimization algorithm must thus be performed on a time scale comparable with the decorrelation of the medium, typically of the order of a millisecond for *in vivo* tissues. Another important aspect is that tissues are typically very thick (a few centimeters) and the distal side of it might not be accessible. At a more fundamental level, one usually wants to image or focus inside rather than through a scattering medium. For this reason, the concept of a thin slab is not directly relevant: although it is reasonable to consider that the medium up to depth D at which one wants to image is an opaque slab of thickness D to be traversed, this is, in fact, only partially true. Consider here that light can also propagate deeper than D before diffusing back to the plane at depth D that is of interest.

Workarounds for this problem of accessing the region of interest have meanwhile been developed. One of them is to try to get access to the local light intensity deep inside the tissue using a complementary technique such as acoustics. Particularly promising progress has been made in acousto-optics (Xu, Liu, and Wang, 2011; Si, Fiolka, and Cui, 2012; Wang *et al.*, 2012) and in photoacoustics (Kong *et al.*, 2011; Chaigne, Gateau *et al.*, 2014; Chaigne, Katz *et al.*, 2014) [for a review see Bossy and Gigan (2016)]. In all these techniques, the resolution is governed by the acoustic wavelength, which is typically much larger than the optical wavelength. Nonetheless, it is possible to overcome the acoustic resolution and get closer to optical speckle scale resolution, either by careful spatial coding (Judkewitz *et al.*, 2013) or by exploiting nonlinearities (Conkey *et al.*, 2015; Lai *et al.*, 2015). Another option is to rely on reflection measurements only. For instance, optimizing the wave front to maximize the total nonlinear reflected signal can force light to focus at depth (Tang, Germain, and Cui, 2012; Katz, Small, Guan, and Silberberg, 2014). It is also possible to measure the reflection matrix (Choi *et al.*, 2013) and exploit its statistical properties for imaging. Another possible idea is to use differential measurements to focus on a moving target (Zhou *et al.*, 2014). Most of these techniques have been detailed in a recent review (Horstmeyer, Ruan, and Yang, 2015).

V. MESOSCOPIC PHYSICS AND WAVE FRONT SHAPING

Wave front shaping techniques have led to remarkable progress for imaging in or through complex media. We see in this section how these techniques can be used to unravel and exploit mesoscopic effects. We explain in Sec. V.A how the memory effect has emerged as a powerful tool for imaging and describe in Sec. V.B recent optical experiments and theoretical works, where first evidence of the existence of open and closed channels was discussed. In Sec. V.C we describe the properties of time-delay eigenstates in different contexts, and in Sec. V.D new avenues for wave front shaping in media with gain and loss are discussed.

A. Memory effect

As seen in Sec. III, the information on the incident wave front is not lost when traversing a multiply scattering medium. A special role in this context plays the memory effect, where spatial variations of the incident wave front are partially mapped onto easily predictable changes in the transmitted speckle. In transmission, we saw in Sec. III.D that the thickness of the medium L determines the typical transverse spatial features that are conserved, which implies that this effect is independent of the strength of the scattering or of the exact scattering properties of the medium.

While the mechanism behind the memory effect is very general, we saw that a particularly important case is the one of a linear phase ramp on the input wave front (see Fig. 12). This angular rotation is transferred to the far side of the medium, provided that the transverse wave vector q of the phase ramp is changed only slightly, $\Delta q < 1/L$, corresponding to a variation of the angle of rotation below the so-called memory effect angle $\theta < \lambda/(2\pi L)$. More precisely, the transmitted speckle decorrelates over a characteristic angle determined by the memory effect. The shape of the angular correlation function was predicted by Feng *et al.* (1988) to be sinh, but the first experimental realization (Freund, Rosenbluh, and Feng, 1988) showed that this function is closer to an exponential decrease. The phase shift of the speckle pattern corresponds to a rotation by the same angle as the incident one, when the field propagates away from the sample. Far away from the sample (as on a distant screen) the speckle field will thus be translated. As shown by Freund, Rosenbluh, and Feng (1988), the memory effect is also present in reflection, but the corresponding angle is not given by the thickness then but by the transport mean free path $\ell^\star$, which measures the extent of the diffuse spot in reflection (as discussed in Sec. III.C).

A fundamental insight is that based on the memory effect not only linear phase ramps, but actually any arbitrary modification of the input wave front can be transferred through the medium (with a cutoff spatial frequency determined by the medium thickness L). A quadratic phase can generate a longitudinal shift of the resulting speckle far away from the sample. In a visionary paper as early as 1990

(Freund, 1990a), Isaac Freund realized that this means that an opaque layer could be used for several functions, such as a lens, a grating, a mirror, or imaging. Unfortunately, the possibilities of shaping the speckle to a focus were not yet available at that time, and the proposal relied on image correlations between the speckle of interest and a reference speckle.

1. Imaging using the memory effect

While most early work considered a plane wave input, the memory effect is also effective for an arbitrary initial input wave front. In particular, it also works when the wave front has been shaped to obtain a speckle that contains a bright focus. If the medium is thin and if the focus has been achieved at a distance, it means that the focus can be translated. This approach is particularly interesting for imaging since, using a single focus and raster scanning it around, it is possible to recover an image, for instance, of a fluorescent object, as first demonstrated by Vellekoop and Aegerter (2010b) (see Fig. 26). In such a setup, it does not matter how the focus was initially obtained, as, e.g., by optimization of the intensity on a CCD camera (Vellekoop and Aegerter, 2010b; van Putten *et al.*, 2011). When using the transmission matrix method, one naturally has the ability to focus at any measurement position. If the memory effect is present, it can be retrieved from correlations between lines of the transmission matrix corresponding to neighboring positions, as demonstrated by Popoff, Lerosey *et al.* (2011) and Chaigne, Katz *et al.* (2014). Still, the ability to move a focus by adding an angular tilt is interesting, particularly because it means fast scanners can be used to rapidly raster scan a focus, possibly orders of magnitude faster than a pixellated SLM.

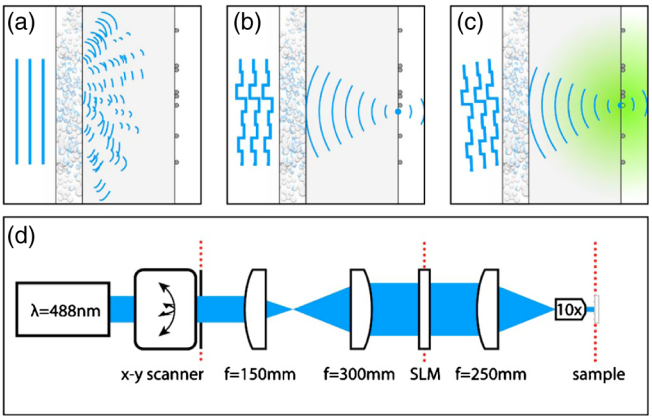

FIG. 26. Principle of imaging using wave front shaping and the memory effect. (a) A thin scattering layer blocks a fluorescent structure from sight; all incident light is scattered. (b) By use of interferometric focusing (e.g., phase conjugation or wave front shaping), scattered light is made to focus through the layer. (c) Imaging: the focus follows rotations of the incident beam over a short angular range. (d) Simplified schematic of the experimental setup for 2D imaging. A laser beam is raster scanned, and its wave front is shaped with a spatial light modulator (SLM). Dotted lines are conjugate planes. Adapted from Vellekoop and Aegerter, 2010b.

It is also possible to use the memory effect without having access to the focus region as demonstrated by phase conjugating the second harmonic signal generated by an implanted probe (Hsieh *et al.*, 2010), using the photoacoustic effect to remotely monitor the light intensity (Chaigne, Katz *et al.*, 2014), or after optimizing a nonlinear signal to a focus (Tang, Germain, and Cui, 2012; Katz, Small, Guan, and Silberberg, 2014). Also, by adding not only a linear phase shift but also a quadratic phase ramp, the technique can be extended to the third dimension for both scanning and imaging (Ghielmetti and Aegerter, 2012, 2014; Yang *et al.*, 2012).

Once a wave front was shaped by an SLM to focus at a given position, it means that a source placed at this position would be transformed by the same SLM into a plane wave and therefore can be conjugated to a focal spot by a subsequent imaging system. Based on this concept, it was then realized by Katz, Small, and Silberberg (2012) that scanning the focus is not the only way to recover an image. As discussed by Freund (1990a), the memory effect features an isoplanetic angle over which the speckle remains correlated. In other words, the correction of the wave front compensates the scattering medium for a small angle and for a small range of frequency, irrespective of the illumination. Katz, Small, and Silberberg (2012) generated a point source speckle after a scattering medium, after which an SLM is placed and the wave front is optimized to form a focus on a CCD camera, therefore performing the analog of a focusing experiment, except that the SLM is placed after the medium rather than before. The SLM is conjugated with the output plane of the scattering medium in order to maximize the memory angle range. If the point source is displaced, so is the focus image on the camera, provided the displacement is smaller than the one allowed by the memory effect. The point source is then replaced by an extended source (an object), and an image is directly obtained on the camera. Crucially, the correction even works if the object is illuminated by spatially and temporally incoherent light, but since the correction of the wave front is valid only within a given angle around the focus and for a given spectral bandwidth related to the spectral correlation of the medium around the calibration frequency, only this fraction of the light is well conjugated.

Finally, several works reverted to the original idea of Freund (1990a) of using the memory effect without shaping or focusing to image behind a turbid layer. All these approaches exploit the fact that a speckle, despite being a very complex pattern, has a well-defined peaked autocorrelation function. Bertolotti *et al.* (2012) illuminated a fluorescent object placed at a distance behind a scattering layer by a speckle that is translated (by scanning the illumination angle), and its fluorescence is collected as a function of the shift of the speckle, thus forming an image (see Fig. 27). While the resulting image is very complicated and specklelike, its autocorrelation is actually the product of the autocorrelation of the object and of the autocorrelation of the speckle, with the latter having a diffraction-limited peaked function. Therefore, one has access to the autocorrelation of the object with a resolution given by the speckle grain size. Using a reconstruction technique known as phase retrieval (Fienup, 1982), the image of the object can be retrieved from its

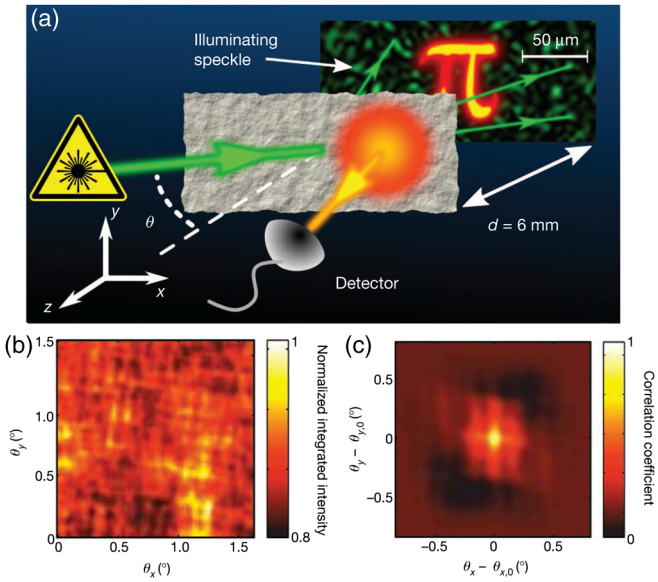

FIG. 27. (a) Schematic of the apparatus for noninvasive imaging through strongly scattering layers. A monochromatic laser beam illuminates an opaque layer of thickness L at an angle θ. A fluorescent object is hidden a distance of 6 mm behind the layer. The fluorescent light is detected from the front of the scattering layer by a camera. (b) Integrated fluorescent intensity on the camera, as a function of the incident angle $\theta = (\theta_x, \theta_y)$. (c) Autocorrelation of the intensity, averaged over nine scans taken at different values of the starting incidence angle θ_0 to average over the different realizations of the speckle. From the autocorrelation, the original image (here the letter π) can be retrieved by phase retrieval. Adapted from Bertolotti *et al.*, 2012.

autocorrelation function. Yang, Pu, and Psaltis (2014) used the same technique to recover the image of blood cells behind a scattering layer of tissues. Katz, Heidmann, Fink, and Gigan (2014) studied another case, where a semitransparent object, illuminated by spatially incoherent light, could be retrieved from the autocorrelation of the speckle it produced behind a scattering layer. In all these approaches, no calibration is required, since the exact scattering properties of the scattering layer are not important. However, in most of this work, a scattering layer rather than a scattering volume was used to ensure light transmission and a very pronounced memory effect.

2. Beyond the conventional memory effect

While the memory effect is mostly considered in transmission, it is also present in reflection (Freund, Rosenbluh, and Feng, 1988) and can be exploited. As mentioned in Sec. III.D the limiting memory effect angle in reflection depends on the transport mean free path ℓ^*, which determines the size of the diffusive halo for focused incident light. For a sufficiently strongly scattering material such as a paint layer, where the mean free path can be on the order of a micrometer, the angular range of the memory effect can be of several degrees. The relatively large fields of view resulting from this estimate have been exploited, for instance, by Katz, Small, and Silberberg (2012) and by Katz, Small, Guan, and Silberberg (2014) to image "around corners." The memory effect was also studied in the context of time reversal (Freund and Rosenbluh, 1991) and polarization (Freund, 1990b).

An important point in the quest toward exploiting the memory effect for biological imaging (see also Sec. IV.C.2) is to assess whether some memory effect can be present inside a biological tissue. For some biological systems the scattering occurs mainly on a thin layer at the surface, and the rest of the sample is mostly transparent. This is the case for the drosophilia puppa at its early development stages, where the fly embryo is covered in a thin (8 μm) but very scattering layer of cells (Vellekoop and Aegerter, 2010a). Inside a volumic scattering medium, which is the case of interest for deep biomedical imaging, one would expect from mesoscopic theory that the memory effect is not present, since in the derivation it is supposed to be the only observable at a distance from the scattering layer. However, some works indicate that this view is conservative. Indeed, tissues typically have a scattering mean free path ℓ of 50–100 μm (Cheong, Prahl, and Welch, 1990) and, more importantly, they scatter mostly forward with g parameters (the average of the cosine of the mean scattering angle) often larger than 0.9. This means that, at small depth (millimeters), there are still forward scattered photons, and the diffuse halo is narrower than the one given by a fully diffusive model. Experimentally, in some instances, a thin scatterer (onion layer, chicken breast slice, or fixed brain slice) could be used for imaging within its memory effect range, which was characterized to be larger than predicted by a diffusive model (Katz, Small, Guan, and Silberberg, 2014; Schott *et al.*, 2015), a strong indication that the memory effect should be present inside a medium. Tang, Germain, and Cui (2012) were able to focus at a depth inside brain tissues (800 μm) and scanned over a few micrometers. In forward scattering media such as biological tissues, a translational memory effect was identified: A lateral shift of the input wave front resulted in a lateral shift of the focus (Judkewitz *et al.*, 2015), an effect valid inside the medium rather than at a distance.

Analogs of the angular memory effect were also demonstrated in MMFs. Here the memory effect is not transverse, but longitudinal. This comes from the fact that a plane wave with a given k vector that is injected is mixed angularly but not radially, provided the fiber is not too long or twisted, producing at the output a narrow cone of speckle with the same transverse angle of incidence. The width of this output cone corresponds to an azimuthal correlation of the speckle. This means that any radial curvature to the initial wave front can be transferred to the output. Čižmár and Dholakia (2012) brought light to a focus by wave front shaping at the distal end of an MMF. Using those azimuthal correlations, the focus was shifted axially, but also elongated to produce a Bessel beam (McGloin and Dholakia, 2005), a doughnut-shaped focus for stimulated emission depletion (Willig *et al.*, 2007) and more generally for engineering the point spread function. There is also a rotational memory effect, coming from the fact that a MMF conserves some rotational symmetry, which can be used to rotate a focus around its center of symmetry (Amitonova, Mosk, and Pinkse, 2015; Rosen *et al.*, 2015).

B. Bimodal distribution of eigenchannels

We saw in the previous section how the TM of a disordered slab, a multimode fiber, or any linear optical system can be measured. However, it is important to stress the difference between the TM $\tilde{\mathbf{t}}$ as measured in experiments and the full TM $\mathbf{t}$ as described in Secs. II and III. The experimental TM $\tilde{\mathbf{t}}$ takes as input the different modes that can be generated and detected by modulating the input beam, i.e., typically pixels on an SLM and on a camera, respectively. In the opaque lens, the number of controlled modes is typically much smaller than the number of available input modes of the medium. In addition, the number of detected modes is much smaller than those being populated at the output of the slab. One of the most striking features of mesoscopic transport, the bimodal distribution of eigenchannels (see Fig. 3), is however elusive when measuring only a subpart of the full TM of the system. In all the different works on the subject, the ratio of modes that are controlled, detected, or illuminated is always the limiting parameter. There is no consensus on notation or even on the definition of this ratio that is defined and labeled differently in every paper, and that depends on the specific situation. In this section, we chose to leave the different definitions (and notations) as they were in the literature and point out when they differ.

1. Accessing the bimodal distribution

Since a complete channel control for accessing open and close channels is currently not available, it is helpful to resort to simulations, as in W. Choi *et al.* (2011), where the full monochromatic transmission matrix of a disordered slab is numerically evaluated. The numerical data are in good agreement with RMT (Nazarov, 1994), and the resulting modes when injecting open and closed channels are evaluated. A striking result is shown in Fig. 28, where the intensity distribution inside the medium and the scattered fields are computed for plane wave input as well as when injecting the optimal wave front for exciting an open or closed channel. One can see a dramatic difference in the intensity distribution along the longitudinal direction when comparing these different cases. When injecting a plane wave, which excites all available transmission channels very broadly, the averaged intensity diminishes linearly with depth, as predicted by Ohm's law. When the wave front corresponds to injecting a closed channel, the decay is much faster and exponential, while when injecting an open channel the intensity first increases with depth until the center of the slab, and only diminishes thereafter. As a result, the intensity is almost symmetric with a maximum in the center of the slab, as necessary in order to transmit a significant amount of energy through the medium. Analytical expressions for these distribution functions were proposed by Davy, Shi, Park *et al.* (2015).

Note that this description considers a simplified system, which serves as a good starting point to understand the difficulty to measure this distribution and inject the corresponding modes in practice: It is assumed that all modes are accessible (from both sides of the slab, including also the polarization degrees of freedom), and that the system is two dimensional only (as in Sec. II for the waveguide geometry).

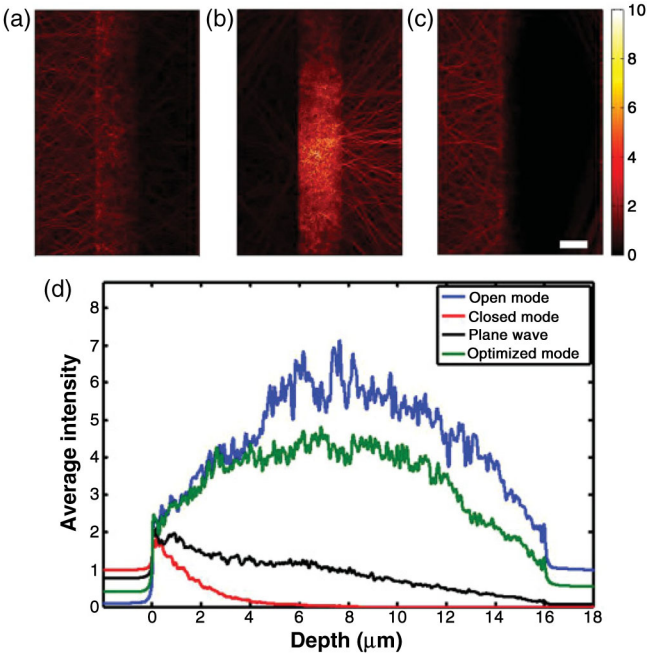

FIG. 28. Simulation of scalar field distributions of transmission eigenchannels inside a 2D disordered slab with 299 channels. The medium of height 130 μm and thickness 16 μm is shown in the middle of each of the three top panels (a)–(c). Field distributions (a) of a plane wave whose incident angle is 11.5°, (b) of an open transmission eigenchannel (transmission of 0.955), and (c) of a closed transmission eigenchannel (close to zero transmission). The incident field is subtracted on the left-hand side of the medium. Color bar: amplitude normalized to the input wave. Scale bar: 10 μm. (d) Averaged intensity along the x direction as a function of the depth in the z direction for the same three different input wave fronts, plus the wave front corresponding to a focusing optimization as in Vellekoop and Mosk (2008b). The disordered medium fills the space between 0 and 16 μm in depth. The intensity is normalized to that of a normally incident plane wave. Adapted from W. Choi *et al.*, 2011.

First experiments which could satisfy these demanding requirements were reported in acoustics (Gérardin *et al.*, 2014) and in optics (Sarma *et al.*, 2016). In both setups the dramatic change in the internal energy distribution (see Fig. 28) could, indeed, be observed. In most experiments, however, these conditions are difficult to meet in practice.

An analytical model and numerical simulations in the waveguide geometry (Goetschy and Stone, 2013) were dedicated to what happens to the distribution of measured transmission eigenvalues in the case of partial channel access (considering both control and detection), and how it affects the maximal transmission $T_{\max}$ that can be achieved by wave front shaping when injecting the maximally open channel that can be measured. For this purpose the control parameter $m = M/N$ was introduced, where M is the number of channels controlled and N is the total number of channels. The most striking result is that even a small degree of imperfect control ($m \lesssim 1$) abruptly suppresses the mode of unit transmission, and the measured distribution rapidly deviates from the bimodal one, with the disappearance of the peaked distribution around unity (see Fig. 29). An increase

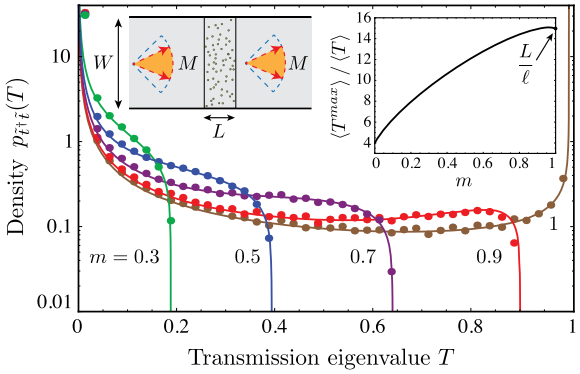

FIG. 29. Transmission eigenvalue density of a disordered slab placed in a waveguide with $N = 485$ channels (length $L = 150/k$, width $W = 900/k$), for different fractions of controlled channels $m = M/N$. Numerical results (dots) are obtained from solving the wave equation for 120 realizations of the slab for fixed disorder strength. The solid lines are the theoretical prediction based on free probability theory. The inset shows the maximal transmission enhancement possible for a given m. Adapted from Goetschy and Stone, 2013.

of the transmission relative to the mean transmission (i.e., $T_{\max} \gg \bar{T}$) can nonetheless be achieved with partial control, until the distribution converges to the Marčenko-Pastur distribution [as in Eq. (52) and Fig. 16]. Interestingly, the crossover to uncorrelated Gaussian matrices occurs when the number of modes controlled is lower than the total transmission T. Similar results are derived in reflection, where the perfect reflection expected when injecting closed modes is suppressed with imperfect control and detection. In particular, detection or control of a single polarization immediately results in loss of half of the modes. The result by Goetschy and Stone (2013) was extended by Popoff *et al.* (2014) to include not only the waveguide geometry, but also the slab geometry with partial illumination. In particular, the effective control parameter m is extended for the case of an illumination zone D smaller than the thickness L of the slab. Because of the fact that the area of the diffusive halo on the far side is larger than the injection area, the number of modes at the output is automatically larger than the number of input modes, which results in a diminution of the maximal transmission achievable.

2. Unraveling and exploiting open and closed channels

Despite these difficulties in accessing the full bimodal nature of the transmission eigenchannels of a disordered slab, several experiments have managed to reveal some features of bimodality by means of wave front shaping.

Historically, the first experimental result was reported by Vellekoop and Mosk (2008b), where an optimization through a slab was performed in the limit where a noticeable fraction of the modes is controlled (up to approximately 30% at the input). Experimentally, this was achieved in two ways: first by designing a relatively thin multiply scattering sample (down to 5.7 μm) to minimize the number of modes to be controlled; second by controlling and detecting both polarizations using polarization separators and using high numerical aperture

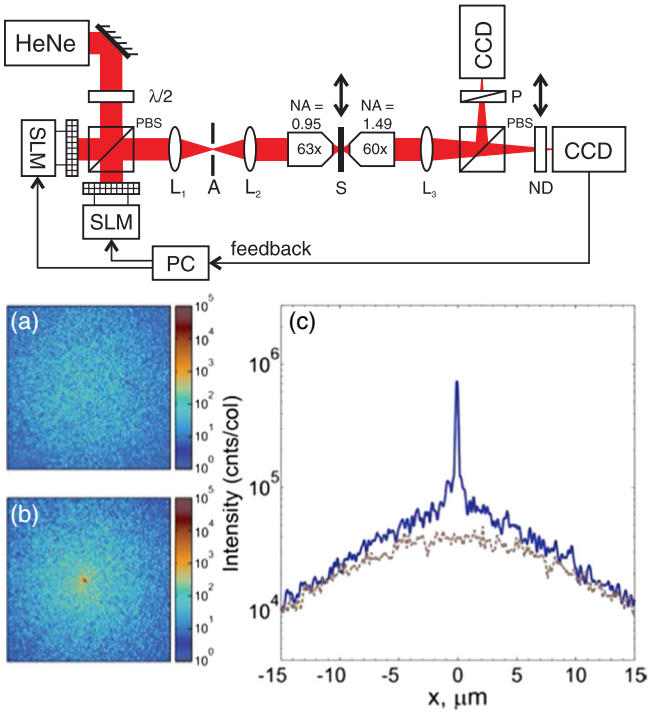

FIG. 30. Coupling to open channels by wave front optimization to a focus spot. (Top) Schematic of the experiment: two SLMs are used to control both polarization directions, high numerical aperture objectives ensure maximal coverage of incident angles, and both polarizations are detected on two CCD cameras on the far side. (Bottom) Intensity of the transmitted speckle figures at the output plane (a) before and (b) after optimization of the wave front. (c) Intensity summed over the y direction to average the speckle: dashed curve for unoptimized and solid curve for optimized wave fronts. The total transmission is increased by 35%. Adapted from Vellekoop and Mosk, 2008b.

objectives to access high angles of incidence. The result when performing the same point optimization as in Vellekoop and Mosk (2007) was a spectacular deviation from the opaque lens predictions (see Fig. 30). While optimizing a single speckle spot, an increase of the overall transmitted intensity was observed, not only in the focus, but also in the surrounding speckle, which meant that strong spatial correlations must be present in the speckle, due to the fact that only a few modes contribute to the transmitted speckle. The increased transmission was compared with RMT predictions and could be well interpreted as a redistribution of the input energy from closed to open channels.

They further derived that perfect optimization to a single point should, on average, increase the total transmission to the universal value of $2/3$. This value of $2/3$ is directly linked to the electronic quantum shot noise for the case of a bimodal distribution of transmission eigenvalues (Beenakker, 2011), which we have found to be characterized by a sub-Poissonian shot-noise Fano factor $F = \mathrm{tr}[\mathbf{t}\mathbf{t}^\dagger(1 - \mathbf{t}\mathbf{t}^\dagger)]/\mathrm{tr}[\mathbf{t}\mathbf{t}^\dagger] = 1/3$ in the diffusive limit (see Sec. II.B). Indeed, when aiming to maximize the intensity to a given position, Eq. (53) tells us that this can be achieved through phase conjugation $\mathbf{E}^{\mathrm{in}} = \mathbf{t}^\dagger \mathbf{E}^{\mathrm{target}}$ (we neglect here for the moment that in the experiment only $\tilde{\mathbf{t}}$, i.e., the partial transmission matrix restricted to

the measured and controlled modes is available). The output field, in turn, is given as $\mathbf{E}^{\text{out}} = \mathbf{t}\mathbf{t}^{\dagger}\mathbf{E}^{\text{target}}$, and the total intensity is $I^{\text{out}} = |\mathbf{E}^{\text{out}}|^2$. When averaging over realizations or over target positions, one can show that the average transmission is $\bar{T} = I_{\text{out}}/I_{\text{in}} = \text{tr}(\mathbf{t}\mathbf{t}^{\dagger}\mathbf{t}\mathbf{t}^{\dagger})/\text{tr}(\mathbf{t}\mathbf{t}^{\dagger})$. Since this relation is directly related to the shot-noise Fano factor by $\bar{T} = 1 - F$, we simply get the result $\bar{T} = 2/3$. This result was numerically confirmed by W. Choi *et al.* (2011), where it was further noted that this result is connected to the fact that the contribution of each eigenchannel n to the optimized wave front was, on average, proportional to its eigenvalue $|\tau_n|^2$, a well-known property of the time-reversal operator $\mathbf{t}\mathbf{t}^{\dagger}$ (Tanter, Thomas, and Fink, 2000). This theoretical result was later verified experimentally by Kim *et al.* (2013). Of course, imperfect control of the wave front leads to a reduced transmission compared to the ideal case. Vellekoop and Mosk (2008b) introduced a parameter γ that represents the overlap between the injected mode and the perfect optimized mode, with the difference coming from imperfect channel control, phase-only operation, and noise in the optimization process. The expected total transmission is $T_c = |\gamma^2|\bar{T}$, and excellent agreement in different experimental conditions is found.

In contrast to the opaque lens case, optimization and imaging through a medium gives quite different results if the number of open channels becomes lower than the number of degrees of freedom that one has access to. As shown by Vellekoop and Mosk (2008b), when optimizing a single point, the background increases, which means that the signal-to-background ratio is lower than expected from the opaque lens analysis. This effect was discussed by Davy, Shi, and Genack (2012) in the context of microwaves but the result remains valid for optics. In essence, the signal to background in a point optimization experiment is bounded by the number of transmitting modes and can be down to 1 (no optimization) in the single open channel regime (Peña *et al.*, 2014). Of course, in this limiting case, the intensity at the focus has been indeed increased, but since there is only a single mode that dominates the transmission, the background has also increased correspondingly.

Several works have also reported on measuring a TM and subsequently injecting the mode with the largest transmission. Kim *et al.* (2012) explored the limiting case of a very sparse measurement: A square transmission matrix was measured over a single polarization and a very limited angular view (covering a numerical aperture of NA $\simeq 0.32$). In this configuration, the quarter-circle law, which corresponds to the Marčenko-Pastur distribution for a square random matrix, is expected [see Eq. (52)]. While this distribution had already been measured in optics by S. M. Popoff *et al.* (2010), they showed that when sending the input vector corresponding to the highest transmission mode given by the measured transmission matrix, they recovered a higher transmission by a factor of 3.99 relative to the mean transmission within the detection angle, in good agreement with the fact that the distribution of eigenvalues is bounded to twice the mean amplitude transmission in the case of a square random matrix (corresponding to a factor of 4 in intensity). Kim *et al.* (2014) reported on the promising use of a binary amplitude modulator to measure the TM and to inject eigenchannels. They showed that such a binary modulator is able to match the calculated mode for single-mode injection with 40% fidelity and demonstrated a twofold increase of transmission over the mean transmission in the detection angle of their apparatus. Measurements of very large TMs in strongly scattering media to approach the bimodal distribution have been reported by Yu *et al.* (2013) and Akbulut *et al.* (2016). In both studies, deviations from the Marčenko-Pastur distribution were observed and could be qualitatively modeled, but due to limited control the direct observation and injection of open channels in optics has so far not yet been reported [see Gérardin *et al.* (2014) for a first realization of open channels in acoustics].

Another possibility of high practical interest is to measure the reflection matrix. When sending the mode with the lowest reflection, a high transmission should be obtained. This idea was experimentally implemented by Kim *et al.* (2015) where a threefold increase in transmission is reported when injecting the mode with the smallest eigenvalue in reflection.

An alternative to single-point optimization was reported experimentally by Popoff *et al.* (2014); see Fig. 31 for a corresponding illustration. Instead of measuring a single position and observing an increase of the transmission, here the total transmitted intensity was optimized directly. In order to detect all modes at the output and not to be limited by collection optics, a large-area photodetector is directly placed on the backside of the sample, thus collecting all modes with

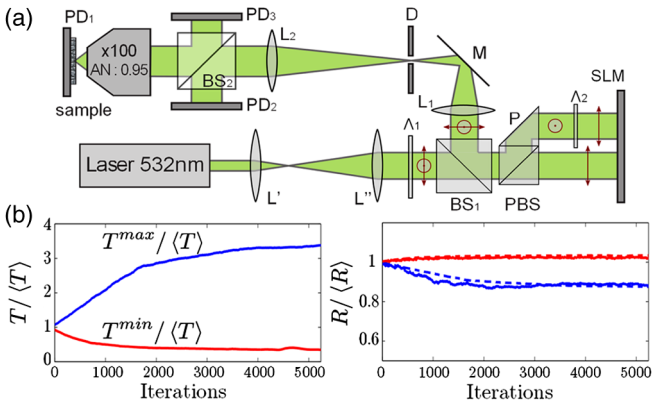

FIG. 31. Experimental setup and results for total transmission optimization. (a) Schematic of the experiment for the control of total transmission. The two polarizations of the laser are modulated by two different areas of a phase-only SLM, with 1740 macropixels controlled. The scattering sample is placed at the focal plane of the objective. Three photodetectors PD1, PD2, and PD3 measure, respectively, the intensities of transmitted, incident, and reflected light, and the optimization is performed on the total transmission T, measured as the intensity on detector PD1 normalized by the incident intensity measured on detector PD2. (b) Measured $T/\langle T\rangle$ (left panel) and $R/\langle R\rangle$ (right panel) vs the step number of optimization for enhancement (increasing blue curve) and reduction (decreasing red curve) of the total transmission. The sample is a 20 m thick ZnO layer, and the average transmission is $\langle T\rangle \sim 5\%$. The dotted line represents the reflection estimated from the transmission using $R/\langle R\rangle = (1-T)/(1-\langle T\rangle)$. Adapted from Popoff *et al.*, 2014.

the same efficiency. This is in contrast to previous results where a limited collection angle was inherent to all implementations, and therefore only partial transmission enhancements were reported, from which changes in total transmission could only be inferred. When optimizing the wave front to maximize or minimize the total transmitted intensity, an approximately 3.6-fold enhancement or a 3.1-fold reduction in transmission relative to the average could be found, respectively. To confirm that this effect was, indeed, a mesoscopic effect, the reflection was also monitored and its increase or decrease was found to be anticorrelated with a corresponding change in transmission. Yet other approaches have been proposed, e.g., optimization algorithms to maximize transmission by analyzing only the backscattered light (Jin *et al.*, 2013, 2014), or a photocurrent (Liew *et al.*, 2016). As shown both experimentally and theoretically (Hsu *et al.*, 2017) long-range-correlation effects as discussed in Sec. III.A and by Scheffold *et al.* (1997) and García-Martín *et al.* (2002) increase the dynamic range of light delivery into regions containing multiple speckles.

C. Time-delay eigenstates

In this section we discuss the interesting properties of the eigenstates of the time-delay operator or matrix $\mathbf{Q} = -i\mathbf{S}^{\dagger}(\partial\mathbf{S})/\partial\omega$ defined in Sec. II.C; see Eq. (48). Thanks to the techniques of wave front shaping discussed in Sec. IV, it is now within reach not only to measure the time-delay matrix of a system, but also to excite an eigenvector at the input, thus generating a time-delay eigenstate. We first describe these states in all their generality, then discuss their applications in two specific cases relevant for optics: principal states and particlelike states (see Secs. V.C.1 and V.C.2). The eigenstates $\mathbf{q}_i$ of $\mathbf{Q}$ are defined as $\mathbf{Q}\mathbf{q}_i = q_i\mathbf{q}_i$, and they are associated with a well-defined scattering time delay q_i (also called proper delay time), which measures the time accumulated between entering and exiting the scattering region. When the scattering matrix $\mathbf{S}$ of a problem is unitary, the associated time-delay operator $\mathbf{Q}$ is Hermitian, such that the proper delay times are real and the time-delay eigenstates $\mathbf{q}_i$ form a complete and orthogonal set at the input to the scattering region.

The question we address is, which practical consequences can be associated with these definitions and how such states can be determined and generated experimentally. Generally speaking, a wave that enters a disordered slab will have components that exit the slab rather quickly, while other components will stay inside the slab for longer (as discussed in Sec. IV.A.2). This is different when injecting a state defined by the time-delay coefficient vector $\mathbf{q}_i$ into the slab (e.g., through an SLM), since this state is characterized by just a single and well-defined time, i.e., its associated proper delay time q_i. This feature leads to advantageous properties related to the fact that a well-defined time delay can be linked to a suppression of frequency dispersion and to a strong collimation of ballistic scattering states.

1. Principal modes in a fiber

Consider a MMF which transmits light almost perfectly, i.e., it has very little reflection and absorption. In this case the transmission matrix $\mathbf{t}$ associated with this fiber is close to unitary such that all the transmission eigenvalues τ_n are near unity. Correspondingly, the associated transmission eigenchannels studied in Sec. II.B will not be in any way special, since the massive degeneracy in the linear subspace associated with $\tau \approx 1$ will mix all these channels indiscriminately. The question thus arises whether this degeneracy can be lifted by a clever choice for a different basis that has advantageous properties, e.g., for the transfer of information through the fiber. One might think that such a suitable basis is given by the fiber modes themselves, as determined by the boundary conditions in the fiber cross section. In particular, since the different transverse mode profiles also result in mode-specific longitudinal velocities it is tempting to think that the fiber modes are the suitable modes for avoiding dispersion in the fiber. It turns out, however, that this is generally not the case and that such a dispersion-free basis is rather given through the eigenbasis of the time-delay operator (Poole and Wagner, 1986; Fan and Kahn, 2005).

Specifically, consider an input coefficient vector $\mathbf{v}$, which is transmitted by the fiber to an output vector $\mathbf{u} = \mathbf{t}\mathbf{v}$, where we assume the vectors and the matrix to be given in the mode basis (polarization degrees of freedom will be neglected). If we now demand that the transverse profile at the fiber output should be dispersion free this means that the output vector $\mathbf{u}$ should not change, when changing the input frequency ω slightly while keeping the input vector $\mathbf{v}$ the same (Fan and Kahn, 2005). To be more specific, we demand that the orientation of the output vector $\mathbf{u}$ stays invariant (which is equivalent to demanding that the output field distribution stays unchanged up to a prefactor). Decomposing $\mathbf{u}$ into an amplitude and the corresponding unit vector which contains this orientation $\mathbf{u} = u\hat{\mathbf{u}}$, we obtain the following:

$$\frac{d\mathbf{u}}{d\omega} = \frac{du}{d\omega}\hat{\mathbf{u}} + u\frac{d\hat{\mathbf{u}}}{d\omega} = \frac{du}{d\omega}u^{-1}\mathbf{t}\mathbf{v} + u\frac{d\hat{\mathbf{u}}}{d\omega} \equiv \frac{d\mathbf{t}}{d\omega}\mathbf{v}. \tag{55}$$

Requiring that $\hat{\mathbf{u}}$ is dispersion free, $d\hat{\mathbf{u}}/d\omega \equiv 0$, and multiplying from the left with $-i\mathbf{t}^{-1}$, we end up with the following:

$$-i\mathbf{t}^{-1}\frac{d\mathbf{t}}{d\omega}\mathbf{v} = -iu^{-1}\frac{du}{d\omega}\mathbf{v}, \tag{56}$$

which tells us that those input states $\mathbf{v}$ that are transmitted without transverse dispersion (to first order) are eigenstates of the matrix $\tilde{\mathbf{Q}} = -i\mathbf{t}^{-1}d\mathbf{t}/d\omega$. For unitary transmission matrices, for which $\mathbf{t}^{-1} = \mathbf{t}^{\dagger}$, this expression for $\tilde{\mathbf{Q}}$ is perfectly equivalent to the expression for the Wigner-Smith time-delay operator $\mathbf{Q}$ that we had found before; see Eq. (48). For nonunitary transmission matrices as for fibers with finite reflection or loss, one can further modify the right-hand side of Eq. (56) [using $u = |u|\exp(i\phi)$] to find the following for the corresponding eigenvalue of this new operator:

$$q = -i\frac{d\ln|\mathbf{t}v|}{d\omega} + \frac{d\arg(\mathbf{t}v)}{d\omega}. \tag{57}$$

The first term on the right-hand side of Eq. (57) is a measure for the losses due to reflection or outcoupling that depends only on the norm of the output; the second term is the

derivative of the scattering phase at the output, i.e., the time delay.

Because of their superior properties, the modes associated with the eigenvectors of $\tilde{\mathbf{Q}}$ have been termed principal modes (Fan and Kahn, 2005). Note in this context, that for a perfectly straight fiber without mode coupling, the PMs and the fiber modes become the same (in the absence of degeneracies). In this sense, the advantages of the PMs assert themselves fully in the presence of a finite crosstalk between the ideal fiber modes (Ho and Kahn, 2014). First observations of PMs in MMFs were reported by Carpenter, Eggleton, and Schroder (2014a, 2015) and Xiong *et al.* (2016). In Fig. 32(a) we show data from a measurement on fibers with a weak mode coupling, which demonstrates the increased stability of PMs as compared to conventional LP fiber modes. Whereas PMs already feature by design a frequency stability to first order, the weak coupling of modes enhances their stability further. In the regime of strong mode coupling the frequency stability of PMs is reduced, but still far superior compared to arbitrary input configurations [see Fig. 32(b)]. The same can be expected for a disordered slab geometry, for which PMs can also be constructed, but for which case no experiments have been reported so far. We see in the following that another class of time-delay eigenstates can also be found in ballistic or quasiballistic scattering structures with a frequency robustness that goes beyond the first-order stability.

2. Particlelike scattering states

Consider the simple case of a resonator geometry, which, for reasons of simplicity, is assumed to be just two dimensional. The scalar waves, which are injected through a waveguide on the left, can be reflected through the same waveguide or transmitted through a second waveguide attached on the right (see Fig. 33). One can now try to steer waves through the resonator such that they will follow the path of a classical trajectory throughout the entire scattering process rather than being diffractively scattered. To select the "geometric optics" states from the full set of scattering states that "wave optics" will produce in this setup, we further assume that only the scattering matrix $\mathbf{S}$ of the system is available (but no information on its interior scattering landscape). The presence of such ballistic scattering states leads to nonuniversal contributions to the distribution of transmission eigenvalues $P(\tau)$ at the values $\tau \approx 0$ and $\tau \approx 1$, corresponding to fully closed and open transmission channels, respectively. As discussed in Sec. II.B, it was exactly such system-specific contributions which were responsible for the suppression of electronic shot noise below the universal limit (Agam, Aleiner, and Larkin, 2000; Jacquod and Sukhorukov, 2004; Aigner, Rotter, and Burgdörfer, 2005; Sukhorukov and Bulashenko, 2005), which itself was already reduced below the Poissonian limit by Schottky (1918) (Beenakker and Schönenberger, 2003).

In analogy to the situation found for the MMF in Sec. V.C.1, all the fully transmitted (reflected) waves are completely mixed in the degenerate subspace corresponding to $\tau \approx 1$ ($\tau \approx 0$). Correspondingly, exciting transmission or reflection eigenchannels will not yield states that follow individual classical bouncing patterns in the system, but several of them simultaneously; see Fig. 33(a). To unmix these contributions one can now make use of the Wigner-Smith time-delay operator $\mathbf{Q} = -i\mathbf{S}^{\dagger}\partial\mathbf{S}/\partial\omega$ introduced in Sec. II.C; this is because its eigenvalues, i.e., the proper delay times allow one to sort all the different ballistic scattering

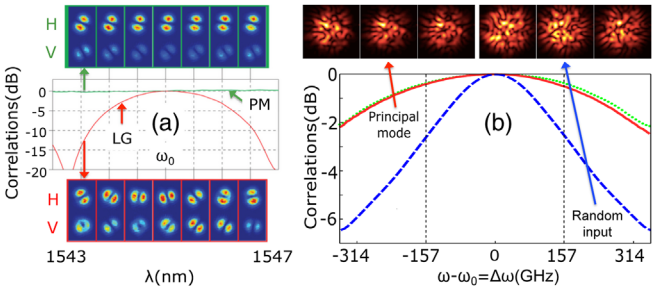

FIG. 32. Experimental data on principal modes (PMs) in fibers with (a) weak and (b) strong mode mixing. In both figures the main panel shows the spectral correlation of the output field pattern measured relative to the center frequency for a PM as compared to a Laguerre-Gaussian (LG) mode in (a) and as compared to a random superposition of LP modes in (b). In both cases the PM features a considerably increased stability of the field configuration at the fiber output. This output is shown in the color images: (a) Top: PM, bottom: LG mode. Horizontal (H) and veritcal (V) polarization directions are shown separately. (b) Top left: PM, top right: random input. Images recorded at $\Delta\omega = -157$, 0, and 157 GHz (from left to right). The dashed green line in (b) shows the calculated correlation function based on the experimentally obtained fiber transmission matrix, which is in excellent agreement with the experimentally determined correlation function (red). (a) Adapted from Carpenter, Eggleton, and Schröder, 2015. (b) Adapted from Xiong *et al.*, 2016.

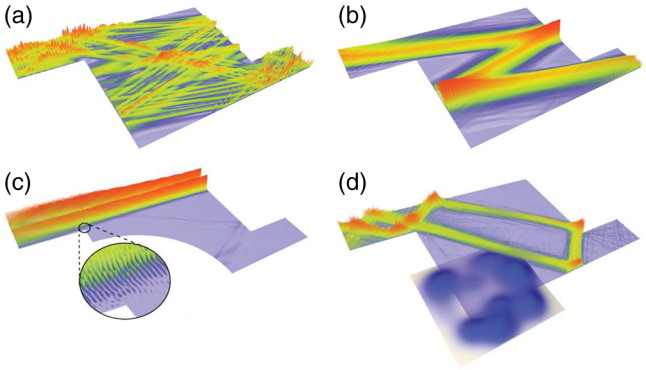

FIG. 33. (a) Wave intensity of a transmission eigenchannel with transmission close to unity in scattering through a resonator with two waveguides attached on the left and right (the flux is incoming from the left). Whereas transmission eigenchannels typically lead to highly complex interference patterns inside the resonator (as in wave optics), the particlelike states shown in (b)–(d) follow a classical bouncing pattern throughout the entire scattering process (as in geometric optics). (b) Transmitted particlelike state in a clean rectangular resonator. (c), (d) Reflected particlelike states in a geometry of the same dimensions as in (a), (b), from which, however, a quarter-circular piece was removed in (c) and a smooth and weak disorder potential was added in (d) (see bottom part of this panel). Adapted from Rotter, Ambichl, and Libisch, 2011.

contributions by way of their different time delays (Rotter, Ambichl, and Libisch, 2011). Specifically, one determines those eigenstates $\mathbf{q}$ of $\mathbf{Q}$ that have incoming components only in the left waveguide, i.e., $\mathbf{q} = (\mathbf{q}_l, \mathbf{0})^{\mathrm{T}}$. Writing the time-delay operator with its four sub-blocks [in correspondence to the subdivision of the scattering matrix itself, see Eq. (15)], one finally obtains the following eigenvalue problem:

$$\begin{pmatrix} \mathbf{Q}_{11} & \mathbf{Q}_{12} \\ \mathbf{Q}_{21} & \mathbf{Q}_{22} \end{pmatrix} \begin{pmatrix} \mathbf{q}_l \\ \mathbf{0} \end{pmatrix} = \begin{pmatrix} \mathbf{Q}_{11}\mathbf{q}_l \\ \mathbf{Q}_{21}\mathbf{q}_l \end{pmatrix} = q \begin{pmatrix} \mathbf{q}_l \\ \mathbf{0} \end{pmatrix}. \tag{58}$$

From the last equality the following two conditions can be deduced: (i) $\mathbf{Q}_{11}\mathbf{q}_l = q\mathbf{q}_l$ and (ii) $\mathbf{Q}_{21}\mathbf{q}_l = \vec{0}$. Since $\mathbf{Q}_{11}$ is a Hermitian matrix ($\mathbf{Q}_{12}$ and $\mathbf{Q}_{21}$ are not), condition (i) yields an orthogonal and complete set of eigenstates in the incoming waveguide. Out of this set of states, those which, according to condition (ii), lie in the null space (kernel) of $\mathbf{Q}_{21}$ are the desired time-delay eigenstates with a well-defined input port. One can show (Rotter, Ambichl, and Libisch, 2011) that both conditions can be fulfilled only by waves which are either fully transmitted or reflected; in other words these states are simultaneously eigenstates of $\mathbf{Q}$ and of $\mathbf{t}^\dagger\mathbf{t}$ with deterministic transmission eigenvalues τ close to 0 or 1. Practically, the degree to which condition (ii) is fulfilled can be evaluated by a measure $\chi = \|\mathbf{Q}_{21}\mathbf{q}_l\|$ which should be the closer to 0 the better condition (ii) is fulfilled. This measure can thus be conveniently used for assessing how well a given state will be able to follow a classical bouncing pattern. Typically those states with a small value of χ are also those with a small time-delay eigenvalue q, in agreement with the expectation that only states which stay inside the scattering region for a time shorter than the Ehrenfest time $q < \tau_E$ will be able to behave particlelike (Agam, Aleiner, and Larkin, 2000). In Figs. 33(b)–33(d) three examples of states are shown that feature very small values of χ for different resonator geometries. It can be seen how these states tend to follow a (short) ray from geometric optics that avoids any diffractive scattering throughout its propagation (as at the sharp corners of the input and output facets). The first experimental demonstration of particlelike scattering states and corresponding wave packets was reported based on acoustic wave scattering in a metal plate studied by laser interferometry (Gérardin *et al.*, 2016).

When comparing these particlelike states to the PMs from Sec. V.C.1, the following comments can be made: PMs can be constructed for arbitrary scattering media (including strongly disordered samples) and their frequency stability to first order will be assured in all of these systems by construction. Particlelike states, on the other hand, can be found only in systems where waves can propagate along sufficiently stable ballistic scattering pathways. Because of their collimation on these pathways, particlelike states feature, in turn, a much higher frequency stability than principle modes (in a similar way as geometric optics states are frequency independent by default). Both sets of states have advantageous properties for communication purposes, like the dispersion-free transmission as well as the high directionality of the particlelike states that seems well suited for steering a signal to a well-defined target. In Sec. V.D.1 we also see that the time-delay eigenstates optimally avoid or enhance the effect of dissipation in a medium.

D. Wave front shaping in media with gain or loss

In this section we discuss the application of wave front shaping techniques in systems with gain or loss, with a focus on disordered media.

1. Absorbing media

Consider the case of an absorbing disordered medium, which, for simplicity, we assume to be uniformly absorbing (i.e., the absorption rate is independent of the spatial position in the medium). For this situation we know from our analysis in Sec. II.C that the absorption is directly proportional to the time spent inside the absorbing medium. Since, in turn, the time associated with a stationary scattering state can be measured through the dwell-time operator $\mathbf{Q}_d$, minimal or maximal absorption of waves in a medium can be achieved by injecting those eigenvectors of $\mathbf{Q}_d$, which are associated with the smallest or largest eigenvalue, respectively. (We recall here the result from Sec. II.C that in the limit of vanishing absorption the dwell-time operator $\mathbf{Q}_d$ and the time-delay operator $\mathbf{Q}$ coincide up to mostly negligible self-interference terms.) The procedure to obtain the states with minimal absorption is thus equivalent to the approach presented in Sec. V.C.2 for the generation of particlelike scattering states, which are associated with the smallest values of the time delay. The states with maximal absorption were explicitly studied by Chong and Stone (2011), where it was shown how in a weakly scattering medium a suitably chosen input wave front can increase the degree of absorption from a few percent to more than 99%. Such a coherent enhancement of absorption (CEA) can, in principle, be realized at any frequency for which the input wave is shaped appropriately.

An interesting point to observe here is that in the theoretical approach put forward by Chong and Stone (2011) these maximally absorbed states were not identified through the help of the dwell-time operator, but rather as those states which are minimally reflected from an absorbing disordered medium. In the considered single-port systems, where the reflection matrix is equivalent to the scattering matrix, we know, however, from Eq. (51) that the dwell-time operator is equivalent to the unitary deficit of the scattering matrix such that these two different concepts to evaluate maximum absorption perfectly coincide. Chong and Stone (2011) extended the analysis to the case of a spatially localized absorber buried behind a layer of lossless scattering medium—a situation that was also studied experimentally by Vellekoop *et al.* (2008) in an attempt to focus light on a small fluorescent nanoscopic bead inside a disordered medium to increase the fluorescence. In this case the degree of optimal absorption was found to be more strongly bounded as compared to the case where the entire medium is absorbing. Further work also shows how the long-range spectral correlations inherent in the transmission and reflection matrices can help to achieve enhanced absorption in a broadband frequency range (Hsu *et al.*, 2015). The first experimental realization of a variant of CEA was reported by Liew *et al.* (2016).

In another numerical study the effect of absorption was investigated in scattering systems with more than one port, like a 2D disordered waveguide connected to two perfect leads on the left and right (Liew, Popoff *et al.*, 2014). In such systems both the maximally transmitted and the minimally reflected channels were studied. For weak absorption these two types of channels were found to be dominated by diffusive transport and to be equivalent (as following from the connection between the transmission and reflection matrices in unitary systems, see Sec. II.A.4). For increasing absorption, however, the behavior of these two different channels decouples, as the reflection can then be minimized not only by increased transmission, but also by enhanced absorption: at a given absorption strength, the maximum transmission channel was found to display a sharp transition to a quasiballistic transport regime. This transition does not occur for the minimal reflection channel, which gets increasingly dominated by the absorption when the absorption strength is increased. An interesting aspect that was also found in this context is that the shape of the transmission and reflection eigenvalue distributions in disordered and dissipative media depends on the confinement geometry (Yamilov *et al.*, 2016)—a fact that may be used for controlling this distribution at will.

Whereas the concepts relating to CEA can be implemented at any input frequency, Chong *et al.* (2010) showed that at well-defined frequencies and at a carefully chosen amount of dissipation, certain incoming channels of light can be fully absorbed. Such a coherent perfect absorber (CPA) of light corresponds to the multimode generalization of a critically coupled oscillator, with the difference that at least two input beams are required, which have to have the correct amplitude and phase to interfere appropriately. As a result, the relative phase between the input beams can be used to sensitively tune the degree of absorption as was done in the first CPA experiment (Wan *et al.*, 2011). From a conceptual point of view a CPA is a time-reversed laser, in the sense that a gain medium at its first lasing threshold will emit coherent radiation at a well-defined frequency and with a well-defined phase relationship, e.g., between beams emitted on either side of the laser. The time-reversed process corresponds to an absorbing medium which perfectly absorbs the coherent illumination which impinges on it. If one considers a simple 1D edge-emitting laser that emits to the left and right, the coherently absorbed light field of the corresponding CPA features two beams (incoming from the left and right), which share a specific phase relationship to each other. At the points where this phase relationship is satisfied, maximal absorption occurs. It is interesting that, prior to these theoretical and experimental developments, a seminal experiment in the field of plasmonics showed extraordinary absorption for a gold grating under specific incident illumination (Hutley and Maystre, 1976), which was explained using a similar reasoning.

The concept of a CPA can also be extended to other systems (Noh *et al.*, 2012; Zanotto *et al.*, 2014), to 2D or 3D as well as to disordered media. In the latter case the CPA would be the time reverse of a random laser, corresponding to an absorbing random medium, which absorbs incoming waves that have exactly the same complex wave front as the emission profile of the random laser. To generate such a complex wave pattern one would of course have to resort to wave front shaping techniques using SLMs or equivalent tools.

Generally speaking, the theoretical concept behind CPAs builds on the analytical properties of the scattering matrix $\mathbf{S}(\omega)$ (see Sec. II.A.4). In the absence of loss or gain, this matrix is unitary and features poles (zeros) at complex frequencies with negative (positive) imaginary parts located in the complex plane as mirror-symmetric pairs with respect to the real axis. When adding gain to the system the poles and zeros move upwards in the complex plane until the point where the first pole reaches the real axis and lasing sets in. Alternatively, when adding loss to the system, the poles and zeros move downwards until the first zero hits the real axis, at which point coherent perfect absorption can be realized (Chong *et al.*, 2010). Adding even more loss drags additional zeros across the real axis, creating a CPA at each new intersection. Subsequent work also demonstrated how a laser and a CPA can be combined in a single device (Longhi, 2010; Chong, Ge, and Stone, 2011). Such a laser absorber (or CPA laser) can be realized based on the concept of $\mathcal{PT}$-symmetric optical systems (Bender and Boettcher, 1998; El-Ganainy *et al.*, 2007; Makris *et al.*, 2008; Rüter *et al.*, 2010) in which gain and loss are carefully balanced and poles and zeros of the scattering matrix can be brought to meet on the real axis. Realizing such concepts in the optical experiments is challenging as the CPA-lasing points at the pole-zero crossing are affected by the noise due to amplified spontaneous emission. The first realization of a CPA with a $\mathcal{PT}$-phase transition has been reported with a pair of coupled resonators coupled to a microwave transmission line (Sun *et al.*, 2014), followed by the first successful demonstration of lasing and antilasing in the same $\mathcal{PT}$-symmetric device (Wong *et al.*, 2016).

2. Amplifying media

In the previous section we discussed how waves that are injected into a certain disordered medium with absorption can be shaped such as to be maximally or minimally absorbed. Such an approach can, of course, also be considered with an amplifying medium, where one is naturally concerned with maximal or minimal amplification. Work in this direction has dealt with the nontrivial transient dynamics in photonic waveguide structures composed of a combination of materials with both loss and gain. Contrary to conventional expectation, specific initial conditions for the incoming wave can lead to power amplification by several orders of magnitude even if the waveguide is, on average, lossy (Makris, Ge, and Türeci, 2014). Systems with gain and loss have also been proposed for the realization of a special family of waves that have the curious property of featuring a constant intensity in the presence of a nonhomogeneous scattering landscape (Makris *et al.*, 2015)—a feature that cannot be realized with Hermitian scattering potentials. Extending this concept allows one to achieve perfect transmission even through strongly scattering disorder (Makris *et al.*, 2016). A realization of these curious wave solutions requires a careful shaping of the incoming wave front and of the medium's gain-loss profile.

As a medium with a sufficient amount of gain can emit coherent radiation on its own when crossing the laser threshold, work on amplifying media has also always had a strong

focus on engineering the gain for a desired lasing action. In principle, optimizing the gain profile for a medium is a well-studied problem. Consider here the case of a distributed feedback laser in which a so-called "gain grating," consisting of a periodic arrangement of purely amplifying components, can efficiently pump lasing modes with the same periodicity as the grating (Carroll, Whiteaway, and Plumb, 1998). Whereas these concepts for quasi-1D laser structures (like ridge or ring lasers) have meanwhile reached the level of industrial applications, more advanced concepts on lasers with a quasi-2D (planar) geometry have been explored recently. Here the main focus was on reducing the laser threshold of specific modes by increasing the spatial overlap between these selected modes and an externally applied pump profile. Practical implementations of this concept include, e.g., electrically pumped devices for which the electrodes were patterned appropriately (Fukushima *et al.*, 2002; Kneissl *et al.*, 2004; Shinohara *et al.*, 2010). All of these implementations require, however, prior knowledge of the spatial pattern of the selected mode.

With the availability of wave front shaping tools, the pump profile as exerted on an optically pumped laser can, however, be tuned in a manner which is flexible enough to select a given mode based on a simple feedback loop. This feedback can be set up between the pump profile (as determined by the pixel configuration in an SLM) and the light spectrum of the laser pumped with this profile. Combining the feedback with an optimization algorithm has been suggested as a means to make the multimode emission spectrum of a random laser single moded (Bachelard *et al.*, 2012). In an experimental realization, realized shortly after the theoretical proposal (Bachelard *et al.*, 2014) a mode-specific pump selection and a corresponding single-mode operation could be successfully demonstrated for the challenging case of a weakly scattering random laser (see Fig. 34). For such a system no *a priori* knowledge of the lasing mode is available and finding the appropriate pump grating is thus only possible through optimization. As in this case the laser modes are also strongly overlapping both spectrally and spatially, the pump profiles obtained as a result of the optimization process do not just follow the intensity of the laser modes, but instead display a highly complex pattern only remotely related to the mode profiles. The connection between the pump profiles and the modes they select was elucidated in subsequent theoretical work (Bachelard, 2014; Cerjan *et al.*, 2016) based on a non-Hermitian perturbation theory analysis. Alternatively, a mode-selection approach was proposed based on insights from gain saturation of interacting laser modes (Ge, 2015).

A remarkable feature of the feedback-based pump optimization is its flexibility in terms of the optimization goals that it can be employed for. Specifically, it has been proposed that not only the multimode spectrum of a random laser can be "tamed" with it, but also its highly irregular emission profile; see Fig. 34(a) (right panel) (Hisch *et al.*, 2013). A corresponding pump-shaping strategy for tuning the emission profile of a laser has meanwhile been successfully implemented for microcavity lasers (Liew, Redding *et al.*, 2014) [for random lasers a collimated output beam was achieved with other means (Schönhuber *et al.*, 2016)]. A next step could be to use the spatial control of the applied pump to enhance the power efficiency of lasers (Ge, Malik, and Türeci, 2014).

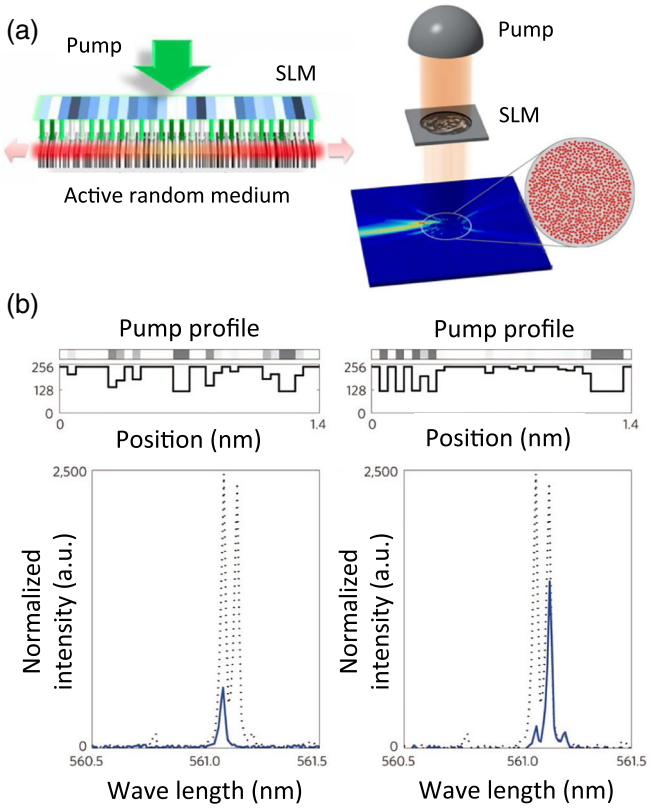

FIG. 34. (a) (Left) Schematic to control the emission spectrum of a random laser consisting of a quasi-one-dimensional sequence of different dielectric layers. Tuning the incident pump beam through the spatial light modulator allows here to change how many lasing modes are active and at which frequencies they emit. (Right) A corresponding setup proposed to control the directionality of the emission. (b) The spectral control of a random laser [left panel in (a)] was realized in an experiment using optofluidic random lasers, where the laser emitted in two modes for uniform pumping (see dotted lines in lower panels). By shaping the pump profile as shown in the top panel, single-mode emission through either one of these two modes was achieved (see solid lines in lower panels). (a) (Left panel) Adapted from Bachelard *et al.*, 2012. (a) (Right panel) Adapted from Hisch *et al.*, 2013. (b) Adapted from Bachelard *et al.*, 2014.

VI. CONCLUSIONS AND OUTLOOK

Wave front shaping techniques will become faster, more accurate, and will involve an increasing number of controlled pixels. Loosely speaking, this development can be connected to the exponential increase in efficiency of computer hardware (known as Moore's law). With this projection in mind, one can foresee that experiments using light modulation technology will soon be able to do much more than they can already do today. In this last section a few ideas are provided on where the further technological developments could take us or on what we believe could be promising research topics in the next few years.

A. Wave front shaping for unraveling mesoscopic phenomena

Whereas our review highlighted quite a few mesoscopic effects that were brought to light with wave front shaping tools, we believe that many more fundamental phenomena can still be explored with this new technology. Prominent examples could be an unambiguous proof for Anderson localization in a three-dimensional medium (Lagendijk, Tiggelen, and Wiersma, 2009; Maret *et al.*, 2013; Scheffold and Wiersma, 2013; Segev, Silberberg, and Christodoulides, 2013; Sperling *et al.*, 2013; Skipetrov and Sokolov, 2014) or the direct experimental demonstration of the bimodal distribution of transmission eigenvalues in optical scattering through a disordered medium [for which several indications have already been put forward (Vellekoop and Mosk, 2008b; Goetschy and Stone, 2013; Popoff *et al.*, 2014)]. In this context it would also be of great interest to directly inject the fully open transmission eigenchannels and to observe their superior transmission characteristics, in a similar way to what was done in acoustics (Gérardin *et al.*, 2014). Likewise, one could try to directly observe the propagation of time-delay eigenstates [such as principal modes (Fan and Kahn, 2005) or particlelike states (Rotter, Ambichl, and Libisch, 2011)] through a weakly or strongly disordered optical medium, similar to what was recently achieved in optical fibers (Carpenter, Eggleton, and Schröder, 2015; Xiong *et al.*, 2016) and in acoustic waveguides (Gérardin *et al.*, 2016). An experimental demonstration that also still remains to be done is that of a multichannel coherent perfect absorber (Chong *et al.*, 2010), which could go as far as to demonstrate the time-reverse process of random lasing. Also other exotic effects, like "rogue waves" (Solli *et al.*, 2007; C. Liu *et al.*, 2015) or "branched flow" (Topinka *et al.*, 2001; Metzger, Fleischmann, and Geisel, 2010), that have also been studied in the context of ocean acoustics, could now be enhanced and tuned in various ways through wave front shaping. Optical scattering of course also brings in many new aspects as compared to its electronic counterpart, in particular, through nonlinearities (Wellens and Grémaud, 2008; Bortolozzo, Residori, and Sebbah, 2011) and the breaking of reciprocity (Muskens *et al.*, 2012; Peng *et al.*, 2014), which have not yet been fully explored with wave front shaping tools.

B. New systems

We saw that mesoscopic physics theory and experiments have mostly been focused on a handful of canonical systems in electronics: the disordered wire, the quantum billiard, the quantum point contact, etc. In the optical domain, a large fraction of the theoretical and experimental work was focused on scattering in three-dimensional bulk disorder and restricted to a few geometries as well. Here we comment on the opportunities of new optical systems to be studied with the mesoscopic physics concepts already developed.

Two systems were discussed extensively already in Secs. IV and V: biological tissues and multimode fibers. We tried to highlight their specific features in terms of scattering and in which way these can be appropriately described by adapting the existing mescoscopic physics concepts. We also tried to highlight how these system-specific aspects could lead to new opportunities, e.g., for imaging (see here the discussion on the memory effect in Secs. II and V). Plasmonic systems are also an interesting playground to study the effect of disorder and wave front shaping, in particular, due to the capability of the metal to localize light well below the diffraction limit. This includes not only metallic hole arrays with disorder (Gjonaj *et al.*, 2011, 2013; Seo *et al.*, 2014), but also metal-dielectric fractal structures (Bondareff, Gigan, and Grésillon, 2015; Gaio *et al.*, 2015).

New optical systems are meanwhile emerging due to the exciting possibility in photonics to tailor the propagation medium, e.g., to vary the amount of order and disorder, or to change the dimensionality of the problem. Light transport has been studied in 1D stacks (Bertolotti *et al.*, 2005), 1D waveguides (Topolancik, Vollmer, and Ilic, 2007; Sapienza *et al.*, 2010), and 2D disordered structures (Riboli *et al.*, 2011; García *et al.*, 2012). A whole community works on photonic crystals, trying to obtain perfectly regular structures, but the very small amount of residual disorder has been known to strongly affect transport within these structures. Careful engineering of the amount of disorder can, in turn, allow one to control the transport properties of the system (Topolancik, Vollmer, and Ilic, 2007; García *et al.*, 2013). In 3D, self-organization allows the fabrication of near-perfect 3D photonic crystals (Galisteo-Lopez *et al.*, 2011), for which the amount of disorder and its effect on the transport properties of light can again be controlled. Another potential revolution was initiated by the possibility of engraving on a medium a completely designed refractive index distribution via direct laser writing (Kawata *et al.*, 2001; Deubel *et al.*, 2004), which meanwhile allows one to create new kinds of disorder, such as hyperuniform structures (Florescu, Torquato, and Steinhardt, 2009; Haberko, Muller, and Scheffold, 2013; Muller *et al.*, 2014; Froufe-Pérez *et al.*, 2016). Finally, we also mention optically reconfigurable structures where a refractive index distribution is engraved from an intensity pattern, such as photorefractive crystals (Schwartz *et al.*, 2007; Levi *et al.*, 2011), an optical valve (Bortolozzo, Residori, and Sebbah, 2011), or integrated silicon-on-insulator multimode interference devices (Bruck *et al.*, 2015, 2016). These structures are promising platforms on which not only the wave front but also the disorder can be controlled using a spatial light modulator.

C. Applications of mesoscopic concepts in optics

A field where wave front shaping concepts have already had a large impact is the field of optical imaging in turbid tissues (see also Sec. IV). Several proof-of-concept experiments have shown that the conventional paradigm of ballistic imaging could be extended to the deep multiple scattering regime (see Sec. IV.C.2). While the multiscale nature and variability of these media makes them difficult to model, they are also a challenge for wave front shaping due to a potentially very short decorrelation time, inhomogeneous absorption, and due to the fact that one typically has access to one side of them only. In this respect, the exploitation of the memory effect (see Sec. V.A) has already overcome this limitation, by providing an order of magnitude increase in speed for scanning a point (Tang, Germain, and Cui, 2012) or even for single shot

imaging (Katz, Small, Guan, and Silberberg, 2014). Other mesoscopic concepts, such as coherent perfect absorption or the generation of time-delay eigenstates (see Secs. V.C and V.D), could be exploited in the future for further improvement of imaging or light delivery, e.g., to avoid or to address regions in a tissue that are absorbing or where movements induce decorrelations. Because of the enormous complexity involved, calculating the transmission matrix of a medium from the characterization of its three-dimensional shape, or worse, recovering the shape of a medium from its transmission matrix, currently remains out of reach for disordered systems. Only in very simple cases can such demanding tasks be achieved, such as in short straight multimode fibers (Plöschner, Tyc, and Čižmár, 2015).

The perspective of better controlling the transmission through a medium has tremendous potential in communication technology, not only in optics but also in the radio-frequency domain, where increased transmission and bandwidth could be realized as well as more secure and well-isolated channels (Kaina *et al.*, 2014). In this context, the direct access to open channels or time-delay eigenstates would be particularly useful (see Sec. V).

Wave front shaping has also moved MMFs into the focus of attention, both for imaging and for telecommunication purposes. Imaging through an MMF is meanwhile a direct competitor to the bulkier fiber bundles (Gigan, 2012). In fiber communications, where the spatial degrees of freedom in MMFs are the last ones remaining to be exploited for a higher data rate (Richardson, Fini, and Nelson, 2013), wave front shaping has already opened the possibility to physically decouple the transmission modes, rather than unmixing the transmitted information *a posteriori* using multiple-input multiple-output technology.

Another domain of application is nanophotonics and quantum optics, where complex systems have increasingly been considered as a platform for light matter interaction. In the first step, a modification of the emission properties of isolated single emitters has been discussed and was connected to the local density of states (Birowosuto *et al.*, 2010; Krachmalnicoff *et al.*, 2010; Sapienza *et al.*, 2010, 2011), which in turn can be linked to the modal structure of the medium as described by mesoscopic theory. More recently, the concepts of quantum networks have been studied, where multiple emitters are distributed and connected for quantum computing or simulations (Vedral, Barenco, and Ekert, 1996; Plenio and Huelga, 2008) as well as to understand quantum phenomena in biology such as photosynthesis (Hildner *et al.*, 2013). In a disordered system, the connections between emitters can again be understood through the underlying modal structure and the associated Green's function of the medium (Cazé, Pierrat, and Carminati, 2013). If mesoscopic theory can help to understand and better design such a network, wave front shaping can also be a particularly useful tool to interrogate such a system for computation or simulation. Even a linearly disordered system can be interesting in the context of quantum random walks of single or multiple photons (Ott, Mortensen, and Lodahl, 2010; Defienne *et al.*, 2014, 2016; Goorden *et al.*, 2014; Huisman *et al.*, 2014; Wolterink *et al.*, 2016). Mesoscopic effects such as Anderson localization have been studied with nonclassical states in waveguide arrays (Schreiber *et al.*, 2011; Crespi *et al.*, 2013) and it would be interesting to study these effects in genuine disordered systems. Again, wave front shaping could serve here as an indispensable ingredient to make these systems useful for applications.

Finally, we mention the following proofs of concept that have already been given for new devices, be it for compact spectrometers (Redding *et al.*, 2013), ultrafast switches (Strudley *et al.*, 2014), tunable random lasers (Hisch *et al.*, 2013; Bachelard *et al.*, 2014), or light harvesting (Vynck *et al.*, 2012; Riboli *et al.*, 2014). We expect this list to be significantly extended in the near future.

ACKNOWLEDGMENTS

We thank all members of the community that were kind enough to share the rights to reprint their figures and the following colleagues for very fruitful discussions: Philipp Ambichl, Alexandre Aubry, Nicolas Bachelard, Hui Cao, Rémi Carminati, Adrian Girschik, Michel Gross, Thomas Hisch, Ori Katz, Florian Libisch, Matthias Liertzer, Stefan Nagele, Renate Pazourek, Romain Pierrat, and Patrick Sebbah. S. R. gratefully acknowledges the generous support of Institut Langevin and Ecole Normale Supérieure through invited professor positions, during which part of this review was written. The authors' own research presented in this review was supported by the Austrian Science Fund (FWF) Projects No. SFB-ADLIS F16, No. P17359, No. SFB-IR-ON F25, No. SFB-NextLite F49, and No. I1142-N27 (GePartWave); the Vienna Science Fund (WWTF) Project No. MA09-030 (LICOTOLI); and the European Research Council (ERC) Grant No. 278025.

REFERENCES

Abrahams, E., 2010, *50 Years of Anderson Localization* (World Scientific, Singapore).

Abrahams, E., P. W. Anderson, D. C. Licciardello, and T. V. Ramakrishnan, 1979, Phys. Rev. Lett. **42**, 673.

Agam, O., I. Aleiner, and A. Larkin, 2000, Phys. Rev. Lett. **85**, 3153.

Aigner, F., S. Rotter, and J. Burgdörfer, 2005, Phys. Rev. Lett. **94**, 216801.

Akbulut, D., T. J. Huisman, E. G. van Putten, W. L. Vos, and A. P. Mosk, 2011, Opt. Express **19**, 4017.

Akbulut, D., T. Strudley, J. Bertolotti, E. P. A. M. Bakkers, A. Lagendijk, O. L. Muskens, W. L. Vos, and A. P. Mosk, 2016, Phys. Rev. A **94**, 043817.

Akemann, G., J. Baik, and P. D. Francesco, 2011, *The Oxford Handbook of Random Matrix Theory* (Oxford University Press, New York).

Akkermans, E., and R. Maynard, 1985, J. Phys. Lett. **46**, 1045.

Akkermans, E., and G. Montambaux, 2007, *Mesoscopic Physics of Electrons and Photons* (Cambridge University Press, Cambridge, England).

Akkermans, E., P. E. Wolf, and R. Maynard, 1986, Phys. Rev. Lett. **56**, 1471.

Albada, M. P. V., and A. Lagendijk, 1985, Phys. Rev. Lett. **55**, 2692.

Alhassid, Y., 2000, Rev. Mod. Phys. **72**, 895.

Altland, A., 1991, Z. Phys. B **82**, 105.

Altshuler, B. L., 1985, JETP Lett. **41**, 648 [http://www.jetpletters.ac.ru/ps/1470/article_22425.shtml].

Ambichl, P., 2012, Delay times and beam-like scattering states in coherent wave transmission through resonators, diploma thesisTech. Rep. [Vienna University of Technology (TU Wien), Vienna, Austria].
Amitonova, L. V., A. P. Mosk, and P. W. H. Pinkse, 2015, Opt. Express **23**, 20569.
Anderson, P. W., 1958, Phys. Rev. **109**, 1492.
Anderson, P. W., E. Abrahams, and T. V. Ramakrishnan, 1979, Phys. Rev. Lett. **43**, 718.
Andreoli, D., G. Volpe, S. Popoff, O. Katz, S. Gresillon, and S. Gigan, 2015, Sci. Rep. **5**, 10347.
Arendt, W., and W. Schleich, 2009, *Mathematical analysis of evolution, information, and complexity* (Wiley-VCH, Weinheim).
Aubry, A., L. Cobus, S. Skipetrov, B. van Tiggelen, A. Derode, and J. Page, 2014, Phys. Rev. Lett. **112**, 043903.
Aubry, A., and A. Derode, 2009, Phys. Rev. Lett. **102**, 084301.
Aulbach, J., B. Gjonaj, P. M. Johnson, A. P. Mosk, and A. Lagendijk, 2011, Phys. Rev. Lett. **106**, 103901.
Babcock, H. W., 1953, Publ. Astron. Soc. Pac. **65**, 229.
Bachelard, N., 2014, Ph.D. thesis (ESPCI, Paris, France).
Bachelard, N., J. Andreasen, S. Gigan, and P. Sebbah, 2012, Phys. Rev. Lett. **109**, 033903.
Bachelard, N., S. Gigan, X. Noblin, and P. Sebbah, 2014, Nat. Phys. **10**, 426.
Balog, S., P. Zakharov, F. Scheffold, and S. E. Skipetrov, 2006, Phys. Rev. Lett. **97**, 103901.
Baranger, H. U., and P. A. Mello, 1994, Phys. Rev. Lett. **73**, 142.
Baranger, H. U., and P. A. Mello, 1995, Phys. Rev. B **51**, 4703.
Beenakker, C., and C. Schönenberger, 2003, Phys. Today **56**, No. 5, 37.
Beenakker, C. W. J., 1994, Mod. Phys. Lett. B **08**, 469.
Beenakker, C. W. J., 1997, Rev. Mod. Phys. **69**, 731.
Beenakker, C. W. J., 2011, in *The Oxford Handbook of Random Matrix Theory*, edited by G. Akemann, J. Baik, and P. Di Francesco (Oxford University Press, Oxford), p. 723.
Beenakker, C. W. J., and M. Büttiker, 1992, Phys. Rev. B **46**, 1889.
Beenakker, C. W. J., and M. Patra, 1999, Mod. Phys. Lett. B **13**, 337.
Beenakker, C. W. J., and B. Rajaei, 1994, Phys. Rev. B **49**, 7499.
Bellanger, C., A. Brignon, J. Colineau, and J. P. Huignard, 2008, Opt. Lett. **33**, 2937.
Bender, C. M., and S. Boettcher, 1998, Phys. Rev. Lett. **80**, 5243.
Berdagué, S., and P. Facq, 1982, Appl. Opt. **21**, 1950.
Bergmann, G., 1983, Phys. Rev. B **28**, 2914.
Berkovits, R., and S. Feng, 1994, Phys. Rep. **238**, 135.
Berkovits, R., and M. Kaveh, 1990, Phys. Rev. B **41**, 2635.
Bertolotti, J., S. Gottardo, D. Wiersma, M. Ghulinyan, and L. Pavesi, 2005, Phys. Rev. Lett. **94**, 113903.
Bertolotti, J., E. G. v. Putten, C. Blum, A. Lagendijk, W. L. Vos, and A. P. Mosk, 2012, Nature (London) **491**, 232.
Bianchi, S., and R. Di Leonardo, 2012, Lab Chip **12**, 635.
Bifano, T., 2011, Nat. Photonics **5**, 21.
Birman, M. S., and D. R. Yafaev, 1992, Algebra i Analiz **4**, 1 [http://mi.mathnet.ru/eng/aa/v4/i6/p1].
Birowosuto, M. D., S. E. Skipetrov, W. L. Vos, and A. P. Mosk, 2010, Phys. Rev. Lett. **105**, 013904.
Bittner, S., B. Dietz, M. Miski-Oglu, P. O. Iriarte, A. Richter, and F. Schäfer, 2009, Phys. Rev. A **80**, 023825.
Blanter, Y., and M. Büttiker, 2000, Phys. Rep. **336**, 1.
Bloom, D., and G. Bjorklund, 1977, Appl. Phys. Lett. **31**, 592.
Blümel, R., and U. Smilansky, 1990, Phys. Rev. Lett. **64**, 241.
Bohigas, O., M. J. Giannoni, and C. Schmit, 1984, Phys. Rev. Lett. **52**, 1.
Bohigas, O., R. U. Haq, and A. Pandey, 1983, *Nuclear Data for Science and Technology*, edited by K. H. Böchhoff (Reidel, Dordrecht), p. 809.
Bondareff, G. V., S. Gigan, and S. Grésillon, 2015, ACS Photonics **2**, 1658.
Boniface, A., M. Mounaix, B. Blochet, R. Piestun, and S. Gigan, 2017, Optica **4**, 54.
Born, M., and E. Wolf, 1999, *Principles of Optics: Electromagnetic Theory of Propagation, Interference and Diffraction of Light* (Cambridge University Press, Cambridge, England).
Bortolozzo, U., S. Residori, and P. Sebbah, 2011, Phys. Rev. Lett. **106**, 103903.
Bossy, E., and S. Gigan, 2016, J. Photoacoust. **4**, 22.
Breit, G., and E. Wigner, 1936, Phys. Rev. **49**, 519.
Bridges, W. B., P. T. Brunner, S. P. Lazzara, T. A. Nussmeier, T. R. OMeara, J. A. Sanguinet, and W. P. Brown, 1974, Appl. Opt. **13**, 291.
Brillouin, L., 1960, *Wave Propagation and Group Velocity* (Academic Press, New York and London).
Brouwer, P. W., 1995, Phys. Rev. B **51**, 16878.
Brouwer, P. W., 1997, Ph.D. thesis, Leiden University.
Brouwer, P. W., 1998, Phys. Rev. B **57**, 10526.
Brouwer, P. W., and C. W. J. Beenakker, 1995, Phys. Rev. B **51**, 7739.
Brouwer, P. W., and K. Frahm, 1996, Phys. Rev. B **53**, 1490.
Brouwer, P. W., K. M. Frahm, and C. W. J. Beenakker, 1997, Phys. Rev. Lett. **78**, 4737.
Bruck, R., B. Mills, B. Troia, D. J. Thomson, F. Y. Gardes, Y. Hu, G. Z. Mashanovich, V. M. N. Passaro, G. T. Reed, and O. L. Muskens, 2015, Nat. Photonics **9**, 54.
Bruck, R., K. Vynck, P. Lalanne, B. Mills, D. J. Thomson, G. Z. Mashanovich, G. T. Reed, and O. L. Muskens, 2016, Optica **3**, 396.
Büttiker, M., 1986, Phys. Rev. Lett. **57**, 1761.
Büttiker, M., 1988, Phys. Rev. B **38**, 9375.
Büttiker, M., 1990, Phys. Rev. Lett. **65**, 2901.
Calvo, H. L., and H. M. Pastawski, 2010, Europhys. Lett. **89**, 60002.
Candes, E. J., and T. Tao, 2006, IEEE Trans. Inf. Theory **52**, 5406.
Caravaca-Aguirre, A. M., E. Niv, D. B. Conkey, and R. Piestun, 2013, Opt. Express **21**, 12881.
Carminati, R., G. Cwilich, L. S. Froufe-Pérez, and J. J. Sáenz, 2015, Phys. Rev. A **91**, 023807.
Carminati, R., R. Pierrat, J. d. Rosny, and M. Fink, 2007, Opt. Lett. **32**, 3107.
Carminati, R., J. J. Saenz, J.-J. Greffet, and M. Nieto-Vesperinas, 2000, Phys. Rev. A **62**, 012712.
Carpenter, J., B. Eggleton, and J. Schroder, 2014a, in *2014 European Conference on Optical Communication (ECOC)* (IEEE), pp. 1–3.
Carpenter, J., B. J. Eggleton, and J. Schröder, 2014b, Opt. Express **22**, 96.
Carpenter, J., B. J. Eggleton, and J. Schröder, 2015, Nat. Photonics **9**, 751.
Carroll, J. E., J. Whiteaway, and D. Plumb, 1998, *Distributed Feedback Semiconductor Lasers (IET)* (The Institution of Electrical Engineers, Herts, UK).
Cartwright, J., 2007, "Opaque lens focuses light" [http://physicsworld.com/cws/article/news/2007/aug/15/opaque-lens-focuses-light]
Cazé, A., R. Pierrat, and R. Carminati, 2010, Phys. Rev. A **82**, 043823.

Cazé, A., R. Pierrat, and R. Carminati, 2013, Phys. Rev. Lett. **110**, 063903.
Cerjan, A., B. Redding, L. Ge, S. F. Liew, H. Cao, and A. D. Stone, 2016, Opt. Express **24**, 26006.
Chaigne, T., J. Gateau, O. Katz, E. Bossy, and S. Gigan, 2014, Opt. Lett. **39**, 2664.
Chaigne, T., O. Katz, A. C. Boccara, M. Fink, E. Bossy, and S. Gigan, 2014, Nat. Photonics **8**, 58.
Chang, A. M., H. U. Baranger, L. N. Pfeiffer, and K. W. West, 1994, Phys. Rev. Lett. **73**, 2111.
Cheong, W.-F., S. A. Prahl, and A. J. Welch, 1990, IEEE J. Quantum Electron. **26**, 2166.
Ching, E. S. C., P. T. Leung, A. Maassen van den Brink, W. M. Suen, S. S. Tong, and K. Young, 1998, Rev. Mod. Phys. **70**, 1545.
Chizhik, D., J. Ling, P. Wolniansky, R. Valenzuela, N. Costa, and K. Huber, 2003, IEEE J. Sel. Areas Commun. **21**, 321.
Choi, W., C. Fang-Yen, K. Badizadegan, S. Oh, N. Lue, R. R. Dasari, and M. S. Feld, 2007, Nat. Methods **4**, 717.
Choi, W., A. P. Mosk, Q.-H. Park, and W. Choi, 2011, Phys. Rev. B **83**, 134207.
Choi, W., Q.-H. Park, and W. Choi, 2012, Opt. Express **20**, 20721.
Choi, Y., T. R. Hillman, W. Choi, N. Lue, R. R. Dasari, P. T. C. So, W. Choi, and Z. Yaqoob, 2013, Phys. Rev. Lett. **111**, 243901.
Choi, Y., T. D. Yang, C. Fang-Yen, P. Kang, K. J. Lee, R. R. Dasari, M. S. Feld, and W. Choi, 2011, Phys. Rev. Lett. **107**, 023902.
Choi, Y., C. Yoon, M. Kim, T. D. Yang, C. Fang-Yen, R. R. Dasari, K. J. Lee, and W. Choi, 2012, Phys. Rev. Lett. **109**, 203901.
Chong, Y. D., L. Ge, H. Cao, and A. D. Stone, 2010, Phys. Rev. Lett. **105**, 053901.
Chong, Y. D., L. Ge, and A. D. Stone, 2011, Phys. Rev. Lett. **106**, 093902.
Chong, Y. D., and A. D. Stone, 2011, Phys. Rev. Lett. **107**, 163901.
Čižmár, T., and K. Dholakia, 2011, Opt. Express **19**, 18871.
Čižmár, T., and K. Dholakia, 2012, Nat. Commun. **3**, 1027.
Conkey, D. B., A. N. Brown, A. M. Caravaca-Aguirre, and R. Piestun, 2012, Opt. Express **20**, 4840.
Conkey, D. B., A. M. Caravaca-Aguirre, J. D. Dove, H. Ju, T. W. Murray, and R. Piestun, 2015, Nat. Commun. **6**, 7902.
Conkey, D. B., A. M. Caravaca-Aguirre, and R. Piestun, 2012, Opt. Express **20**, 1733.
Cornelissen, S. A., T. G. Bifano, and P. A. Bierden, 2012, Proc. SPIE Int. Soc. Opt. Eng. **8253**, 825306.
Cox, G., 2012, *Optical Imaging Techniques in Cell Biology* (Taylor & Francis, London).
Crespi, A., R. Osellame, R. Ramponi, V. Giovannetti, R. Fazio, L. Sansoni, F. De Nicola, F. Sciarrino, and P. Mataloni, 2013, Nat. Photonics **7**, 322.
Cuche, E., P. Marquet, and C. Depeursinge, 2000, Appl. Opt. **39**, 4070.
Cui, M., and C. Yang, 2010, Opt. Express **18**, 3444.
Curry, N., P. Bondareff, M. Leclercq, N. F. van Hulst, R. Sapienza, S. Gigan, and S. Gresillon, 2011, Opt. Lett. **36**, 3332.
Datta, S., 1997, *Electronic Transport in Mesoscopic Systems* (Cambridge University Press, Cambridge, England).
Davy, M., Z. Shi, and A. Z. Genack, 2012, Phys. Rev. B **85**, 035105.
Davy, M., Z. Shi, J. Park, C. Tian, and A. Z. Genack, 2015, Nat. Commun. **6**, 6893.
Davy, M., Z. Shi, J. Wang, X. Cheng, and A. Z. Genack, 2015, Phys. Rev. Lett. **114**, 033901.
Defienne, H., M. Barbieri, B. Chalopin, B. Chatel, I. A. Walmsley, B. J. Smith, and S. Gigan, 2014, Opt. Lett. **39**, 6090.
Defienne, H., M. Barbieri, I. A. Walmsley, B. J. Smith, and S. Gigan, 2016, Sci. Adv. **2**, e1501054.
de Jong, M. J. M., and C. W. J. Beenakker, 1992, Phys. Rev. B **46**, 13400.
Delagnes, J. C., A. Monmayrant, P. Zahariev, A. Arbouet, B. Chatel, B. Girard, and M. A. Bouchene, 2007, Appl. Phys. B **86**, 573.
Dembowski, C., H.-D. Gräf, R. Hofferbert, H. Rehfeld, A. Richter, and T. Weiland, 1999, Phys. Rev. E **60**, 3942.
Derode, A., P. Roux, and M. Fink, 1995, Phys. Rev. Lett. **75**, 4206.
Derode, A., A. Tourin, and M. Fink, 1999, J. Appl. Phys. **85**, 6343.
Derode, A., A. Tourin, and M. Fink, 2001a, Phys. Rev. E **64**, 036606.
Derode, A., A. Tourin, and M. Fink, 2001b, Phys. Rev. E **64**, 036605.
de Rosny, J., and M. Fink, 2002, Phys. Rev. Lett. **89**, 124301.
Deubel, M., G. von Freymann, M. Wegener, S. Pereira, K. Busch, and C. M. Soukoulis, 2004, Nat. Mater. **3**, 444.
Devaux, F., E. Guiot, and E. Lantz, 1998, Opt. Lett. **23**, 1597.
Di Battista, D., G. Zacharakis, and M. Leonetti, 2015, arXiv:1506.06886.
Dietz, B., and A. Richter, 2015, Chaos **25**, 097601.
Di Leonardo, R., and S. Bianchi, 2011, Opt. Express **19**, 247.
Donoho, D. L., 2006, IEEE Trans. Inf. Theory **52**, 1289.
Dorokhov, O., 1982, JETP Lett. **36**, 318 [http://www.jetpletters.ac.ru/ps/1335/article_27160.shtml].
Dorokhov, O., 1983, Sov. Phys. JETP **58**, 606 [http://www.jetp.ac.ru/cgi-bin/e/index/e/58/3/p606?a=list].
Dorokhov, O., 1984, Solid State Commun. **51**, 381.
Draeger, C., and M. Fink, 1997, Phys. Rev. Lett. **79**, 407.
Dragoman, D., and M. Dragoman, 2004, *Quantum-Classical Analogies* (Springer, New York).
Drémeau, A., A. Liutkus, D. Martina, O. Katz, C. Schülke, F. Krzakala, S. Gigan, and L. Daudet, 2015, Opt. Express **23**, 11898.
Dyson, F., 1962a, J. Math. Phys. (N.Y.) **3**, 157.
Dyson, F. J., 1962b, J. Math. Phys. (N.Y.) **3**, 140.
Economou, E. N., and C. M. Soukoulis, 1981, Phys. Rev. Lett. **46**, 618.
Edwards, J. T., and D. J. Thouless, 1972, J. Phys. C **5**, 807.
Efetov, K. B., and A. I. Larkin, 1983, Sov. Phys. JETP **58**, 444 [http://www.jetp.ac.ru/cgi-bin/e/index/e/58/2/p444?a=list].
Eisenbud, L., 1948, Ph.D. Dissertation, Ph.D. thesis (Princeton University).
El-Ganainy, R., K. G. Makris, D. N. Christodoulides, and Z. H. Musslimani, 2007, Opt. Lett. **32**, 2632.
Ellegaard, C., T. Guhr, K. Lindemann, H. Q. Lorensen, J. Nygård, and M. Oxborrow, 1995, Phys. Rev. Lett. **75**, 1546.
Fallert, J., R. J. B. Dietz, J. Sartor, D. Schneider, C. Klingshirn, and H. Kalt, 2009, Nat. Photonics **3**, 279.
Fan, S., and J. M. Kahn, 2005, Opt. Lett. **30**, 135.
Farahi, S., E. Benoit, A. A. Grabar, J.-P. Huignard, and F. Ramaz, 2012, Opt. Lett. **37**, 2754.
Farahi, S., D. Ziegler, I. N. Papadopoulos, D. Psaltis, and C. Moser, 2013, Opt. Express **21**, 22504.
Faulkner, J. S., 1977, J. Phys. C **10**, 4661.
Feinberg, J., and R. W. Hellwarth, 1980, Opt. Lett. **5**, 519.
Feng, S., C. Kane, P. A. Lee, and A. D. Stone, 1988, Phys. Rev. Lett. **61**, 834.
Ferry, D. K., and S. M. Goodnick, 1997, *Transport in Nanostructures* (Cambridge University Press, Cambridge, England).
Feshbach, H., 1958, Ann. Phys. (N.Y.) **5**, 357.
Feshbach, H., 1962, Ann. Phys. (N.Y.) **19**, 287.
Fienup, J. R., 1982, Appl. Opt. **21**, 2758.
Fink, M., 1997, Phys. Today **50**, No. 3, 34.
Fisher, D. S., and P. A. Lee, 1981, Phys. Rev. B **23**, 6851.
Fisher, R. A., 2012, *Optical Phase Conjugation* (Academic Press, New York).

Florescu, M., S. Torquato, and P. J. Steinhardt, 2009, Proc. Natl. Acad. Sci. U.S.A. **106**, 20658.
Frahm, K., 1995, Phys. Rev. Lett. **74**, 4706.
Freund, I., 1990a, Physica A (Amsterdam) **168**, 49.
Freund, I., 1990b, Opt. Lett. **15**, 1425.
Freund, I., and R. Berkovits, 1990, Phys. Rev. B **41**, 496.
Freund, I., and M. Rosenbluh, 1991, Opt. Commun. **82**, 362.
Freund, I., M. Rosenbluh, and S. Feng, 1988, Phys. Rev. Lett. **61**, 2328.
Friedman, W. A., and P. A. Mello, 1985a, Ann. Phys. (N.Y.) **161**, 276.
Friedman, W. A., and P. A. Mello, 1985b, J. Phys. A **18**, 425.
Froufe-Pérez, L. S., M. Engel, P. F. Damasceno, N. Muller, J. Haberko, S. C. Glotzer, and F. Scheffold, 2016, Phys. Rev. Lett. **117**, 053902.
Fukushima, T., T. Harayama, P. Davis, P. O. Vaccaro, T. Nishimura, and T. Aida, 2002, Opt. Lett. **27**, 1430.
Gad-el Hak, M., 2010, *The MEMS handbook* (CRC Press, Boca Raton, FL), Vol. 17.
Gaio, M., M. Castro-Lopez, J. Renger, N. v. Hulst, and R. Sapienza, 2015, Faraday Discuss. **178**, 237.
Galisteo-Lopez, J. F., M. Ibisate, R. Sapienza, L. S. Froufe-Perez, A. Blanco, and C. Lopez, 2011, Adv. Mater. **23**, 30.
Gamow, G., 1928, Z. Phys. **51**, 204.
García, P. D., A. Javadi, H. Thyrrestrup, and P. Lodahl, 2013, Appl. Phys. Lett. **102**, 031101.
García, P. D., S. Stobbe, I. Söllner, and P. Lodahl, 2012, Phys. Rev. Lett. **109**, 253902.
García-Martín, A., F. Scheffold, M. Nieto-Vesperinas, and J. J. Sáenz, 2002, Phys. Rev. Lett. **88**, 143901.
Ge, L., 2015, Opt. Express **23**, 30049.
Ge, L., O. Malik, and H. E. Türeci, 2014, Nat. Photonics **8**, 871.
Gehler, S., B. Köber, G. L. Celardo, and U. Kuhl, 2016, Phys. Rev. B **94**, 161407(R).
Gehner, A., M. Wildenhain, H. Neumann, J. Knobbe, and O. Komenda, 2006, Proc. SPIE Int. Soc. Opt. Eng. **6113**, 61130K.
Gérardin, B., J. Laurent, P. Ambichl, C. Prada, S. Rotter, and A. Aubry, 2016, Phys. Rev. B **94**, 014209.
Gérardin, B., J. Laurent, A. Derode, C. Prada, and A. Aubry, 2014, Phys. Rev. Lett. **113**, 173901.
Ghielmetti, G., and C. M. Aegerter, 2012, Opt. Express **20**, 3744.
Ghielmetti, G., and C. M. Aegerter, 2014, Opt. Express **22**, 1981.
Gigan, S., 2012, Physics **5**, 127.
Gjonaj, B., J. Aulbach, P. M. Johnson, A. P. Mosk, L. Kuipers, and A. Lagendijk, 2011, Nat. Photonics **5**, 360.
Gjonaj, B., J. Aulbach, P. M. Johnson, A. P. Mosk, L. Kuipers, and A. Lagendijk, 2013, Phys. Rev. Lett. **110**, 266804.
Goetschy, A., and A. D. Stone, 2013, Phys. Rev. Lett. **111**, 063901.
Goodman, J. W., 1976, J. Opt. Soc. Am. **66**, 1145.
Goodman, J. W., 2007, *Speckle Phenomena in Optics: Theory and Applications* (Roberts and Company, Greenwood Village, CO).
Goorden, S. A., J. Bertolotti, and A. P. Mosk, 2014, Opt. Express **22**, 17999.
Goorden, S. A., M. Horstmann, A. P. Mosk, B. Škorić, and P. W. H. Pinkse, 2014, Optica **1**, 421.
Gopar, V. A., and P. A. Mello, 1998, Europhys. Lett. **42**, 131.
Gorkov, L., A. I. Larkin, and D. Khmelnitskii, 1979, JETP Lett. **30**, 228 [http://www.jetpletters.ac.ru/ps/1364/article_20629.shtml].
Gower, M., and D. Proch, 1994, *Optical Phase Conjugation* (Springer, New York).
Gräf, H.-D., H. L. Harney, H. Lengeler, C. H. Lewenkopf, C. Rangacharyulu, A. Richter, P. Schardt, and H. A. Weidenmüller, 1992, Phys. Rev. Lett. **69**, 1296.
Griffiths, D. J., 1999, *Introduction to Electrodynamics* (Prentice-Hall, Englewood Cliffs, NJ).
Guan, Y., O. Katz, E. Small, J. Zhou, and Y. Silberberg, 2012, Opt. Lett. **37**, 4663.
Guhr, T., A. Müller-Groeling, and H. A. Weidenmüller, 1998, Phys. Rep. **299**, 189.
Haberko, J., N. Muller, and F. Scheffold, 2013, Phys. Rev. A **88**, 043822.
Hastings, M. B., A. D. Stone, and H. U. Baranger, 1994, Phys. Rev. B **50**, 8230.
Henny, M., S. Oberholzer, C. Strunk, and C. Schönenberger, 1999, Phys. Rev. B **59**, 2871.
Hildner, R., D. Brinks, J. B. Nieder, R. J. Cogdell, and N. F. v. Hulst, 2013, Science **340**, 1448.
Hillman, T. R., T. Yamauchi, W. Choi, R. R. Dasari, M. S. Feld, Y. Park, and Z. Yaqoob, 2013, Sci. Rep. **3**, 01909.
Hisch, T., M. Liertzer, D. Pogany, F. Mintert, and S. Rotter, 2013, Phys. Rev. Lett. **111**, 023902.
Ho, K.-P., and J. Kahn, 2011, J. Lightwave Technol. **29**, 3119.
Ho, K.-P., and J. M. Kahn, 2014, J. Lightwave Technol. **32**, 614.
Höhmann, R., U. Kuhl, H.-J. Stöckmann, L. Kaplan, and E. J. Heller, 2010, Phys. Rev. Lett. **104**, 093901.
Hornbeck, L. J., 2001, MRS Bull. **26**, 325.
Horstmeyer, R., H. Ruan, and C. Yang, 2015, Nat. Photonics **9**, 563.
Houten, H. v., and C. Beenakker, 1996, Phys. Today **49**, No. 7, 22.
Hsieh, C.-L., Y. Pu, R. Grange, G. Laporte, and D. Psaltis, 2010, Opt. Express **18**, 20723.
Hsieh, C.-L., Y. Pu, R. Grange, and D. Psaltis, 2010, Opt. Express **18**, 12283.
Hsu, C. W., A. Goetschy, Y. Bromberg, A. D. Stone, and H. Cao, 2015, Phys. Rev. Lett. **115**, 223901.
Hsu, C. W., S. F. Liew, A. Goetschy, H. Cao, and A. D. Stone, 2017, Nat. Phys. (to be published).
Huibers, A. G., S. R. Patel, C. M. Marcus, P. W. Brouwer, C. I. Duruöz, and J. S. Harris, 1998, Phys. Rev. Lett. **81**, 1917.
Huisman, T. J., S. R. Huisman, A. P. Mosk, and P. W. H. Pinkse, 2014, Appl. Phys. B **116**, 603.
Hutley, M. C., and D. Maystre, 1976, Opt. Commun. **19**, 431.
Iida, S., H. A. Weidenmüller, and J. A. Zuk, 1990a, Ann. Phys. (N.Y.) **200**, 219.
Iida, S., H. A. Weidenmüller, and J. A. Zuk, 1990b, Phys. Rev. Lett. **64**, 583.
Ilić, I., P. P. Beličev, V. Milanović, and J. Radovanović, 2009, Phys. Scr. **T135**, 014040.
Imry, Y., 1986, Europhys. Lett. **1**, 249.
Imry, Y., 2002, *Introduction to Mesoscopic Physics* (Oxford University Press, New York).
Ivakhnik, V. V., V. M. Petnikova, V. S. Solomatin, and V. V. Shuvalov, 1980, Sov. J. Quantum Electron. **10**, 373.
Izrailev, F. M., and N. M. Makarov, 2005, J. Phys. A **38**, 10613.
Jackson, J. D., 1998, *Classical Electrodynamics* (Wiley, New York).
Jacquod, P., and E. V. Sukhorukov, 2004, Phys. Rev. Lett. **92**, 116801.
Jalabert, R. A., J.-L. Pichard, and C. W. J. Beenakker, 1994, Europhys. Lett. **27**, 255.
Jalas, D., *et al.*, 2013, Nat. Photonics **7**, 579.
Janssen, M., 2001, *Fluctuations and Localization in Mesoscopic Electron Systems* (World Scientific, Singapore).
Jauch, J. M., K. B. Sinha, and B. N. Misra, 1972, Helv. Phys. Acta **45**, 398 [http://www.e-periodica.ch/digbib/view?pid=hpa-001:1972:45::404#404].
Jayet, B., J.-P. Huignard, and F. Ramaz, 2013, Opt. Lett. **38**, 1256.

Jin, C., R. R. Nadakuditi, E. Michielssen, and S. Rand, 2014, J. Opt. Soc. Am. A **31**, 1788.
Jin, C., R. R. Nadakuditi, E. Michielssen, and S. C. Rand, 2013, J. Opt. Soc. Am. A **30**, 1592.
Joannopoulos, J. D., S. G. Johnson, J. N. Winn, and R. D. Meade, 2008, *Photonic Crystals: Molding the Flow of Light (Second Edition)* (Princeton University Press, Princeton, NJ).
Judkewitz, B., R. Horstmeyer, I. M. Vellekoop, I. N. Papadopoulos, and C. Yang, 2015, Nat. Phys. **11**, 684.
Judkewitz, B., Y. M. Wang, R. Horstmeyer, A. Mathy, and C. Yang, 2013, Nat. Photonics **7**, 300.
Kaina, N., M. Dupré, G. Lerosey, and M. Fink, 2014, Sci. Rep. **4**, 6693.
Kang, S., S. Jeong, W. Choi, H. Ko, T. D. Yang, J. H. Joo, J.-S. Lee, Y.-S. Lim, Q.-H. Park, and W. Choi, 2015, Nat. Photonics **9**, 253.
Kapur, P. L., and R. Peierls, 1938, Proc. R. Soc. A **166**, 277.
Karaguleff, C., and G. L. Clark, 1990, Opt. Lett. **15**, 820.
Katz, O., P. Heidmann, M. Fink, and S. Gigan, 2014, Nat. Photonics **8**, 784.
Katz, O., E. Small, Y. Bromberg, and Y. Silberberg, 2011, Nat. Photonics **5**, 372.
Katz, O., E. Small, Y. Guan, and Y. Silberberg, 2014, Optica **1**, 170.
Katz, O., E. Small, and Y. Silberberg, 2012, Nat. Photonics **6**, 549.
Kawata, S., M. Ohtsu, and M. Irie, 2002, *Nano-Optics* (Springer, New York).
Kawata, S., H.-B. Sun, T. Tanaka, and K. Takada, 2001, Nature (London) **412**, 697.
Khlus, V. A., 1987, Sov. Phys. JETP **66**, 1243 [http://www.jetp.ac.ru/cgi-bin/e/index/e/66/6/p1243?a=list].
Khmel'nitskii, D. E., 1984, Physica B+C (Amsterdam) **126**, 235.
Kim, D., W. Choi, M. Kim, J. Moon, K. Seo, S. Ju, and W. Choi, 2014, Opt. Commun. **330**, 35.
Kim, M., W. Choi, C. Yoon, G. H. Kim, and W. Choi, 2013, Opt. Lett. **38**, 2994.
Kim, M., W. Choi, C. Yoon, G. H. Kim, S.-h. Kim, G.-R. Yi, Q.-H. Park, and W. Choi, 2015b, Opt. Express **23**, 12740.
Kim, M., Y. Choi, C. Yoon, W. Choi, J. Kim, Q.-H. Park, and W. Choi, 2012, Nat. Photonics **6**, 581.
Kneissl, M., M. Teepe, N. Miyashita, N. M. Johnson, G. D. Chern, and R. K. Chang, 2004, Appl. Phys. Lett. **84**, 2485.
Kohlgraf-Owens, T., and A. Dogariu, 2008, Opt. Express **16**, 13225.
Kohlgraf-Owens, T. W., and A. Dogariu, 2010, Opt. Lett. **35**, 2236.
Kong, F., R. H. Silverman, L. Liu, P. V. Chitnis, K. K. Lee, and Y. C. Chen, 2011, Opt. Lett. **36**, 2053.
Kottos, T., 2005, J. Phys. A **38**, 10761.
Krachmalnicoff, V., E. Castanié, Y. De Wilde, and R. Carminati, 2010, Phys. Rev. Lett. **105**, 183901.
Kragl, H., 1992, J. Opt. Soc. Am. A **9**, 964.
Králiková, B., J. Skála, P. Straka, and H. Turcicová, 1997, Opt. Lett. **22**, 766.
Krein, M. G., 1962, Dokl. Akad. Nauk SSSR **144**, 475.
Kuhl, U., R. Höhmann, J. Main, and H.-J. Stöckmann, 2008, Phys. Rev. Lett. **100**, 254101.
Laforest, T., A. Verdant, A. Dupret, S. Gigan, and F. Ramaz, 2012, in 2012 IEEE Sensors, pp. 1–4.
Lagendijk, A., B. v. Tiggelen, and D. S. Wiersma, 2009, Phys. Today **62**, No. 8, 24.
Lagendijk, A., and B. A. van Tiggelen, 1996, Phys. Rep. **270**, 143.
Lai, P., L. Wang, J. W. Tay, and L. V. Wang, 2015, Nat. Photonics **9**, 126.
Landauer, R., 1957, IBM J. Res. Dev. **1**, 223.
Landauer, R., and M. Büttiker, 1987, Phys. Rev. B **36**, 6255.
Lee, P. A., and A. D. Stone, 1985, Phys. Rev. Lett. **55**, 1622.
Lee, R. W., and J. C. Harp, 1969, Proc. IEEE **57**, 375.
Leith, E. N., and J. Upatnieks, 1966, J. Opt. Soc. Am. **56**, 523.
Leith, E. N., J. Upatnieks, and K. A. Haines, 1965, J. Opt. Soc. Am. **55**, 981.
Lemoult, F., G. Lerosey, J. de Rosny, and M. Fink, 2009, Phys. Rev. Lett. **103**, 173902.
Lerosey, G., J. De Rosny, A. Tourin, and M. Fink, 2007, Science **315**, 1120.
Lesovik, G. B., 1989, JETP Lett. **49**, 592 [http://www.jetpletters.ac.ru/ps/1120/article_16970.shtml].
Levi, L., M. Rechtsman, B. Freedman, T. Schwartz, O. Manela, and M. Segev, 2011, Science **332**, 1541.
Lhermite, J., A. Desfarges-Berthelemot, V. Kermene, and A. Barthelemy, 2007, Opt. Lett. **32**, 1842.
Lhermite, J., E. Suran, V. Kermene, F. Louradour, A. Desfarges-Berthelemot, and A. Barthélémy, 2010, Opt. Express **18**, 4783.
Liew, S. F., S. M. Popoff, A. P. Mosk, W. L. Vos, and H. Cao, 2014, Phys. Rev. B **89**, 224202.
Liew, S. F., S. M. Popoff, S. W. Sheehan, A. Goetschy, C. A. Schmuttenmaer, A. D. Stone, and H. Cao, 2016, ACS Photonics **3**, 449.
Liew, S. F., B. Redding, L. Ge, G. S. Solomon, and H. Cao, 2014, Appl. Phys. Lett. **104**, 231108.
Lifante, G., 2003, *Integrated Photonics: Fundamentals* (John Wiley & Sons, New York).
Liu, C., R. E. C. van der Wel, N. Rotenberg, L. Kuipers, T. F. Krauss, A. Di Falco, and A. Fratalocchi, 2015, Nat. Phys. **11**, 358.
Liu, Y., P. Lai, C. Ma, X. Xu, A. A. Grabar, and L. V. Wang, 2015, Nat. Commun. **6**, 5904.
Liutkus, A., D. Martina, S. Popoff, G. Chardon, O. Katz, G. Lerosey, S. Gigan, L. Daudet, and I. Carron, 2014, Sci. Rep. **4**, 5552.
Longhi, S., 2010, Phys. Rev. A **82**, 031801.
Loterie, D., S. Farahi, I. Papadopoulos, A. Goy, D. Psaltis, and C. Moser, 2015, Opt. Express **23**, 23845.
Lueder, E., 2010, *Liquid crystal displays: Addressing schemes and electro-optical effects* (Wiley, New York).
Lyuboshitz, V., 1977, Phys. Lett. B **72**, 41.
MacKintosh, F. C., J. X. Zhu, D. J. Pine, and D. A. Weitz, 1989, Phys. Rev. B **40**, 9342.
Mahaux, C., and H. A. Weidenmüller, 1969, *Shell-model approach to nuclear reactions* (North-Holland Pub. Co., Amsterdam).
Mailly, D., and M. Sanquer, 1992, J. Phys. I (France) **2**, 357.
Makris, K., L. Ge, and H. Türeci, 2014, Phys. Rev. X **4**, 041044.
Makris, K. G., A. Brandstötter, P. Ambichl, Z. H. Musslimani, and S. Rotter, 2016, arXiv:1612.03070.
Makris, K. G., R. El-Ganainy, D. N. Christodoulides, and Z. H. Musslimani, 2008, Phys. Rev. Lett. **100**, 103904.
Makris, K. G., Z. H. Musslimani, D. N. Christodoulides, and S. Rotter, 2015, Nat. Commun. **6**, 7257.
Marčenko, V. A., and L. A. Pastur, 1967, Mathematics of the USSR-Sbornik **1**, 457 [http://iopscience.iop.org/article/10.1070/SM1967v001n04ABEH001994/meta].
Marconcini, P., M. Macucci, G. Iannaccone, B. Pellegrini, and G. Marola, 2006, Europhys. Lett. **73**, 574.
Marcus, C. M., A. J. Rimberg, R. M. Westervelt, P. F. Hopkins, and A. C. Gossard, 1992, Phys. Rev. Lett. **69**, 506.
Marcus, C. M., *et al.*, 1997, Chaos Solitons Fractals **8**, 1261.
Maret, G., T. Sperling, W. Bührer, A. Lubatsch, R. Frank, and C. M. Aegerter, 2013, Nat. Photonics **7**, 934.
Martin, O. J. F., C. Girard, and A. Dereux, 1995, Phys. Rev. Lett. **74**, 526.
Martin, P. A., 1976, Commun. Math. Phys. **47**, 221.
Martin, T., and R. Landauer, 1992, Phys. Rev. B **45**, 1742.

Maurer, C., A. Jesacher, S. Bernet, and M. Ritsch-Marte, 2011, Laser Photonics Rev. **5**, 81.
McCabe, D. J., A. Tajalli, D. R. Austin, P. Bondareff, I. A. Walmsley, S. Gigan, and B. Chatel, 2011, Nat. Commun. **2**, 447.
McGloin, D., and K. Dholakia, 2005, Contemp. Phys. **46**, 15.
McMichael, I., P. Yeh, and P. Beckwith, 1987, Opt. Lett. **12**, 507.
Mehta, M. L., 2004, *Random Matrices* (Academic Press, New York).
Mello, P., P. Pereyra, and N. Kumar, 1988, Ann. Phys. (N.Y.) **181**, 290.
Mello, P. A., and N. Kumar, 2004, *Quantum Transport in Mesoscopic Systems: Complexity and Statistical Fluctuations, a Maximum-entropy Viewpoint* (Oxford University Press, New York).
Mello, P. A., P. Pereyra, and T. H. Seligman, 1985, Ann. Phys. (N.Y.) **161**, 254.
Méndez-Bermúdez, J. A., and T. Kottos, 2005, Phys. Rev. B **72**, 064108.
Méndez-Sánchez, R. A., U. Kuhl, M. Barth, C. H. Lewenkopf, and H.-J. Stöckmann, 2003, Phys. Rev. Lett. **91**, 174102.
Metzger, J. J., R. Fleischmann, and T. Geisel, 2010, Phys. Rev. Lett. **105**, 020601.
Milione, G., D. A. Nolan, and R. R. Alfano, 2015, J. Opt. Soc. Am. B **32**, 143.
Mitchell, G. E., A. Richter, and H. A. Weidenmüller, 2010, Rev. Mod. Phys. **82**, 2845.
Moiseyev, N., 2011, *Non-Hermitian Quantum Mechanics* (Cambridge University Press, Cambridge, England).
Monmayrant, A., S. Weber, and B. Chatel, 2010, J. Phys. B **43**, 103001.
Montambaux, G., 2006, arXiv:cond-mat/0611574.
Montie, E. A., E. C. Cosman, G. W. 't Hooft, M. B. van der Mark, and C. W. J. Beenakker, 1991, Nature (London) **350**, 594.
Morales-Delgado, E. E., S. Farahi, I. N. Papadopoulos, D. Psaltis, and C. Moser, 2015, Opt. Express **23**, 9109.
Morse, P. M., and H. Feshbach, 1953, *Methods of theoretical physics* (McGraw-Hill, New York).
Mosk, A. P., A. Lagendijk, G. Lerosey, and M. Fink, 2012, Nat. Photonics **6**, 283.
Mounaix, M., D. Andreoli, H. Defienne, G. Volpe, O. Katz, S. Grésillon, and S. Gigan, 2016, Phys. Rev. Lett. **116**, 253901.
Mounaix, M., H. Defienne, and S. Gigan, 2016, Phys. Rev. A **94**, 041802.
Muller, N., J. Haberko, C. Marichy, and F. Scheffold, 2014, Adv. Opt. Mater. **2**, 115.
Müller, S., S. Heusler, P. Braun, F. Haake, and A. Altland, 2004, Phys. Rev. Lett. **93**, 014103.
Muskens, O. L., P. Venn, T. van der Beek, and T. Wellens, 2012, Phys. Rev. Lett. **108**, 223906.
Muttalib, K. A., 1990, Phys. Rev. Lett. **65**, 745.
Nagaev, K. E., 1992, Phys. Lett. A **169**, 103.
Nazarov, Y. V., 1994, Phys. Rev. Lett. **73**, 134.
Nazmitdinov, R. G., H.-S. Sim, H. Schomerus, and I. Rotter, 2002, Phys. Rev. B **66**, 241302.
Nieto-Vesperinas, M., and E. Wolf, 1986, J. Opt. Soc. Am. A **3**, 2038.
Noh, H., Y. Chong, A. D. Stone, and H. Cao, 2012, Phys. Rev. Lett. **108**, 186805.
Noh, H., S. M. Popoff, and H. Cao, 2013, Opt. Express **21**, 17435.
Ntziachristos, V., 2010, Nat. Methods **7**, 603.
Oberholzer, S., E. V. Sukhorukov, and C. Schönenberger, 2002, Nature (London) **415**, 765.
Ossipov, A., T. Kottos, and T. Geisel, 2003, Europhys. Lett. **62**, 719.
Ott, J. R., N. A. Mortensen, and P. Lodahl, 2010, Phys. Rev. Lett. **105**, 090501.
Papadopoulos, I. N., S. Farahi, C. Moser, and D. Psaltis, 2012, Opt. Express **20**, 10583.
Papadopoulos, I. N., S. Farahi, C. Moser, and D. Psaltis, 2013, Biomed. Opt. Express **4**, 260.
Papadopoulos, I. N., O. Simandoux, S. Farahi, J. P. Huignard, E. Bossy, D. Psaltis, and C. Moser, 2013, Appl. Phys. Lett. **102**, 211106.
Papas, C. H., 2011, *English Theory of Electromagnetic Wave Propagation* (Dover Publications, New York).
Pappu, R., B. Recht, J. Taylor, and N. Gershenfeld, 2002, Science **297**, 2026.
Park, J.-H., C. Park, H. Yu, J. Park, S. Han, J. Shin, S. H. Ko, K. T. Nam, Y.-H. Cho, and Y. Park, 2013, Nat. Photonics **7**, 454.
Patterson, M. S., B. Chance, and B. C. Wilson, 1989, Appl. Opt. **28**, 2331.
Paudel, H. P., C. Stockbridge, J. Mertz, and T. Bifano, 2013, Opt. Express **21**, 17299.
Paurisse, M., M. Hanna, F. Druon, P. Georges, C. Bellanger, A. Brignon, and J. P. Huignard, 2009, Opt. Express **17**, 13000.
Pazourek, R., S. Nagele, and J. Burgdörfer, 2015, Rev. Mod. Phys. **87**, 765.
Peña, A., A. Girschik, F. Libisch, S. Rotter, and A. A. Chabanov, 2014, Nat. Commun. **5**, 3488.
Pendry, J. B., 1987, J. Phys. C **20**, 733.
Pendry, J. B., A. MacKinnon, and A. B. Pretre, 1990, Physica A (Amsterdam) **168**, 400.
Pendry, J. B., A. MacKinnon, and P. J. Roberts, 1992, Proc. R. Soc. A **437**, 67.
Peng, B., S. K. Ozdemir, F. Lei, F. Monifi, M. Gianfreda, G. L. Long, S. Fan, F. Nori, C. M. Bender, and L. Yang, 2014, Nat. Phys. **10**, 394.
Persson, E., I. Rotter, H.-J. Stöckmann, and M. Barth, 2000, Phys. Rev. Lett. **85**, 2478.
Pichard, J.-L., 1991, in *Quantum Coherence in Mesoscopic Systems*, NATO Advanced Study Institute, Series B: Physics, Vol. 254, edited by B. Kramer (Plenum, New York).
Pichard, J.-L., N. Zanon, Y. Imry, and A. Douglas Stone, 1990, J. Phys. IV (France) **51**, 587.
Pierrat, R., P. Ambichl, S. Gigan, A. Haber, R. Carminati, and S. Rotter, 2014, Proc. Natl. Acad. Sci. U.S.A. **111**, 17765.
Pierrat, R., C. Vandenbem, M. Fink, and R. Carminati, 2013, Phys. Rev. A **87**, 041801.
Plenio, M. B., and S. F. Huelga, 2008, New J. Phys. **10**, 113019.
Plöschner, M., T. Tyc, and T. Čižmár, 2015, Nat. Photonics **9**, 529.
Poole, C., and R. Wagner, 1986, Electron. Lett. **22**, 1029.
Popoff, S., A. Goetschy, S. Liew, A. Stone, and H. Cao, 2014, Phys. Rev. Lett. **112**, 133903.
Popoff, S., G. Lerosey, M. Fink, A. C. Boccara, and S. Gigan, 2010, Nat. Commun. **81**, 1.
Popoff, S. M., A. Aubry, G. Lerosey, M. Fink, A. C. Boccara, and S. Gigan, 2011, Phys. Rev. Lett. **107**, 263901.
Popoff, S. M., G. Lerosey, R. Carminati, M. Fink, A. C. Boccara, and S. Gigan, 2010, Phys. Rev. Lett. **104**, 100601.
Popoff, S. M., G. Lerosey, M. Fink, A. C. Boccara, and S. Gigan, 2011, New J. Phys. **13**, 123021.
Porter, C. E., 1965, *Statistical Theories of Spectra: Fluctuations: a Collection of Reprints and Original Papers* (Academic Press, New York).
Prada, C., and M. Fink, 1994, Wave Motion **20**, 151.
Rabinovitz, Y. K., 2011, "Digital Light Processing Technology (DLP) Beyond any conventional projection."
Redding, B., and H. Cao, 2012, Opt. Lett. **37**, 3384.

Redding, B., S. F. Liew, R. Sarma, and H. Cao, 2013, Nat. Photonics **7**, 746.
Redding, B., S. M. Popoff, and H. Cao, 2013, Opt. Express **21**, 6584.
Riboli, F., P. Barthelemy, S. Vignolini, F. Intonti, A. De Rossi, S. Combrie, and D. S. Wiersma, 2011, Opt. Lett. **36**, 127.
Riboli, F., *et al.*, 2014, Nat. Mater. **13**, 720.
Richardson, D. J., J. M. Fini, and L. E. Nelson, 2013, Nat. Photonics **7**, 354.
Roddier, F., 1999, *Adaptive Optics in Astronomy* (Cambridge University Press, Cambridge, England).
Rosen, S., D. Gilboa, O. Katz, and Y. Silberberg, 2015, arXiv:1506.08586.
Rotter, I., 2009, J. Phys. A **42**, 153001.
Rotter, S., F. Aigner, and J. Burgdörfer, 2007, Phys. Rev. B **75**, 125312.
Rotter, S., P. Ambichl, and F. Libisch, 2011, Phys. Rev. Lett. **106**, 120602.
Rotter, S., J.-Z. Tang, L. Wirtz, J. Trost, and J. Burgdörfer, 2000, Phys. Rev. B **62**, 1950.
Rüter, C. E., K. G. Makris, R. El-Ganainy, D. N. Christodoulides, M. Segev, and D. Kip, 2010, Nat. Phys. **6**, 192.
Sadreev, A. F., and I. Rotter, 2003, J. Phys. A **36**, 11413.
Sapienza, L., H. Thyrrestrup, S. Stobbe, P. D. Garcia, S. Smolka, and P. Lodahl, 2010, Science **327**, 1352.
Sapienza, R., P. Bondareff, R. Pierrat, B. Habert, R. Carminati, and N. F. van Hulst, 2011, Phys. Rev. Lett. **106**, 163902.
Sarma, R., A. Yamilov, S. Petrenko, Y. Bromberg, and H. Cao, 2016, Phys. Rev. Lett. **117**, 086803.
Savage, N., 2009, Nat. Photonics **3**, 170.
Savin, D. V., and H.-J. Sommers, 2003, Phys. Rev. E **68**, 036211.
Savin, D. V., and H.-J. Sommers, 2006, Phys. Rev. B **73**, 081307.
Scheffold, F., W. Härtl, G. Maret, and E. Matijević, 1997, Phys. Rev. B **56**, 10942.
Scheffold, F., and G. Maret, 1998, Phys. Rev. Lett. **81**, 5800.
Scheffold, F., and D. Wiersma, 2013, Nat. Photonics **7**, 934.
Schep, K. M., and G. E. W. Bauer, 1997, Phys. Rev. B **56**, 15860.
Schomerus, H., and P. Jacquod, 2005, J. Phys. A **38**, 10663.
Schönenberger, C., S. Oberholzer, E. V. Sukhorukov, and H. Grabert, 2001, arXiv:cond-mat/0112504.
Schönhuber, S., M. Brandstetter, T. Hisch, C. Deutsch, M. Krall, H. Detz, A. M. Andrews, G. Strasser, S. Rotter, and K. Unterrainer, 2016, Optica **3**, 1035.
Schott, S., J. Bertolotti, J.-F. Leger, L. Bourdieu, and S. Gigan, 2015, Opt. Express **23**, 13505.
Schottky, W., 1918, Ann. Phys. (Berlin) **362**, 541.
Schreiber, A., K. N. Cassemiro, V. Potoček, A. Gábris, I. Jex, and C. Silberhorn, 2011, Phys. Rev. Lett. **106**, 180403.
Schwartz, T., G. Bartal, S. Fishman, and M. Segev, 2007, Nature (London) **446**, 52.
Schwinger, J., 1951, Phys. Rev. **82**, 664.
Sebbah, P., 2001, *Waves and Imaging Through Complex Media* (Springer, New York).
Segev, M., Y. Silberberg, and D. N. Christodoulides, 2013, Nat. Photonics **7**, 197.
Seo, E., J. Ahn, W. Choi, H. Lee, Y. M. Jhon, S. Lee, and W. Choi, 2014, Opt. Lett. **39**, 5838.
Shapiro, B., 1999, Phys. Rev. Lett. **83**, 4733.
Shemirani, M. B., W. Mao, R. A. Panicker, and J. Kahn, 2009, J. Lightwave Technol. **27**, 1248.
Shi, Z., M. Davy, and A. Z. Genack, 2015, Opt. Express **23**, 12293.
Shi, Z., and A. Genack, 2012a, in *Frontiers in Optics 2012/Laser Science XXVIII*, OSA Technical Digest (online) (Optical Society of America), p. FTh3F.2.
Shi, Z., and A. Z. Genack, 2012b, Phys. Rev. Lett. **108**, 043901.
Shinohara, S., T. Harayama, T. Fukushima, M. Hentschel, T. Sasaki, and E. E. Narimanov, 2010, Phys. Rev. Lett. **104**, 163902.
Si, K., R. Fiolka, and M. Cui, 2012, Nat. Photonics **6**, 657.
Silvestrov, P. G., M. C. Goorden, and C. W. J. Beenakker, 2003, Phys. Rev. B **67**, 241301.
Skipetrov, S., and I. Sokolov, 2014, Phys. Rev. Lett. **112**, 023905.
Skipetrov, S. E., 2003, Phys. Rev. E **67**, 036621.
Skipetrov, S. E., and R. Maynard, 2000, Phys. Rev. B **62**, 886.
Small, E., O. Katz, Y. Guan, and Y. Silberberg, 2012, Opt. Lett. **37**, 3429.
Smith, F. T., 1960, Phys. Rev. **118**, 349.
Snyder, A. W., and J. Love, 1983, *Optical Waveguide Theory* (Springer, New York).
Sokolov, V. V., and V. Zelevinsky, 1997, Phys. Rev. C **56**, 311.
Solli, D. R., C. Ropers, P. Koonath, and B. Jalali, 2007, Nature (London) **450**, 1054.
Sperling, T., W. Bührer, C. M. Aegerter, and G. Maret, 2013, Nat. Photonics **7**, 48.
Sprik, R., A. Tourin, J. de Rosny, and M. Fink, 2008, Phys. Rev. B **78**, 012202.
Steinbach, A. H., J. M. Martinis, and M. H. Devoret, 1996, Phys. Rev. Lett. **76**, 3806.
Stöckmann, H.-J., 2006, *Quantum Chaos: An Introduction* (Cambridge University Press, Cambridge, England).
Stöckmann, H.-J., E. Persson, Y.-H. Kim, M. Barth, U. Kuhl, and I. Rotter, 2002, Phys. Rev. E **65**, 066211.
Stoffregen, U., J. Stein, H.-J. Stöckmann, M. Kuś, and F. Haake, 1995, Phys. Rev. Lett. **74**, 2666.
Stone, A. D., P. A. Mello, K. A. Muttalib, and J.-L. Pichard, 1991, in *Mesoscopic Phenomena in Solids*, edited by B. L. Altshuler, P. A. Lee, and R. A. webb (North-Holland, Amsterdam), p. 369.
Strudley, T., R. Bruck, B. Mills, and O. L. Muskens, 2014, Light Sci. Appl. **3**, e207.
Sukhorukov, E. V., and O. M. Bulashenko, 2005, Phys. Rev. Lett. **94**, 116803.
Sun, Y., W. Tan, H.-q. Li, J. Li, and H. Chen, 2014, Phys. Rev. Lett. **112**, 143903.
Tanabe, T., H. Tanabe, Y. Teramura, and F. Kannari, 2002, J. Opt. Soc. Am. B **19**, 2795.
Tang, J., R. N. Germain, and M. Cui, 2012, Proc. Natl. Acad. Sci. U.S.A. **109**, 8434.
Tanter, M., J.-L. Thomas, and M. Fink, 2000, J. Acoust. Soc. Am. **108**, 223.
Thouless, D. J., 1977, Phys. Rev. Lett. **39**, 1167.
Tiggelen, B. A. v., A. Tip, and A. Lagendijk, 1993, J. Phys. A **26**, 1731.
Tikhonov, A., 1963, Sov. Math. Dokl. **4**, 1035.
Topinka, M. A., B. J. LeRoy, R. M. Westervelt, S. E. J. Shaw, R. Fleischmann, E. J. Heller, K. D. Maranowski, and A. C. Gossard, 2001, Nature (London) **410**, 183.
Topolancik, J., F. Vollmer, and B. Ilic, 2007, Appl. Phys. Lett. **91**, 201102.
Tripathi, S., R. Paxman, T. Bifano, and K. C. Toussaint, Jr., 2012, Opt. Express **20**, 16067.
Tsang, L., J. A. Kong, and K.-H. Ding, 2004, *Scattering of Electromagnetic Waves, Theories and Applications* (John Wiley & Sons, New York).
Tse, D., and P. Viswanath, 2005, *Fundamentals Of Wireless Communication* (Cambridge University Press, Cambridge, England).

Türeci, H. E., A. D. Stone, and B. Collier, 2006, Phys. Rev. A **74**, 043822.
Umbach, C. P., S. Washburn, R. B. Laibowitz, and R. A. Webb, 1984, Phys. Rev. B **30**, 4048.
van Albada, M. P., J. F. de Boer, and A. Lagendijk, 1990, Phys. Rev. Lett. **64**, 2787.
van Beijnum, F., E. G. van Putten, A. Lagendijk, and A. P. Mosk, 2011, Opt. Lett. **36**, 373.
van Putten, E. G., D. Akbulut, J. Bertolotti, W. L. Vos, A. Lagendijk, and A. P. Mosk, 2011, Phys. Rev. Lett. **106**, 193905.
van Putten, E. G., I. M. Vellekoop, and A. P. Mosk, 2008, Appl. Opt. **47**, 2076.
van Tiggelen, B. A., and E. Kogan, 1994, Phys. Rev. A **49**, 708.
van Tiggelen, B. A., and R. Maynard, 1997, in *Wave Propagation in Complex Media*, The IMA Volumes in Mathematics and its Applications, Vol. 96, edited by G. Papanicolaou (Springer, Berlin), pp. 247–271.
van Wees, B. J., H. van Houten, C. W. J. Beenakker, J. G. Williamson, L. P. Kouwenhoven, D. van der Marel, and C. T. Foxon, 1988, Phys. Rev. Lett. **60**, 848.
Vedral, V., A. Barenco, and A. Ekert, 1996, Phys. Rev. A **54**, 147.
Vellekoop, I. M., 2008, arXiv:0807.1087.
Vellekoop, I. M., 2015, Opt. Express **23**, 12189.
Vellekoop, I. M., and C. M. Aegerter, 2010a, Proc. SPIE Int. Soc. Opt. Eng. **7554** 755430.
Vellekoop, I. M., and C. M. Aegerter, 2010b, Opt. Lett. **35**, 1245.
Vellekoop, I. M., A. Lagendijk, and A. P. Mosk, 2010, Nat. Photonics **4**, 320.
Vellekoop, I. M., P. Lodahl, and A. Lagendijk, 2005, Phys. Rev. E **71**, 056604.
Vellekoop, I. M., and A. P. Mosk, 2007, Opt. Lett. **32**, 2309.
Vellekoop, I. M., and A. P. Mosk, 2008a, Opt. Commun. **281**, 3071.
Vellekoop, I. M., and A. P. Mosk, 2008b, Phys. Rev. Lett. **101**, 120601.
Vellekoop, I. M., E. G. van Putten, A. Lagendijk, and A. P. Mosk, 2008, Opt. Express **16**, 67.
Verbaarschot, J. J. M., H. A. Weidenmüller, and M. R. Zirnbauer, 1985, Phys. Rep. **129**, 367.
Viviescas, C., and G. Hackenbroich, 2003, Phys. Rev. A **67**, 013805.
Voronin, E. S., V. V. Ivakhnik, V. M. Petnikova, V. S. Solomatin, and V. V. Shuvalov, 1979, Sov. J. Quantum Electron. **9**, 765.
Vos, W. L., A. Lagendijk, and A. P. Mosk, 2015, *Light Localisation and Lasing: Random and Quasi-Random Photonic Structures*, edited by M. Ghulinyan and L. Pavesi (Cambridge University Press, Cambridge, England), Chap. 1, p. 1.
Vynck, K., M. Burresi, F. Riboli, and D. S. Wiersma, 2012, Nat. Mater. **11**, 1017.
Wan, W., Y. Chong, L. Ge, H. Noh, A. D. Stone, and H. Cao, 2011, Science **331**, 889.
Wang, J., and A. Z. Genack, 2011, Nature (London) **471**, 345.
Wang, L. V., and S. Hu, 2012, Science **335**, 1458.
Wang, L. V., and H.-i. Wu, 2012, *Biomedical Optics: Principles and Imaging* (John Wiley & Sons, New York).
Wang, Y. M., B. Judkewitz, C. A. DiMarzio, and C. Yang, 2012, Nat. Commun. **3**, 928.
Washburn, S., C. P. Umbach, R. B. Laibowitz, and R. A. Webb, 1985, Phys. Rev. B **32**, 4789.
Washburn, S., and R. A. Webb, 1986, Adv. Phys. **35**, 375.
Webb, R. A., S. Washburn, C. P. Umbach, and R. B. Laibowitz, 1985, Phys. Rev. Lett. **54**, 2696.
Weidenmüller, H. A., 1990, Physica A (Amsterdam) **167**, 28.
Weidenmüller, H. A., and G. E. Mitchell, 2009, Rev. Mod. Phys. **81**, 539.
Wellens, T., and B. Grémaud, 2008, Phys. Rev. Lett. **100**, 033902.
Weyl, H., 1911, Nachrichten von der Gesellschaft der Wissenschaften zu Göttingen, Mathematisch-Physikalische Klasse 110 [http://www.digizeitschriften.de/dms/resolveppn/?PID=GDZPPN002502526].
Wiersma, D. S., M. P. van Albada, B. A. van Tiggelen, and A. Lagendijk, 1995, Phys. Rev. Lett. **74**, 4193.
Wigner, E. P., 1955a, Ann. Math. Second Series **62**, 548.
Wigner, E. P., 1955b, Phys. Rev. **98**, 145.
Wigner, E. P., 1957, *Proceedings of the Canadian Mathematical Congress* (University of Toronto, Toronto), p. 174.
Wigner, E. P., 1967, SIAM Rev. **9**, 1.
Wijnands, F., J. B. Pendry, F. J. Garcia-Vidal, P. M. Bell, P. J. Roberts, and L. Marti, 1997, Opt. Quantum Electron. **29**, 199.
Willig, K. I., B. Harke, R. Medda, and S. W. Hell, 2007, Nat. Methods **4**, 915.
Winful, H. G., 2003, Phys. Rev. Lett. **91**, 260401.
Wolf, P., G. Maret, E. Akkermans, and R. Maynard, 1988, J. Phys. (Orsay, Fr.) **49**, 63.
Wolf, P.-E., and G. Maret, 1985, Phys. Rev. Lett. **55**, 2696.
Wolterink, T. A. W., R. Uppu, G. Ctistis, W. L. Vos, K.-J. Boller, and P. W. H. Pinkse, 2016, Phys. Rev. A **93**, 053817.
Wong, Z. J., Y-L. Xu, J. Kim, K. O'Brien, Y. Wang, L. Feng, and X. Zhang, 2016, Nat. Photonics **10**, 796.
Xiong, W., P. Ambichl, Y. Bromberg, B. Redding, S. Rotter, and H. Cao, 2016, Phys. Rev. Lett. **117**, 053901.
Xu, X., H. Liu, and L. V. Wang, 2011, Nat. Photonics **5**, 154.
Yamaguchi, I., and T. Zhang, 1997, Opt. Lett. **22**, 1268.
Yamilov, A., and H. Cao, 2003, Phys. Rev. B **68**, 085111.
Yamilov, A., S. Petrenko, R. Sarma, and H. Cao, 2016, Phys. Rev. B **93**, 100201.
Yang, X., C.-L. Hsieh, Y. Pu, and D. Psaltis, 2012, Opt. Express **20**, 2500.
Yang, X., Y. Pu, and D. Psaltis, 2014, Opt. Express **22**, 3405.
Yaqoob, Z., D. Psaltis, M. S. Feld, and C. Yang, 2008, Nat. Photonics **2**, 110.
Yariv, A., 1976, J. Opt. Soc. Am. **66**, 301.
Yariv, A., 1978, Opt. Commun. **25**, 23.
Yariv, A., D. Fekete, and D. M. Pepper, 1979, Opt. Lett. **4**, 52.
Yariv, A., and D. M. Pepper, 1977, Opt. Lett. **1**, 16.
Yilmaz, H., W. L. Vos, and A. P. Mosk, 2013, Biomed. Opt. Express **4**, 1759.
Yu, C., J. Kansky, S. Shaw, D. Murphy, and C. Higgs, 2006, Electron. Lett. **42**, 1024.
Yu, H., T. R. Hillman, W. Choi, J. O. Lee, M. S. Feld, R. R. Dasari, and Y. Park, 2013, Phys. Rev. Lett. **111**, 153902.
Yu, H., J. Park, K. Lee, J. Yoon, K. Kim, S. Lee, and Y. Park, 2015, Curr. Appl. Phys. **15**, 632.
Zaitsev, O., and L. Deych, 2010, J. Opt. **12**, 024001.
Zanotto, S., F. P. Mezzapesa, F. Bianco, G. Biasiol, L. Baldacci, M. S. Vitiello, L. Sorba, R. Colombelli, and A. Tredicucci, 2014, Nat. Phys. **10**, 830.
Zhou, E. H., H. Ruan, C. Yang, and B. Judkewitz, 2014, Optica **1**, 227.